

Improving future gravitational-wave
detectors using nondegenerate
internal squeezing

James W. Gardner

A thesis submitted for partial fulfilment of the degree of
Bachelor of Philosophy (Honours) with Honours in Physics at
The Australian National University

October 2021

Declaration

This thesis is an account of research undertaken between February 2021 and October 2021 at the Centre for Gravitational Astrophysics, Research School of Physics and Research School of Astronomy and Astrophysics, The Australian National University, Canberra, Australia.

Except where acknowledged in the customary manner, the material presented in this thesis is, to the best of my knowledge, original and has not been submitted in whole or part for a degree at any other university.

The research presented in this thesis was completed on the lands of the Ngunnawal and Ngambri people, the traditional owners of the land of The Australian National University's Canberra campus. I acknowledge that this land was stolen and sovereignty was never ceded, and I pay my respects to the elders past, present, and emerging.

James W. Gardner

October 2021

Acknowledgements

I thank my supervisor David McClelland for offering his strategy and wisdom for this project, fostering my general outlook on research, and making me feel welcome. I thank my other supervisors (nominal and honorary) Min Jet Yap, Vaishali Adya, and Sheon Chua for their generous attention, advice, encouragement, knowledge, and humour during the research and editing of this thesis. I thank the CGA squeezer group for our discussions and particularly Dan Gould for his expertise with lasing theory. In summary, to all of the squeezer group, I quote Miranda from Shakespeare's *The Tempest*:

O, wonder!
How many goodly creatures are there here!
How beauteous mankind is! O brave new world
That has such people in't!

I thank Xiang Li for granting the use of the code from Ref. [1] to compare to my results. I thank Carl Bender for the stimulating discussion about PT-symmetry. I thank Henry Gardner and Callum Sambridge for their editorial assistance. The optical configurations in this thesis were illustrated using graphics from Alexander Franzen [2]. Finally, I thank my friends and family for their support.

Abstract

Gravitational waves are “ripples” in spacetime emitted by massive astrophysical events. Over the past decade, interferometric detectors have been used to measure gravitational waves from the binary mergers of black holes and neutron stars to learn more about such systems; these gravitational waves had frequencies around 100 Hz. Other frequencies of gravitational waves are thought to exist and contain valuable information but are yet to be detected. For example, detecting kilohertz (1–4 kHz) gravitational waves from binary neutron-star mergers could be used to further constrain the neutron-star equation-of-state and better understand exotic states of matter. However, to do so, the sensitivity of current detectors will need to be extended from 100 Hz to the kilohertz regime.

The kilohertz sensitivity of current gravitational-wave detectors is limited by quantum noise from the fundamental quantum uncertainties in the state of light inside the detector. This noise can be mitigated by replacing the vacuum fluctuations entering the readout port of the detector with squeezed states. In this thesis, I investigate a new technique to improve kilohertz sensitivity by placing a nondegenerate squeezer inside the detector. This technique, called nondegenerate internal squeezing, improves sensitivity by amplifying the detector’s response to the gravitational-wave signal more than it increases the quantum noise. To assess its feasibility, I derive an analytic Hamiltonian model of nondegenerate internal squeezing and calculate its sensitivity and stability as well as analyse its tolerance to the realistic optical losses expected in a future gravitational-wave detector. My model indicates that nondegenerate internal squeezing is stable, robust to detection loss in the readout, and provides a viable alternative to other proposals to improve kilohertz sensitivity. I demonstrate a technique to determine its squeezing threshold and, therefore, the limits of its operation. I find that nondegenerate internal squeezing could feasibly improve the sensitivity of a future detector to 1–4 kHz gravitational waves. I also explore an alternative readout scheme that is promising for broadband 0.1–4 kHz sensitivity.

Contents

Declaration	i
Acknowledgements	ii
Abstract	iii
1 Introduction	1
1.1 Gravitational waves	1
1.1.1 Kilohertz gravitational-wave astrophysics	2
1.2 Interferometric gravitational-wave detectors	2
1.2.1 Factors limiting kilohertz sensitivity	4
1.2.2 Literature review: how to improve kilohertz sensitivity	5
1.3 Thesis outline	6
1.4 Chapter summary	7
2 Background theory of quantum noise and squeezing in gravitational-wave detectors	8
2.1 Quantum-mechanical nature of light	8
2.1.1 Squeezing	10
2.2 Hamiltonian models of squeezing	12
2.2.1 Degenerate OPO	12
2.2.2 Nondegenerate OPO	17
2.3 Quantum noise in gravitational-wave detectors	21
2.3.1 Squeezing in current gravitational-wave detectors	22
2.4 Chapter summary	23
3 Existing proposals for improving kilohertz sensitivity	24
3.1 Degenerate internal squeezing	24

3.1.1	Understanding the behaviour using a Hamiltonian model	25
3.1.2	Limitation: tolerance to optical loss	28
3.2	Stable optomechanical filtering	30
3.2.1	Limitation: tolerance to mechanical loss	31
3.3	Chapter summary	32
4	Analytic model of nondegenerate internal squeezing	33
4.1	Motivation	33
4.2	Analytic Hamiltonian model	35
4.3	Results	41
4.4	Stability and threshold	45
4.4.1	Stability	45
4.4.2	Singularity threshold	47
4.5	Chapter summary	51
5	Nondegenerate internal squeezing for gravitational-wave detection	52
5.1	Tolerance to optical loss	52
5.1.1	Comparison to degenerate internal squeezing	55
5.1.2	Optimal squeezing	56
5.2	Comparison to stable optomechanical filtering	56
5.3	Feasibility for gravitational-wave detection	59
5.4	Chapter summary	61
6	Alternative readout schemes for nondegenerate internal squeezing	63
6.1	Conceptual understanding and model	63
6.2	Results	65
6.3	Idler readout tolerance to optical loss	67
6.3.1	Variational idler readout and tolerance to pump phase	70
6.4	Idler readout for gravitational-wave detection	72
6.5	Chapter summary	73
7	Conclusions and future work	74
7.1	Future work	75

A Stability of degenerate internal squeezing	78
B Comparison of abstract mode structures	79
C Singularity threshold for degenerate internal squeezing	80
Bibliography	82

Introduction

This chapter outlines the problem that this thesis addresses. In Section 1.1, I explain and motivate the detection of kilohertz gravitational waves. Then, in Section 1.2, I describe how gravitational-wave detectors work, explain what currently prevents them from detecting kilohertz gravitational waves, and review the literature of possible solutions. Finally, in Section 1.3, I outline what this thesis contributes towards detecting kilohertz gravitational waves in the future.

1.1 Gravitational waves

Gravitational waves are propagating perturbations in spacetime described by the Einstein field equations of General Relativity [3, 4]. These waves are predicted to be emitted by the acceleration of massive objects under certain asymmetry conditions. Gravitational-wave signals at around 100 Hz have been detected from the late inspiral of compact binary systems, i.e. the last moments before the merger of, for example, two black holes

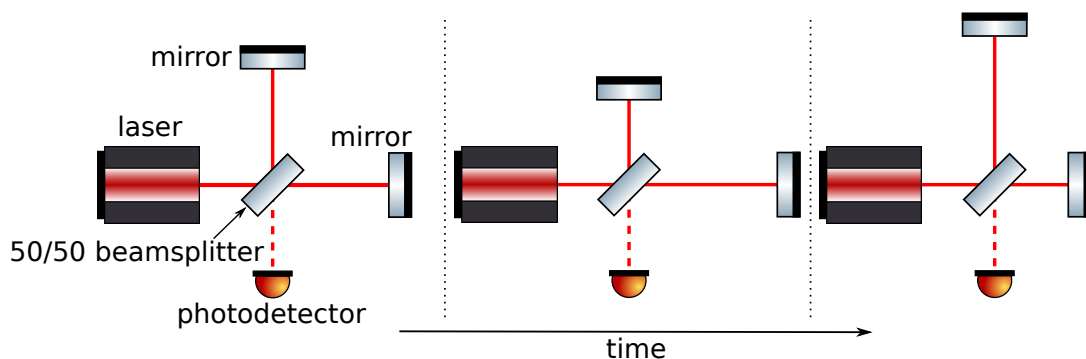


Figure 1.1: The exaggerated effect of a gravitational wave incident into the page upon a Michelson interferometer. Over time, the gravitational wave complementarily stretches and squashes the two perpendicular arms which changes the interference pattern at the photodetector.

or neutron stars [5]. These waves alternately stretch and squash spacetime along the two axes perpendicular to the direction of propagation as shown in Fig. 1.1. The gravitational-wave strain $h(t) = \frac{\Delta L}{L}$ gives the fractional change in length of one of these axis of length L over time t [3]. The goal of gravitational wave detection is to accurately and precisely measure $h(t)$ to extract the encoded astrophysical information about the source of the gravitational wave.

1.1.1 Kilohertz gravitational-wave astrophysics

To date, gravitational waves have only been detected around 100 Hz [5, 6], but there is believed to be varied and interesting astrophysics encoded in kilohertz gravitational waves. For example, gravitational waves from 1–4 kHz are predicted to be emitted during the coalescence and from the remnant of binary neutron-star mergers [7]. These signals are predicted to contain information otherwise unavailable about the exotic states of matter inside neutron stars that could better constrain the neutron-star equation-of-state and improve our understanding of matter under extreme conditions [7, 8]. Other potential astrophysical science using kilohertz gravitational waves includes determining the origin of low-mass black holes by detecting binary black hole–neutron star mergers [9], insights on the post-bounce dynamics of core-collapse supernovae [10], improving measurements of the Hubble constant independently of electromagnetic observations [11], and searching the stochastic gravitational-wave background for primordial sources [8]. This possible wealth of new astrophysics motivates developing the ability to detect kilohertz gravitational waves; I will focus on 1–4 kHz frequencies and the case example of binary neutron-star mergers.

1.2 Interferometric gravitational-wave detectors

Current gravitational-wave detectors are based on the *Michelson interferometer* as shown in Fig. 1.1 where a laser beam is split down two perpendicular arms before returning and interfering at the beamsplitter to produce an interference pattern at the output [12, 13]. An incident gravitational wave changes the path length difference between the kilometre-long arms by less than a thousandth the width of a proton [14] which poses a great

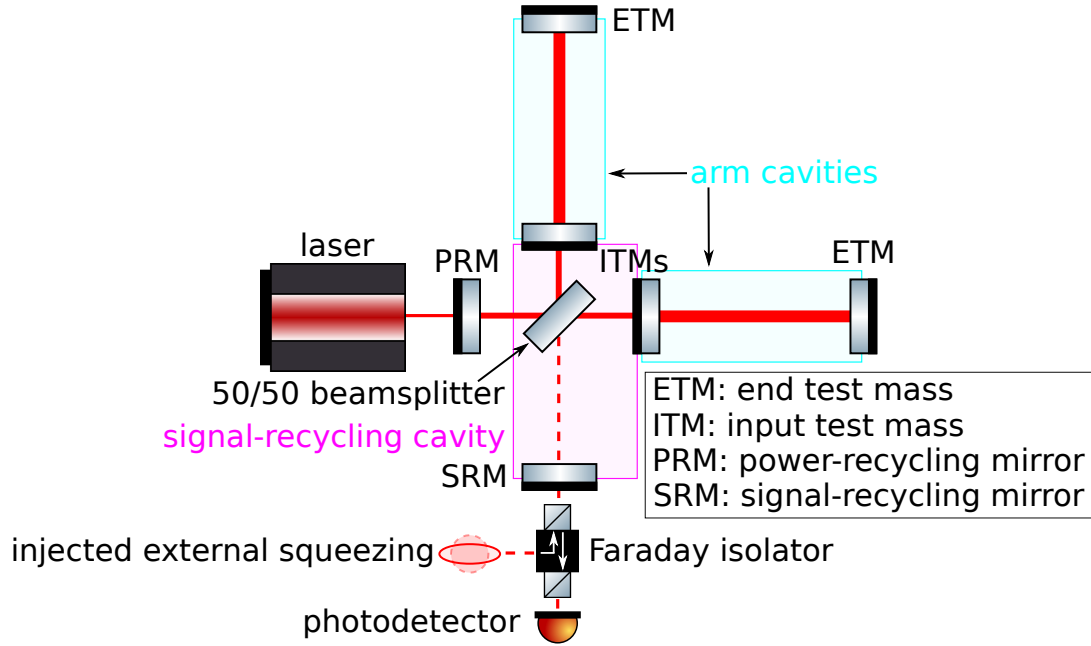


Figure 1.2: Dual-recycled Fabry-Perot Michelson interferometer configuration, where cavities are introduced to enhance the sensitivity of the Michelson interferometer in Fig. 1.1. Technically, the recycling cavities include their respective recycling mirror and the whole Michelson [15, 16], but I highlight only the inner Michelson to reduce clutter. Injected, degenerate external squeezing via a Faraday isolator is shown for later reference, represented by a squeezed noise ellipse.

challenge for detection.

Optical cavities are introduced to improve the sensitivity of the detector ¹ as shown in Fig. 1.2. Firstly, arm cavities are introduced that increase the circulating power in the arms to increase the detector’s response to passing gravitational-wave signals (called the “signal response” of the detector) [13]. Secondly, a power-recycling cavity is introduced between a power-recycling mirror and the Michelson to resonantly increase the power input into the interferometer [15, 13]. Finally, a signal-recycling cavity is introduced via a signal-recycling mirror that changes the overall resonance behaviour of the signal response and can be tuned to achieve broadband or narrow-band enhancement [15, 16]. This enhanced detector is called a dual-recycled Fabry-Perot Michelson interferometer [15, 13] and will be modelled in Chapter 3. Without these cavities, the detection of 100 Hz gravitational waves would not be possible [12].

¹Here and henceforth, I mean the whole gravitational-wave detector, not the photodetector.

1.2.1 Factors limiting kilohertz sensitivity

Gravitational-wave detectors are limited at kilohertz frequencies by several factors that affect their signal response, noise, and sensitivity.

The detector's kilohertz *signal response is limited by the resonance behaviour of the arm cavities*. Optical cavities display resonance behaviour due to the different propagation phases acquired on each round-trip (i.e. circuit) of the cavity by light at different frequencies ² [17]. In the steady-state, the light entering a cavity interferes with the circulating light which amplifies the circulating power if the cavity is resonant. For the detector in Fig. 1.2, the sensitivity below the arm cavity bandwidth is improved by the power amplification from the resonant arm cavities. However, at kilohertz, the arm cavities are off-resonance and the signal response is decreased. Although the other cavities in the interferometer also display resonance behaviour, the kilometre-long arm cavities have the limiting bandwidth, e.g. ~ 100 Hz for 4 km arms [12] ³, and therefore limit the kilohertz signal response.

A detector is subject to noise from many sources. At kilohertz, the *noise response is dominated by quantum shot noise*, with the sum of contributions from all other noise sources contributing less than half the total noise for the Advanced Laser Interferometric Gravitational-Wave Observatory (Advanced LIGO) [12, 18]. Therefore, with my focus on kilohertz frequencies, quantum noise is the primary source of noise that I consider in this thesis.

The *Mizuno limit* states that the circulating power limits an interferometer's integrated quantum noise-limited sensitivity, i.e. the product of its bandwidth and peak sensitivity [19]. This means that, for fixed circulating power, increasing the bandwidth to improve kilohertz sensitivity would sacrifice existing low-frequency (~ 100 Hz) sensitivity. The Mizuno limit could be alleviated if the circulating power could be increased, however, this is technologically challenging and is an ongoing area of research, from mitigating current effects which prevent increasing the power [20, 21] to working towards the power

²I will not consider spatial behaviour (e.g. spatial modes) in this thesis.

³I only consider the first resonance of the arm cavities since the second resonance is above 1–4 kHz. Separately, I also ignore that in a Michelson interferometer the phase accumulated in the arms due to the gravitational wave can cancel between going from and coming back to the beamsplitter since this only affects frequencies above 1–4 kHz (e.g. 37.5 kHz for 4 km arms [12, 13]).

requirements of future detectors [22]. Ultimately, arbitrarily high circulating power is not possible, and, therefore, a different method is required to improve kilohertz sensitivity that can work around the Mizuno limit.

1.2.2 Literature review: how to improve kilohertz sensitivity

Over the past decade, various proposals to improve the kilohertz sensitivity of gravitational-wave detectors have been made, two of which are particularly relevant to this thesis. One is *degenerate internal squeezing* (also known as a degenerate quantum expander) which has been characterised in different operating regimes, e.g. to improve broadband [23] or kilohertz [24] sensitivity. This configuration avoids the Mizuno limit without increasing the circulating power by using a non-classical technique, quantum squeezing [19] that I will detail later. However, degenerate internal squeezing has a low tolerance to optical losses because the squeezing it uses degrades with optical loss [23]. Although research continues today into optimising degenerate internal squeezing in the high loss regime [25], its low tolerance to loss motivates investigating configurations that are more tolerant to the realistic losses expected in a future detector.

Another existing proposal is *optomechanical filtering* which improves sensitivity without increasing the circulating power by broadening the arm cavity resonance that limits the kilohertz signal response, called the “white-light cavity” idea [26]⁴. Optomechanical filtering in this context was first proposed in an unstable configuration which required a stabilising feedback control system [26]. Then, the system was made stable without a control system by changing the readout (measurement) scheme [1]. This stable configuration was recently further investigated and showed promising sensitivity improvement with a more realistic model that included higher-order modes [29]. However, to improve sensitivity, stable optomechanical filtering has a stringent requirement of low mechanical loss [26, 1]. Research is ongoing into how to achieve the demands of this configuration [30, 31] but the demands, like those of degenerate internal squeezing, motivate investigating more loss-tolerant configurations.

Although there are other existing proposals for kilohertz improvement (such as Refs. [32,

⁴The white-light cavity idea was initially proposed using atomic media [27] and, subsequently, optomechanics [28].

33]), degenerate internal squeezing and stable optomechanical filtering are currently the most developed proposals. These two proposals are also the most related configurations to my work in this thesis that examines *nondegenerate internal squeezing*, an alternative gravitational-wave detector configuration that combines stable optomechanical filtering with the all-optical approach of degenerate internal squeezing. Although nondegenerate squeezing has long been studied both outside [34] and within (e.g. Ref. [35]) gravitational-wave research, this particular configuration has only been mentioned once in the literature as its Hamiltonian is equivalent to stable optomechanical filtering under a certain mapping of optical to mechanical modes [1]. However, in the work studying stable optomechanical filtering [1, 29], only the dominant loss term is included in the model and the perturbations due to other realistic losses are ignored, that is, it is not known how low these other losses need to be. Moreover, the realistic optical and mechanical losses expected in a future detector are different, which could mean that nondegenerate internal squeezing might have less-stringent loss constraints than stable optomechanical filtering. Finally, other aspects of nondegenerate internal squeezing are not known, such as its squeezing threshold, its behaviour in low and high loss limits, and its possible readout schemes.

1.3 Thesis outline

In this thesis, I investigate the unexplored aspects of nondegenerate internal squeezing discussed above and present the first results on them. In particular, I characterise nondegenerate internal squeezing with realistic optical loss in every optical mode for different readout schemes and assess its feasibility for kilohertz gravitational-wave detection.

- In Chapter 2, I will review the background physics of squeezing and the quantum noise response of a detector. I will demonstrate the analytic Hamiltonian modelling that I use throughout this thesis and will discuss how squeezing is currently used to improve the sensitivity of gravitational-wave detectors.
- In Chapter 3, I will discuss the benefits and limitations of degenerate internal squeezing and stable optomechanical filtering which motivate combining them into nondegenerate internal squeezing.

- Then, in Chapter 4, I will derive an analytic Hamiltonian model of nondegenerate internal squeezing. I will characterise the sensitivity and stability of the configuration, study its high and low loss limits, and derive its squeezing threshold.
- Next, in Chapter 5, I will compare nondegenerate internal squeezing’s tolerance to realistic optical loss to the two existing proposals discussed above and consider its application to kilohertz (1–4 kHz) and broadband (0.1–4 kHz) gravitational-wave detection.
- In Chapter 6, I will discuss the differences between the possible readout schemes of nondegenerate internal squeezing and consider whether the broadband sensitivity can be further improved with a different readout scheme.
- Finally, in Chapter 7, I will consider the conclusions and limitations of my work and what avenues of future work it suggests.

The abbreviations used throughout this thesis are shown in Table 1.1.

ITM	input test mass	DC	direct current
ETM	end test mass	SRC	signal-recycling cavity
SRM	signal-recycling mirror	PT	parity-time
OPO	optical parametric oscillator	GW	gravitational wave
PD	photodetector	RP	radiation pressure

Table 1.1: The abbreviations used throughout this thesis in order of appearance.

1.4 Chapter summary

In this chapter, I have motivated the detection of kilohertz gravitational waves for advancing our understanding of astrophysical phenomena. I have explained how detectors based on the Michelson interferometer can detect gravitational waves at around 100 Hz but that their sensitivity cannot be simply broadened to also detect kilohertz gravitational waves. Finally, I have mentioned the two proposed configurations (degenerate internal squeezing and stable optomechanical filtering) that motivate my work, the limitations of these two configurations, and that this thesis will examine nondegenerate internal squeezing as an alternative configuration for gravitational-wave detection.

Background theory of quantum noise and squeezing in gravitational-wave detectors

In this chapter, I review the necessary physics to describe quantum noise and squeezing. Firstly, in Section 2.1, I review the quantum-mechanical nature of light and introduce squeezing using the conventional mathematical formalism that starts from the Heisenberg Uncertainty Principle. In Section 2.2, I then show how squeezing can be understood using Hamiltonian models of the degenerate and nondegenerate optical parametric oscillator (OPO) as I use similar Hamiltonian modelling later in my work. Finally, in Section 2.3, I explain how squeezing improves the quantum noise-limited sensitivity of current gravitational-wave detectors.

2.1 Quantum-mechanical nature of light

The quantum noise in a detector is caused by the quantum-mechanical, fundamental uncertainties in the state of the light in the detector [36, 37]. To express this, I quantise the electromagnetic field following the conventional formalism (e.g. see Refs. [38, 39] throughout this chapter). Let the creation and annihilation operators of a resonant mode of an optical cavity be \hat{a}^\dagger and \hat{a} , respectively, that act on the Hilbert space of states of the light inside the cavity such that $\hat{a}|\emptyset\rangle = 0$ where $|\emptyset\rangle$ is the vacuum state. These bosonic operators obey the commutation relation $[\hat{a}, \hat{a}^\dagger] = 1$. In the Heisenberg Picture with their time-dependence implicit, these operators evolve according to the Heisenberg equation-of-motion $\dot{\hat{a}} = -\frac{i}{\hbar}[\hat{a}, \hat{H}]$, and its conjugate equation, given a quantised, time-independent

Hamiltonian \hat{H} and the reduced Plank constant \hbar . In the absence of any interaction, the mode created by \hat{a}^\dagger evolves according to the harmonic oscillator Hamiltonian $\hat{H}_0 = \hbar\omega(\hat{a}^\dagger\hat{a} + \frac{1}{2})$ where ω is the angular frequency of the mode corresponding to the energy $\hbar\omega$ per each occupation of the mode.

Consider the linear combination $\hat{X}_\theta = \frac{1}{\sqrt{2}}(e^{-i\theta}\hat{a} + e^{i\theta}\hat{a}^\dagger)$ for $\theta \in [0, 2\pi)$ and let the ‘‘amplitude’’ $\hat{X}_1 = \hat{X}_{\theta=0}$ and ‘‘phase’’ $\hat{X}_2 = \hat{X}_{\theta=\frac{\pi}{2}}$ quadratures¹ be defined such that they span these combinations and obey $[\hat{X}_1, \hat{X}_2] = i$. The annihilation/creation operators can be converted to the quadrature picture by the matrix $\Gamma = \frac{1}{\sqrt{2}}\begin{bmatrix} 1 & 1 \\ -i & i \end{bmatrix}$ such that $(\hat{X}_1, \hat{X}_2)^T = \Gamma(\hat{a}, \hat{a}^\dagger)^T$. Unlike \hat{a} and \hat{a}^\dagger , these quadrature operators are observable because they are Hermitian and therefore they can be used to measure the state of a detector (and, ultimately, a gravitational wave) which is why I am interested in them². The uncertainty in a measurement of \hat{X}_1 is given by $\sigma_{X_1} = \sqrt{\langle \hat{X}_1^2 \rangle - \langle \hat{X}_1 \rangle^2}$ where $\langle \hat{X}_1 \rangle = \langle \emptyset | \hat{X}_1 | \emptyset \rangle$. However, the Heisenberg Uncertainty Principle states that

$$\sigma_{X_1}\sigma_{X_2} \geq \frac{1}{2}|\langle [\hat{X}_1, \hat{X}_2] \rangle| = \frac{1}{2}. \quad (2.1)$$

Therefore, the quadratures can never be simultaneously exactly known and there is always uncertainty in at least one of them.

The *Fourier-domain* counterparts to the above time-domain quadratures contain spectral information about a gravitational-wave signal³. Let $\hat{O}(\Omega) = \int_{-\infty}^{\infty} \frac{1}{\sqrt{2}}\hat{O}e^{-i\Omega t}dt$ be the Fourier transform of \hat{O} with the Fourier angular frequency Ω . Then, the Fourier-domain quadratures are $\hat{X}_\theta(\Omega) = \frac{1}{\sqrt{2}}(e^{-i\theta}\hat{a}(\Omega) + e^{i\theta}\hat{a}^\dagger(-\Omega))$ where the sign of the last argument was flipped to account for the $e^{-i\Omega t}$ in the Fourier transform⁴. In the Fourier domain, the time-domain variance σ_O^2 becomes a (single-sided) spectral density $S_O(\Omega)\delta(\Omega - \Omega') = \langle \hat{O}(\Omega) \circ \hat{O}^\dagger(\Omega') \rangle$ ⁵. The spectral densities of the quadratures obey

¹Although they are only associated to the amplitude and the phase of the electric field, respectively, by convention [38].

²The exact method of measuring the quadratures at the photodetector is not of concern, but a balanced homodyne readout scheme will suffice throughout this thesis [38].

³Transient gravitational-wave signals have durations on the order of seconds, but the response of an interferometer is on the time-scale of the round-trip time of the arms (e.g. $\sim 10 \mu s$) [13]. Therefore, the steady-state approximation required for the Fourier transform is valid for the interferometer.

⁴Although the Fourier-domain quadratures are not Hermitian, they are indirectly observable, either through their time-domain counterparts or through measurements that can derive their real and imaginary parts separately which is possible due to the condition $\hat{X}^\dagger(\Omega) = \hat{X}(-\Omega)$ [40].

⁵Here, $A \circ B = \frac{1}{2}(A \cdot B + B \cdot A)$.

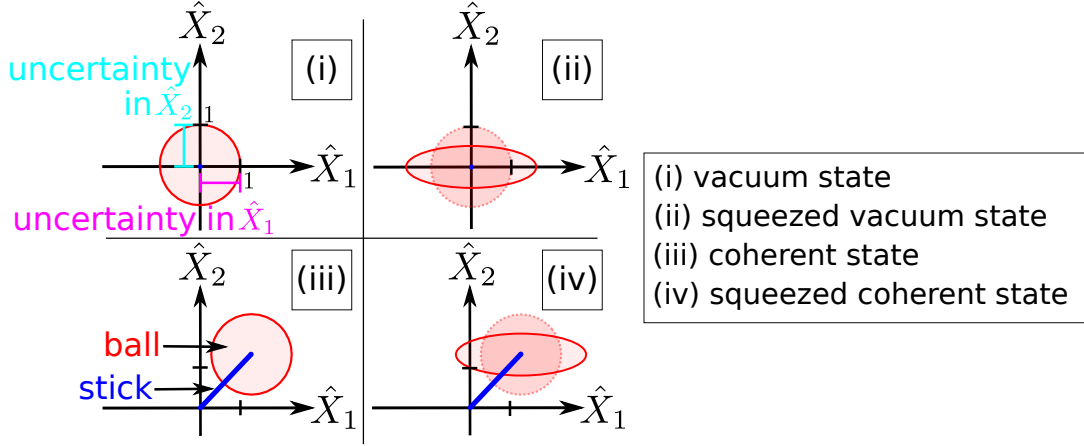


Figure 2.1: “Ball-and-stick” representation of squeezing. The red ellipse represents the uncertainty around the coherent amplitude represented by the blue stick; the coherent amplitude is zero for the vacuum state. The lengths of the ellipse’s semi-axes represent the uncertainty $\sqrt{S_{X_i}}$ in each quadrature $\hat{X}_i(\Omega)$ for $i = 1, 2$. Squeezing the noise changes these lengths such that their product is preserved, or increased if optical losses are present, to obey the Heisenberg Uncertainty Principle.

a similar Heisenberg Uncertainty Principle as Eq. 2.1, $\sqrt{S_{X_1} S_{X_2}} \geq 1$. This inequality is achieved as an equality by the uncorrelated vacuum state $|\emptyset\rangle$ since for the associated quadratures $\langle \hat{X}_i(\Omega) \circ \hat{X}_j^\dagger(\Omega') \rangle = \delta_{i,j} \delta(\Omega - \Omega')$ where $\delta_{i,j}$ is the Kronecker delta and therefore $\sqrt{S_{X_i}^{\text{vac}}} = 1$ for $i = 1, 2$ [38]. This means that there is equal uncertainty in each of the quadratures $\hat{X}_\theta(\Omega)$ which can be visualised as the vacuum state having a “noise ellipse” with equal semi-axes lengths of one in the $(\hat{X}_1(\Omega), \hat{X}_2(\Omega))$ plane as shown in Fig. 2.1, where the radius of the noise ellipse in a direction θ represents the uncertainty in $\hat{X}_\theta(\Omega)$.

2.1.1 Squeezing

Squeezing refers to a broad range of technologies that decrease uncertainty in a desired quantity by increasing uncertainty in its conjugate, less desired quantity while still obeying the Heisenberg Uncertainty Principle [34]. For example, decreasing (“squeezing”) uncertainty in the amplitude quadrature by some factor $e^{-r} < 1$ by increasing (“anti-squeezing”) uncertainty in the phase quadrature by $e^r > 1$ still satisfies the Heisenberg Uncertainty Principle $(\frac{S_{X_1}}{e^r})(e^r S_{X_2}) \geq 1$. This can be expressed as a squeezing operator trading the uncertainties of a vacuum or coherent state ⁶ and squeezing their noise ellipses

⁶I will only consider squeezed vacuum states in this thesis.

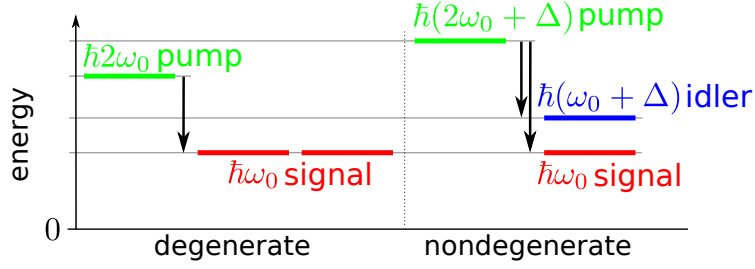


Figure 2.2: Parametric down-conversion, showing the energy levels of the degenerate (left panel) and nondegenerate (right panel) processes. In either case, the process conserves energy, i.e. $\hbar\omega$ for angular frequency ω , and the created photons are squeezed and entangled.

in Fig. 2.1 [38]⁷. Squeezing can also be explained using sideband theory [38] which I do not discuss. When a squeezed state encounters optical loss, the squeezing is reduced as the decoherence of the state reduces correlations and pulls the uncertainties back towards their vacuum values of one, however, the anti-squeezed and squeezed uncertainties are affected differently which increases their product in the Heisenberg Uncertainty Principle⁸.

Optical squeezing can be achieved via a variety of technologies, but I will focus on the production of squeezed states using *nonlinear crystals* [34]. In a crystal with a quadratic polarisability $\chi^{(2)}$ ⁹, the process of parametric down-conversion can occur, where a photon at a pump (angular) frequency ω_p is annihilated to create two entangled, squeezed photons at the “signal”¹⁰ ω_0 and “idler” $\omega_0 + \Delta$ frequencies such that $\omega_p = 2\omega_0 + \Delta$ to conserve energy [41]. The frequency difference Δ , chosen by how the crystal is pumped, is small in comparison to the other frequencies in the system, and when $\Delta = 0$ the produced photons are energetically degenerate which changes the mode structure of the system; the energy level structure of this process is shown in Fig. 2.2. These degenerate and nondegenerate processes can be used to manipulate the quantum noise differently.

⁷This correlates the quadratures that lie off the semi-axes of the noise ellipse, e.g. \hat{X}_θ and $\hat{X}_{\theta'}$ for $\theta \neq 0, \pi/2$ for $0 < \theta < \pi$ and similarly for θ' .

⁸This will be explained later as optical loss mixing the light with the vacuum as shown in Fig. 2.4.

⁹When classically exposed to an electric field \vec{E} it produces an electric field with i th component $\epsilon_0(\sum_j \chi_{ij}^{(1)} E_j + \sum_{j,k} \chi_{ijk}^{(2)} E_j E_k)$ where $\chi^{(1)}$ is the linear polarisability.

¹⁰There is potential confusion later between the signal mode of light created by the squeezer and the light in the detector that contains the gravitational-wave signal. I will clarify wherever necessary.

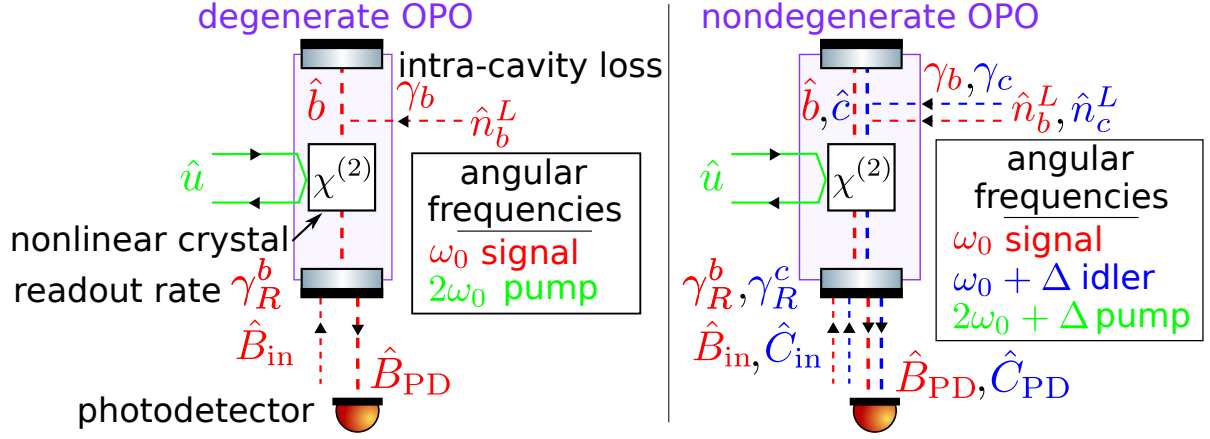


Figure 2.3: Degenerate (left panel) and nondegenerate (right panel) optical parametric oscillator (OPO) configurations with all modes labelled. Intra-cavity loss (e.g. γ_b) occurs via the mechanism in Fig. 2.4 henceforth. The nonlinear crystal is labelled with $\chi^{(2)}$ to represent its quadratic polarisability. In practice, the pump mode also circulates inside the cavity but I represent it as shown to reduce clutter.

2.2 Hamiltonian models of squeezing

Cavity-based squeezing is currently used to generate squeezed states for gravitational-wave detectors [42]. Here, I introduce the Hamiltonian modelling of cavity-based squeezing that I will use later in my work.

2.2.1 Degenerate OPO

A degenerate optical parametric oscillator (OPO) consists of a nonlinear crystal operating the degenerate down-conversion process inside of an optical cavity as shown in Fig. 2.3 [43]. The cavity increases the number of passes of the squeezer that the light makes and therefore increases the squeezing. The vacuum state entering the cavity through the readout port exits squeezed by the crystal and its quadratures are measured at a photodetector.

Analytic model

The *Hamiltonian* of this system is given by $\hat{H} = \hat{H}_0 + \hat{H}_I + \hat{H}_\gamma$, where \hat{H}_0 gives the decoupled dynamics of the pump mode with annihilation operator \hat{u} at $2\omega_0$ and the cavity

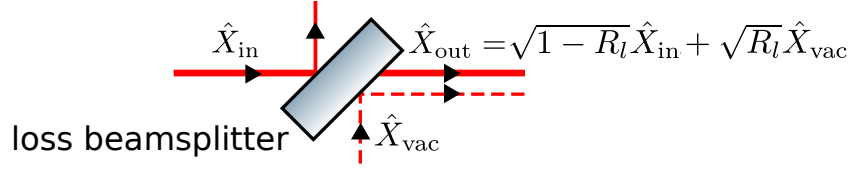


Figure 2.4: Beamsplitter model of optical loss. The light \hat{X}_{in} loses energy into the environment at some rate and uncorrelated vacuum \hat{X}_{vac} is introduced at some rate; the Fluctuation-Dissipation Theorem states that these two rates are equal – let them be R_l . The beamsplitter reflection R_l and transmission T_l coefficients obey $T_l + R_l = 1$ to conserve energy which is proportional to the quadrature squared. I use the equivalent “loss port” convention $R_l \leftrightarrow T_l$ for the intra-cavity losses in Fig. 2.3.

mode \hat{b} at frequency ω_0 ¹¹, \hat{H}_I gives the parametric down-conversion in the crystal¹², and \hat{H}_γ gives the coupling to the vacuum entering the readout port (\hat{B}_{in}) and describes the intra-cavity loss [23],

$$\hat{H}_0 = \hbar\omega_0\hat{b}^\dagger\hat{b} + \hbar 2\omega_0\hat{u}^\dagger\hat{u}, \quad \hat{H}_I = i\hbar\frac{g}{2}(\hat{u}(\hat{b}^\dagger)^2 - \hat{u}^\dagger\hat{b}^2)$$

$$\hat{H}_\gamma = i\hbar\sqrt{2} \int \left(\sqrt{\gamma_R^b} (\hat{b}^\dagger(\Omega)\hat{B}_{\text{in}}(\Omega) - \hat{b}(\Omega)\hat{B}_{\text{in}}^\dagger(\Omega)) + \sqrt{\gamma_b} (\hat{b}^\dagger(\Omega)\hat{n}_b^L(\Omega) - \hat{b}(\Omega)\hat{n}_b^{L\dagger}(\Omega)) \right) d\Omega.$$

Here, g is the real coupling constant of the down-conversion and γ_R^b, γ_b are the readout and intra-cavity loss rates, respectively¹³. The Fluctuation-Dissipation Theorem states that the intra-cavity loss of energy to the thermal bath of the propagation medium and the optics is accompanied by the introduction of uncorrelated noise [44]. Therefore, I model the optical loss with a beamsplitter that releases energy into the environment and creates another open port for vacuum¹⁴ to enter through as shown in Fig. 2.4. It suffices to have a single loss mechanism inside the cavity coupled to vacuum \hat{n}_b^L [38]. “Detection” loss can also occur at the photodetector and in the output chain of optics but I omit it from this model.

¹¹I make a single-mode approximation to the light in the cavity and assume that it is only in mode \hat{b} and interacts with the resonating pump mode. This approximation is valid when considering frequencies within the cavity’s bandwidth [39].

¹²As well as the reverse process of “second-harmonic generation” where two ω_0 photons combine to create a $2\omega_0$ photon.

¹³These coupling rates are given by $\gamma = -\frac{1}{2\tau} \log(1 - T)$ where $\tau = \frac{2L}{c}$ is the round-trip time of the length L cavity and T is the transmission through the readout port ($T_{R,b}$) or the intra-cavity loss port ($T_{l,b}$).

¹⁴By which I mean vacuum fluctuations, i.e. the sea of virtual photons, henceforth.

The *Heisenberg-Langevin equation-of-motion*¹⁵ [45, 43] for \hat{b} given the bosonic commutation relations¹⁶, is

$$\dot{\hat{b}} = -i\omega_0\hat{b} + g\hat{u}\hat{b}^\dagger - \gamma_{\text{tot}}^b\hat{b} + \sqrt{2\gamma_R^b}\hat{B}_{\text{in}} + \sqrt{2\gamma_b}\hat{n}_b^L. \quad (2.2)$$

Here, $\gamma_{\text{tot}}^b = \gamma_R^b + \gamma_b$ is the total loss rate from the cavity. I ignore the dynamics of the pump mode \hat{u} by making a semi-classical approximation with coherent amplitude $ue^{i\phi}$ where ϕ is the pump phase and u is determined by the classical pump power that I assume to be constant. This “no pump depletion” assumption is widely used in the literature and I will later justify what parameter range it is valid in [39]. In the Interaction Picture, i.e. separating the simple dynamics of \hat{H}_0 onto the states, and $\hat{H}_I + \hat{H}_\gamma$ onto the operators, I can ignore the $-i\omega_0\hat{b}$ term from Eq. 2.2 which leaves

$$\dot{\hat{b}} = \chi e^{i\phi}\hat{b}^\dagger - \gamma_{\text{tot}}^b\hat{b} + \sqrt{2\gamma_R^b}\hat{B}_{\text{in}} + \sqrt{2\gamma_b}\hat{n}_b^L. \quad (2.3)$$

Here, $\chi = gu$, the “squeezer parameter”¹⁷, is the gain rate of photons in the cavity mode. To find the quantum noise, I take the fluctuating components of each of these operators, i.e. $\delta\hat{b}(t) = \hat{b}(t) - \langle\hat{b}\rangle_t$, thereby ignoring the classical dynamics described by the time-average $\langle\hat{b}\rangle_t$. Since each of the input modes $\hat{B}_{\text{in}}, \hat{n}_b^L$ are vacuum, with a time-average of zero, the equation is the same for the fluctuating components¹⁸. Therefore, I leave δ implicit in the notation, i.e. $\delta\hat{b} \mapsto \hat{b}$, to reduce clutter.

In the *Fourier domain*, Eq. 2.3 can be solved algebraically [43]

$$\vec{\hat{b}}(\Omega) = M_b^{-1} \left(\sqrt{2\gamma_R^b}\vec{\hat{B}}_{\text{in}}(\Omega) + \sqrt{2\gamma_b}\vec{\hat{n}}_b^L(\Omega) \right), \quad M_b = (\gamma_{\text{tot}}^b - i\Omega)\mathbf{I} - \chi \begin{bmatrix} 0 & e^{i\phi} \\ e^{-i\phi} & 0 \end{bmatrix}. \quad (2.4)$$

Here, $\vec{\hat{Q}}(\Omega) = (\hat{Q}(\Omega), \hat{Q}^\dagger(-\Omega))^T$ for each pair of annihilation/creation operators $(\hat{Q}, \hat{Q}^\dagger)$, and \mathbf{I} is the 2-by-2 identity matrix. Using the input/output relation at the readout

¹⁵The Langevin input/output terms come from H_γ and describe the Heisenberg equation-of-motion for an open system.

¹⁶ $[\hat{Q}_i, \hat{Q}_j^\dagger] = \delta_{i,j}$ where the annihilation operator of the i th bosonic mode is \hat{Q}_i .

¹⁷Not to be confused with the polarisability (e.g. $\chi^{(2)}$).

¹⁸Assuming that the squeezer remains below “threshold” which I explain shortly.

port [45], the light incident on the photodetector (\hat{B}_{PD}) is ¹⁹

$$\vec{B}_{\text{PD}}(\Omega) = \vec{B}_{\text{in}}(\Omega) - \sqrt{2\gamma_R^b} \vec{b}(\Omega). \quad (2.5)$$

Using Γ to convert to quadratures $\vec{X}_Q(\Omega) = (\hat{X}_{Q,1}(\Omega), \hat{X}_{Q,2}(\Omega))^T = \Gamma \vec{Q}(\Omega)$ ²⁰ and putting Eqs. 2.4 and 2.5 together, the output quadratures in terms of the input vacuum quadratures are

$$\vec{X}_{\text{PD}}(\Omega) = \mathbf{R}_{\text{in}} \vec{X}_{\text{in}}(\Omega) + \mathbf{R}_b^L \vec{X}_b^L(\Omega), \quad (2.6)$$

$$\mathbf{R}_{\text{in}} = \Gamma \left(\mathbf{I} - 2\gamma_R^b \mathbf{M}_b^{-1} \right) \Gamma^{-1}, \quad \mathbf{R}_b^L = -2\sqrt{\gamma_R^b \gamma_b} \Gamma \mathbf{M}_b^{-1} \Gamma^{-1}. \quad (2.7)$$

This defines the quantum noise response of the degenerate OPO, where the *total quantum noise* ²¹ measured at the photodetector is described by the matrix \mathbf{S}_X of spectral densities

$$(\mathbf{S}_X)_{i,j}(\Omega) \delta(\Omega - \Omega') = \left\langle (\vec{X}_{\text{PD}})_i(\Omega) \circ (\vec{X}_{\text{PD}})_j^\dagger(\Omega') \right\rangle. \quad (2.8)$$

Here, $\langle \dots \rangle$ is the vacuum expectation value. This can be found by assuming uncorrelated vacuum inputs [38] to be

$$\mathbf{S}_X(\Omega) = \mathbf{R}_{\text{in}} \mathbf{R}_{\text{in}}^\dagger + \mathbf{R}_b^L \mathbf{R}_b^{L\dagger}. \quad (2.9)$$

The diagonal elements of \mathbf{S}_X are the Fourier-domain variances S_{X_i} of the light at the photodetector and the off-diagonal elements give the covariances, i.e. correlations, between the two quadratures ²².

Demonstrating squeezing

I now demonstrate that parametric down-conversion squeezes the variances of the measured quadratures. Computing Eq. 2.9 using matrix algebra ²³ shows that, for $\phi = 0$ ²⁴,

¹⁹I ignore the spatial propagation of these external modes because it does not affect the noise.

²⁰This is different to the vectorisation $\vec{Q}(\Omega)$; $\vec{X}_Q(\Omega)$ is a vector of quadratures each of which obeys $\hat{X}^\dagger(-\Omega) = \hat{X}(\Omega)$.

²¹Which I also call the noise response henceforth.

²²Which obey the Hermiticity of \mathbf{S}_X from Eq. 2.8. Like the Fourier-domain quadratures themselves, these covariances are not real but are indirectly observable [46].

²³Which I perform using Wolfram Mathematica [47] throughout this thesis.

²⁴The pump phase ϕ breaks the symmetry between the quadratures by selecting which quadrature is squeezed; $\phi = 0$ corresponds to the angle of the noise ellipse shown in Fig. 2.1.

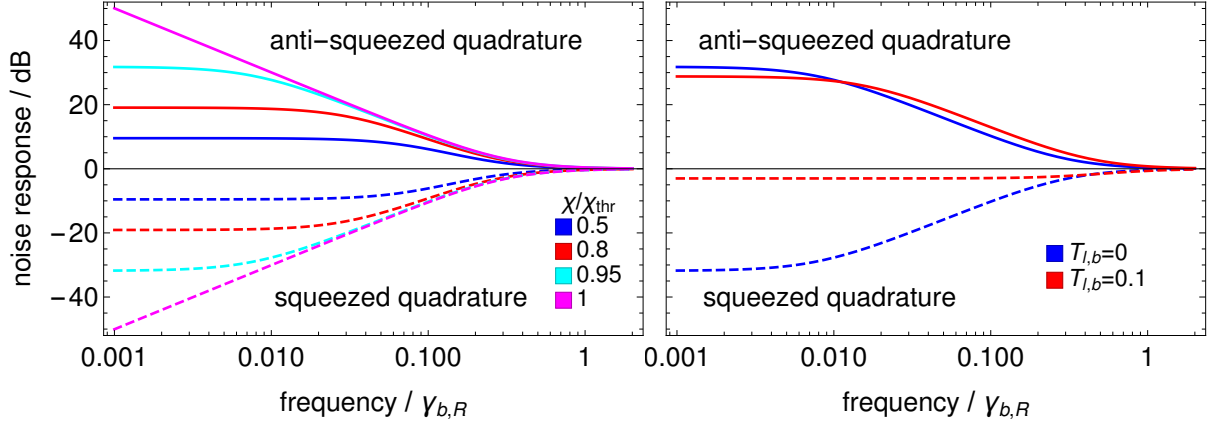


Figure 2.5: Degenerate OPO noise response, i.e. $\sqrt{S_{X_i}}$ versus frequency, showing anti-squeezing ($i = 1$) and squeezing ($i = 2$) for $\phi = 0$. Left panel: different squeezer parameters (χ) up to threshold (χ_{thr}) with no loss. On threshold and at DC ($\Omega = 0$), the anti-squeezed quadrature is singular and the squeezed quadrature is zero. Right panel: different intra-cavity loss ($T_{l,b}$) for a fixed ratio of 95% threshold calculated for each loss. For both quadratures, intra-cavity loss pulls the peak variance towards the vacuum value of one (0 dB) but also broadens the cavity resonance – although here the loss is unrealistically high. The anti-squeezed quadrature is more resistant to loss. I use a 1 m cavity with readout transmission $T_{R,b} = 0.1$.

the covariances vanish and the variances simplify to

$$S_X(\Omega) = \begin{bmatrix} 1 + \frac{4\gamma_R^b \chi}{(\gamma_{\text{tot}}^b - \chi)^2 + \Omega^2} & 0 \\ 0 & 1 - \frac{4\gamma_R^b \chi}{(\gamma_{\text{tot}}^b + \chi)^2 + \Omega^2} \end{bmatrix}. \quad (2.10)$$

Therefore, by turning the squeezer on, $\chi > 0$, one quadrature (\hat{X}_1) has increased uncertainty while the other quadrature (\hat{X}_2) has uncertainty below the vacuum value of 1; these are the anti-squeezed and squeezed quadratures, respectively, as shown in Fig. 2.5. The squeezing/anti-squeezing curves eventually converge to the vacuum value in frequency (around the cavity bandwidth γ_R^b) as the cavity goes off-resonance.

Fig. 2.5 also shows that increasing χ from zero increases the difference from the vacuum value for both quadratures²⁵. The $\Omega = 0$ (DC²⁶) value of the anti-squeezed quadrature from Eq. 2.10 is singular at $\chi_{\text{thr}} = \gamma_{\text{tot}}^b$ and the squeezed quadrature is zero in the lossless case, as shown in Fig. 2.5. This value χ_{thr} , the “*threshold*” of the degenerate OPO, can be understood as the balance of gains and losses inside the cavity: the squeezer creates

²⁵If the vacuum variance $S_X = 1$ is squeezed by a factor e^r , then I quantify the squeezing in amplitude-decibels (dB) as $20 \log_{10}(\sqrt{S_X} e^{-r})$ compared to the vacuum at 0 dB.

²⁶DC (direct current), referring to frequency zero behaviour, comes from electrical engineering.

photons in the cavity mode at a rate χ which are lost at a rate γ_{tot}^b , and when $\chi = \chi_{\text{thr}}$ the gain and loss balance and, like a phase transition, beyond χ_{thr} the OPO starts lasing with a non-zero coherent amplitude at the output [39]. The no-pump-depletion assumption breaks at threshold as it implies that there is no limit to the amount of energy transferred from the pump which makes the system unstable ²⁷. While it is experimentally possible to operate above threshold (e.g. in Ref. [48]), it is not necessary for generating squeezed vacuum states for gravitational-wave detection [42], and, therefore, I will not consider the behaviour above threshold; this makes the no-pump-depletion assumption valid in this thesis ²⁸.

Optical loss decoheres the state of light because it mixes it with the vacuum state as shown in Fig. 2.4. By Eq. 2.10, in the lossless case, the Heisenberg Uncertainty Principle is satisfied as an equality $\sqrt{(S_X)_{1,1}(S_X)_{2,2}} = 1$, and in the lossy case, as an inequality (i.e. > 1) because optical losses decohere the system and the squeezed uncertainty is increased more than the anti-squeezed uncertainty is decreased ²⁹. Introducing intra-cavity loss γ_b acts like damping an oscillator, i.e. the peaks in Fig. 2.5 move towards vacuum but broaden, their quality factor decreasing ³⁰. The intra-cavity loss also increases threshold $\chi_{\text{thr}} = \gamma_{\text{tot}}^b$ which decreases the performance for a fixed pump power. Since this effect can be mitigated experimentally by increasing the pump power, henceforth, I will compare different losses with the same ratio to threshold χ/χ_{thr} , i.e. I will normalise to the different threshold in each case. The effect of losses on the covariances between the other quadratures is similar, i.e. intra-cavity loss reduces the peak and broadens the response.

2.2.2 Nondegenerate OPO

A nondegenerate optical parametric oscillator (OPO) is the same configuration as a degenerate OPO except that the crystal performs nondegenerate parametric down-conversion

²⁷Below threshold, no energy is lost from the pump mode since the squeezed output remains at vacuum.

²⁸Moreover, in the application to gravitational-wave detection, some margin below threshold, e.g. 5%, is maintained so that the system does not stray above threshold.

²⁹For example, the loss does not affect the singularity of the on-threshold anti-squeezed quadrature but does affect the zero of the squeezed quadrature, therefore increasing the product of the uncertainties.

³⁰This means that there are frequencies for which the squeezing is improved by loss because the cavity resonance broadens.

as shown in Fig. 2.3: splitting the pump at frequency $2\omega_0 + \Delta$ down into two ($\Delta \neq 0$) squeezed, entangled modes at ω_0 (the signal) and $\omega_0 + \Delta$ (the idler).

Analytic model

The Hamiltonian of this system is $\hat{H} = \hat{H}_0 + \hat{H}_I + \hat{H}_\gamma$ with [49, 46]

$$\begin{aligned} \hat{H}_0 &= \hbar\omega_0\hat{b}^\dagger\hat{b} + \hbar(\omega_0 + \Delta)\hat{c}^\dagger\hat{c} + \hbar(2\omega_0 + \Delta)\hat{u}^\dagger\hat{u}, & \hat{H}_I &= \hbar\frac{g}{2}(\hat{u}\hat{b}^\dagger\hat{c}^\dagger + \hat{u}^\dagger\hat{b}\hat{c}) \\ \hat{H}_\gamma &= i\hbar\sqrt{2}\int\left(\sqrt{\gamma_R^b}(\hat{b}^\dagger(\Omega)\hat{B}_{\text{in}}(\Omega) - \hat{b}(\Omega)\hat{B}_{\text{in}}^\dagger(\Omega)) + \sqrt{\gamma_b}(\hat{b}^\dagger(\Omega)\hat{n}_b^L(\Omega) - \hat{b}(\Omega)\hat{n}_b^{L\dagger}(\Omega))\right. \\ &\quad \left. + \sqrt{\gamma_R^c}(\hat{c}^\dagger(\Omega)\hat{C}_{\text{in}}(\Omega) - \hat{c}(\Omega)\hat{C}_{\text{in}}^\dagger(\Omega)) + \sqrt{\gamma_c}(\hat{c}^\dagger(\Omega)\hat{n}_c^L(\Omega) - \hat{c}(\Omega)\hat{n}_c^{L\dagger}(\Omega))\right)d\Omega. \end{aligned} \quad (2.11)$$

Here, the pump mode \hat{u} is now at $2\omega_0 + \Delta$, \hat{c} is the idler cavity mode at $\omega_0 + \Delta$ ³¹ with analogous input/output fields to the signal mode \hat{b} , and γ_R^c, γ_c are the idler's coupling rates through the readout and loss ports, respectively³². Using the *same Hamiltonian method* as Section 2.2.1, the Heisenberg-Langevin equations-of-motion can then be found, where I again: (1) assume the semi-classical and no pump depletion approximations to the pump mode $\hat{u} \mapsto ue^{i\phi}$, (2) enter the Interaction Picture to ignore \hat{H}_0 , and (3) take fluctuating components but leave the $\delta\hat{Q}(t)$ implicit in the notation,

$$\begin{cases} \dot{\hat{b}} = -i\chi e^{i\phi}\hat{c}^\dagger - \gamma_{\text{tot}}^b\hat{b} + \sqrt{2\gamma_R^b}\hat{B}_{\text{in}} + \sqrt{2\gamma_b}\hat{n}_b^L \\ \dot{\hat{c}} = -i\chi e^{i\phi}\hat{b}^\dagger - \gamma_{\text{tot}}^c\hat{c} + \sqrt{2\gamma_R^c}\hat{C}_{\text{in}} + \sqrt{2\gamma_c}\hat{n}_c^L. \end{cases} \quad (2.12)$$

Here, $\chi = gu/2$ and $\gamma_{\text{tot}}^c = \gamma_R^c + \gamma_c$. Similarly to the degenerate case, I take Fourier transforms and find the vector equation for $\vec{\hat{d}}(\Omega) = (\hat{b}(\Omega), \hat{b}^\dagger(-\Omega), \hat{c}(\Omega), \hat{c}^\dagger(-\Omega))^T$ which now combines the signal and idler modes, with similar vectorisation for each mode, then I solve that equation algebraically. Using the input/output relation at the readout port [45], I then find the signal and idler quadratures at the photodetector.

The *total quantum noise response* (S_X) is found using Eq. 2.8³³ and assuming uncorre-

³¹Also assumed on resonance by the single-mode approximation.

³²Using dichroic optics can mean that these are different to the signal mode.

³³Here, the vector contains both signal and idler quadratures $\vec{\hat{X}} = (\hat{X}_{b,1}, \hat{X}_{b,2}, \hat{X}_{c,1}, \hat{X}_{c,2})^T$.

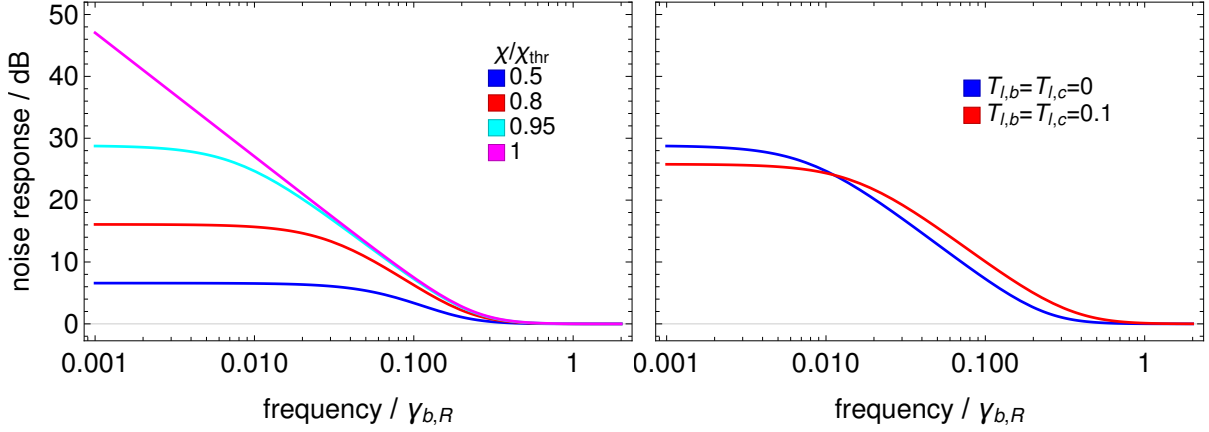


Figure 2.6: Nondegenerate OPO noise response, showing anti-squeezing in the signal mode, i.e. $\sqrt{(S_X)_{1,1}}$. The behaviour is similar to the anti-squeezed quadrature of the degenerate OPO in Fig. 2.5 because the cavity resonance is the same. Left panel: different squeezer parameters up to threshold with no loss. Right panel: different symmetric intra-cavity losses ($T_{l,b} = T_{l,c}$) for a fixed ratio of 95% threshold. The noise in the idler mode is similar [49]. I use a 1 m cavity with symmetric readout transmission $T_{R,b} = T_{R,c} = 0.1$.

lated vacuum between the signal and idler modes to be [49]

$$\begin{aligned}
 (S_X)_{1,1} = (S_X)_{2,2} &= 1 + \frac{8\gamma_R^b \gamma_{\text{tot}}^c \chi^2}{(\gamma_{\text{tot}}^b \gamma_{\text{tot}}^c - \chi^2)^2 + \Omega^2 (\gamma_{\text{tot}}^b{}^2 + \gamma_{\text{tot}}^c{}^2 + 2\chi^2) + \Omega^4} & (2.13) \\
 (S_X)_{3,1} = -(S_X)_{4,2} &= -\frac{\sin(\phi) 4\chi \sqrt{\gamma_R^b \gamma_R^c} (\chi^2 + \Omega^2 + \gamma_{\text{tot}}^b \gamma_{\text{tot}}^c + i\Omega (\gamma_{\text{tot}}^c - \gamma_{\text{tot}}^b))}{(\gamma_{\text{tot}}^b \gamma_{\text{tot}}^c - \chi^2)^2 + \Omega^2 (\gamma_{\text{tot}}^b{}^2 + \gamma_{\text{tot}}^c{}^2 + 2\chi^2) + \Omega^4} \\
 (S_X)_{3,3} = (S_X)_{4,4} &= ((S_X)_{1,1})|_{\hat{b} \leftrightarrow \hat{c}} \quad (S_X)_{4,1} = (S_X)_{3,2} = -\cot(\phi)(S_X)_{3,1}.
 \end{aligned}$$

Here, S_X is now divided into four 2-by-2 blocks: in the upper-left the signal variances and signal-signal covariance (which is zero), in the bottom-right the idler variances (equal to the signal variances under the exchange of rates $\gamma_R^b \leftrightarrow \gamma_R^c$ etc.) and idler-idler covariance (also zero), and in the off-diagonal blocks the signal-idler covariances which are not-zero but all closely related. Like the degenerate case, all expressions are rational functions, the variances are perturbations from the vacuum value of one, and the covariances obey the Hermitianity of S_X and vanish when the squeezer is off.

There are two main differences to the degenerate case: all the variances are now equally anti-squeezed³⁴, which will be explained later, and the signal and idler modes are corre-

³⁴Which makes them independent of the pump phase because no quadrature is squeezed. Here, anti-squeezing might be better referred to as amplification.

lated instead of the signal mode being correlated with itself. However, the effects of the squeezer parameter χ and the intra-cavity loss are similar to the anti-squeezed quadrature of the degenerate case as shown in Fig. 2.6, where threshold is now $\chi_{\text{thr}} = \sqrt{\gamma_{\text{tot}}^b \gamma_{\text{tot}}^c}$ by Eq. 2.13 [49, 48]³⁵.

Recovering squeezing

To explain why only anti-squeezing is seen in the nondegenerate case, I consider making a *coherently combined measurement of the signal and idler modes*. The motivation is that if the signal is measured, then the idler readout rate γ_R^c decoheres the signal measurement by Eq. 2.13, but if the idler mode is also measured then this readout rate would be useful, and vice versa. Consider a particular coherent³⁶, linear combination of the signal and idler quadratures at the photodetector, $\hat{X}_{\text{com}}(\Omega) = \frac{1}{\sqrt{2}}(\hat{X}_{\text{PD};b,1} + \hat{X}_{\text{PD};c,1})$ [49]. Then the combined variance is $S_{\text{com}} = \frac{1}{2}(S_X)_{1,1} + \frac{1}{2}(S_X)_{3,3} + \text{Re}[(S_X)_{3,1}]$. Here, the Hermitianity of S_X has been used and the vacuum value is still one³⁷. Although each variance, e.g. $(S_X)_{1,1}$, is anti-squeezed, the correlation $\text{Re}[S_{3,1}]$ can be sufficiently negative such that the combined variance is squeezed overall. The above choice of linear combination achieves the minimum variance which is equivalent, when the signal and idler losses are the same, to the squeezed variance from a degenerate OPO in Eq. 2.10 [51]³⁸. This explains that the degenerate and nondegenerate OPOs produce the same correlations between the photons from the down-conversion, but that in the nondegenerate case the modes have to be coherently combined to see the squeezing.

³⁵The signal and idler experience the same gain χ , which is half the gain of the degenerate case.

³⁶As opposed to an incoherent combination where the fields are detected separately and then their variances added.

³⁷In experiments, the combination is not normalised and so should be compared to a higher vacuum value, e.g. 2 for $\hat{X}_{b,1} + \hat{X}_{c,1}$. Experiments have measured S_{com} to calculate the correlations between the signal and idler $(S_X)_{3,1}$ and demonstrate quantum entanglement in tests of the Einstein-Podolsky-Rosen (EPR) paradox [50, 46, 49]. This historical association means that nondegenerate squeezing is commonly referred to as ‘‘EPR squeezing’’.

³⁸This linear combination is a Wiener filter, i.e. the optimum choice, for the quantum noise.

2.3 Quantum noise in gravitational-wave detectors

The quantum noise in measuring the gravitational-wave signal with a detector like that shown in Fig. 1.2 comes from two sources: (1) quantum shot noise and (2) quantum radiation-pressure noise [36, 37].

The quantum noise in the arrival time of the photons, i.e. the phase of the light, incident on the photodetector is called *quantum shot noise* [36]. The Poissonian behaviour of the arrival time of each photon leads to noise that is frequency-independent (i.e. “white”) and a measured signal-to-shot noise ratio $\propto \sqrt{P_{\text{circ}}}$ which improves with increased circulating power (P_{circ}) [37]. In the Hamiltonian modelling, the vacuum entering the readout and loss ports produces noise with the vacuum value of one uniformly across all frequencies and quadratures and, in particular, noise in the phase quadrature of the vacuum entering the readout port becomes shot noise in the measured phase quadrature at the photodetector. Although the shot noise remains at one, the above shot noise-limited sensitivity improves with power because the signal response does.

The optomechanical interaction with the test mass mechanical modes causes *quantum radiation-pressure noise* [36]³⁹. The fluctuating amplitude of the light, i.e. the number of photons, incident on a suspended optic produces a fluctuating force due to radiation pressure which becomes noise in the displacement of the optic and therefore in the propagation phase of the reflected light. This means that noise in the amplitude quadrature of the vacuum entering the readout port becomes radiation-pressure noise in the measured phase quadrature at the photodetector. This noise is described by the mechanical resonance(s) of the suspended test masses and can be approximated above their resonant frequencies (e.g. above ~ 10 Hz [52]) as though they are free-falling horizontally (i.e. are harmonic oscillators with a resonant frequency of 0 Hz and mass M [52]) with the signal-to-radiation pressure noise ratio $\propto M\Omega^2/\sqrt{P_{\text{circ}}}$ [37]. Here, the noise decreases as Ω^{-2} , is singular at DC ($\Omega = 0$) in this approximation, and increases with increased power. Therefore, as shown in Fig. 2.7, shot noise is the dominant source of quantum noise at kilohertz and I will focus on reducing shot noise through squeezing.

³⁹This can also be interpreted as back-action noise by making a precise measurement of the position \hat{x} at earlier times [38].

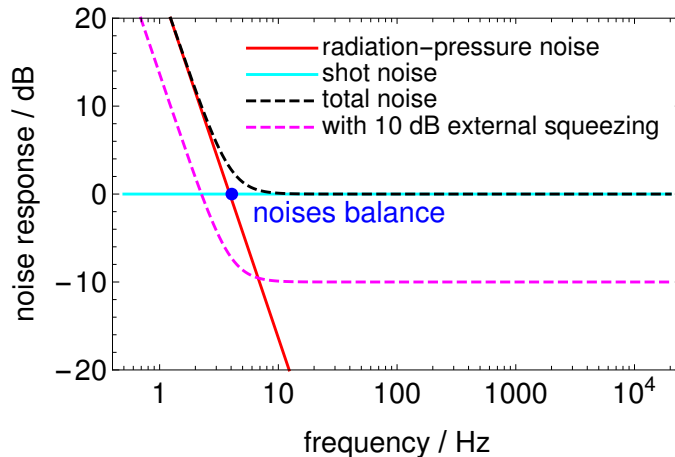


Figure 2.7: Quantum noise response of the detector shown in Fig. 1.2 to radiation-pressure noise, shot noise, and total quantum noise. I use the parameters in Table 3.1 (explained later) but with no losses. At kilohertz, shot noise is the dominant source of quantum noise. The point where the contributions from the two sources of quantum noise are equal is related to the Standard Quantum Limit which I will not discuss here because it is weaker than the Mizuno limit and can also be beaten by squeezing [19]. The total noise with 10 dB injected, frequency-dependent external squeezing is also shown, where 10 dB squeezing is also measured here because there are no losses.

2.3.1 Squeezing in current gravitational-wave detectors

The sensitivity of current gravitational-wave detectors is improved by injecting the squeezed vacuum from an external degenerate OPO into the readout port via a Faraday isolator as shown in Fig. 1.2 [42]⁴⁰. As the vacuum entering readout port is the dominant source of quantum noise in current gravitational-wave detectors, squeezing it reduces the shot noise in the measurement which improves sensitivity because the signal is not affected by external squeezing [53]. External squeezing is used in Advanced LIGO to improve the shot noise-limited sensitivity by a factor of 2 at ~ 200 Hz [42, 53]⁴¹. However, squeezing only the shot noise increases the radiation-pressure noise because they are associated with opposite quadratures of the input squeezed vacuum state. This means that, although the quantum noise around and above 100 Hz is improved, it is worsened below 100 Hz [42]. Current LIGO detectors are undergoing an upgrade to get a broad-band improvement in sensitivity by using a series of filter cavities to rotate the injected

⁴⁰Although essential, the Faraday isolator (also known as a circulator or directional beamsplitter) contributes significantly to the detection and injection losses, but the sensitivity is improved if the squeezing is high enough.

⁴¹This is far more practical than achieving the equivalent increase in circulating power.

squeezed states and squeeze the dominant source of quantum noise at each frequency as shown in Fig. 2.7 [33]. This *frequency-dependent external squeezing* is universally applicable ⁴² to quantum noise–limited detectors since there is always vacuum entering the readout port, and, therefore, I will not include it in my work when comparing different configurations.

2.4 Chapter summary

In this chapter, I have revised the necessary quantum mechanics to explain the benefits of squeezing for gravitational-wave detectors. Firstly, I set up a mathematical framework for the quantum noise in the quadratures of the light inside a detector. I introduced the idea of squeezing to reduce the quantum noise by using a nonlinear crystal. Then, I showed how squeezing can be understood using the analytic Hamiltonian modelling that I will use throughout this thesis. Finally, I explained the different sources of quantum noise in a gravitational-wave detector and how external squeezing is currently used to improve the quantum noise–limited sensitivity of Advanced LIGO.

⁴²Technically, the tolerance of each configuration to the readout port loss versus the other losses affects the sensitivity improvement with external squeezing. However, the readout port is typically the main vacuum source and this is a simple enough addition to future work.

Existing proposals for improving kilohertz sensitivity

In this chapter, I critically examine two of the existing configurations that address the problem of increasing kilohertz sensitivity: degenerate internal squeezing in Section 3.1 and stable optomechanical filtering in Section 3.2. I present the limitations of these two proposals to motivate my work in subsequent chapters into a configuration that combines their strengths but might be able to overcome their limitations and better improve kilohertz sensitivity.

3.1 Degenerate internal squeezing

Degenerate internal squeezing consists of a degenerate squeezer placed inside the signal-recycling cavity of the detector in Fig. 1.2 such that it squeezes the signal mode as shown in Fig. 3.1 [23]. In this configuration, the vacuum entering the readout port is squeezed (as with external squeezing) and the vacuum from the intra-cavity losses and the gravitational-wave signal are also squeezed (unlike external squeezing)¹. The signal comes from the test masses in the arms and the noise comes predominantly from the vacuum entering the readout port. This means that the signal and noise “see” the signal-recycling cavity and the squeezer differently as shown in Fig. 3.1. Therefore, degenerate internal squeezing improves sensitivity, i.e. the signal-to-noise ratio, by squeezing the noise more than the signal as shown in Fig. 3.1 [23].

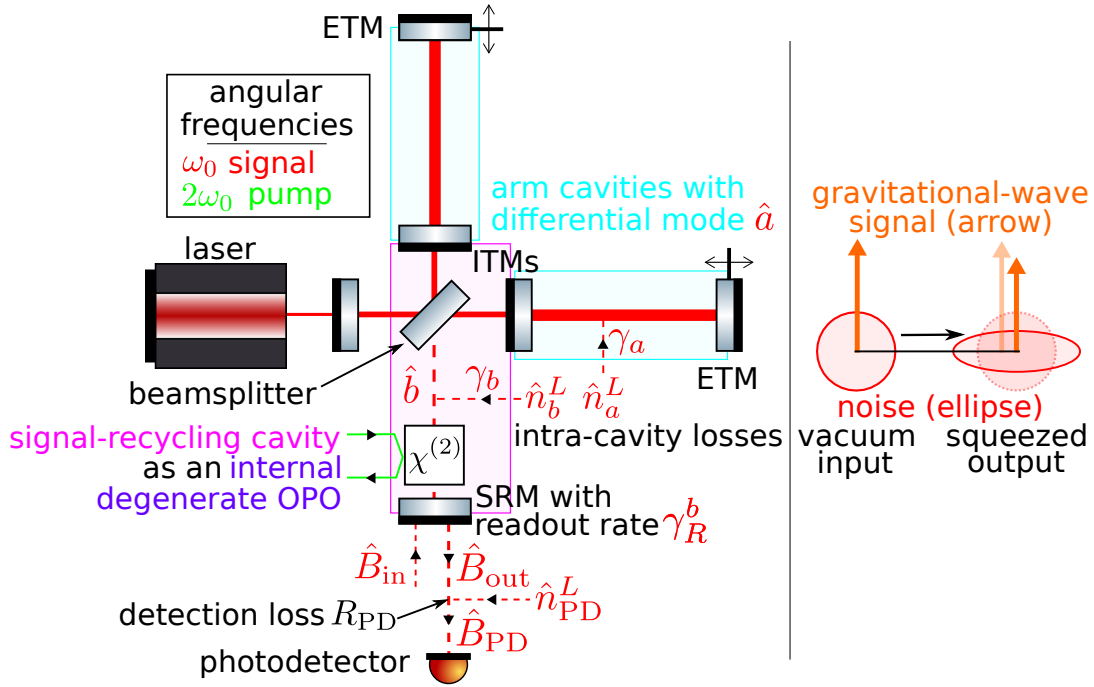


Figure 3.1: Degenerate internal squeezing configuration (left panel), and the squeezer’s effect on the measured signal and noise (right panel) using a noise ellipse and signal arrow representation where the height of the arrow represents the signal response. The signal-recycling cavity resembles the degenerate OPO in Fig. 2.3. Detection loss (R_{PD}) is included in the output field (\hat{B}_{out}) via the beamsplitter convention in Fig. 2.4. The signal enters the detector by moving the end test masses and the noise enters as vacuum from the readout port and losses. The sensitivity is improved by squeezing the noise more than the signal is decreased.

3.1.1 Understanding the behaviour using a Hamiltonian model

My work in the following chapters will follow a similar method to that presented below for degenerate internal squeezing which, accordingly, I show in detail.

Using the *Hamiltonian model* from Ref. [23]², let the interaction Hamiltonian be

$$\hat{H}_I = i\hbar\omega_s(\hat{a}\hat{b}^\dagger - \hat{a}^\dagger\hat{b}) + \frac{\hbar\chi}{2}(e^{i\phi}(\hat{b}^\dagger)^2 - e^{-i\phi}\hat{b}^2). \quad (3.1)$$

Here \hat{a} is the differential arm cavity mode³ at the carrier frequency ω_0 coupled to the signal-recycling cavity signal mode \hat{b} with coupling rate (called the “sloshing” frequency) ω_s determined by the transmission through the input test mass and the lengths of the two

²With an added factor of $\sqrt{2}$ to G_0 from that reference to match the convention for the gravitational-wave coupling constant α_{GW} from Ref. [1] that I use in Chapter 4.

³I assume that the Michelson interferometer is tuned such that the light from the arms destructively interferes at the output of the beamsplitter, called the “dark port” [13].

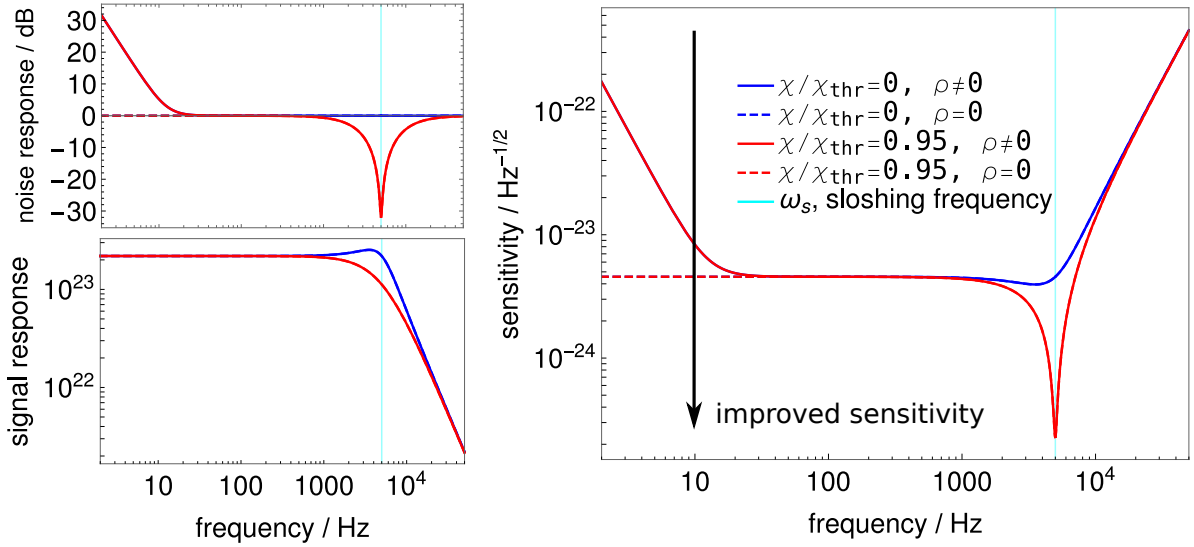


Figure 3.2: Degenerate internal squeezing’s quantum noise response (upper-left panel), gravitational-wave signal response (bottom-left panel), and sensitivity (right panel) without optical losses. The squeezer (red curves) improves sensitivity around the slushing frequency compared to the detector without squeezing (blue curves). The quantum noise response is shown in dB and the signal response is unitless [38]. The sensitivity is conventionally shown as the noise-to-signal ratio in $\text{Hz}^{-1/2}$ and henceforth the goal is to lower the sensitivity curve. I use the parameters in Table 3.1. The readout rate (γ_R^b) determines the width of the squeezing peak centred on the slushing frequency (ω_s). The radiation-pressure coupling constant (ρ , explained later) controls whether radiation-pressure noise is seen below ~ 10 Hz ($\rho \neq 0$) or not ($\rho = 0$).

carrier wavelength, λ_0	$2 \mu\text{m}$	slushing frequency, ω_s	5 kHz
arm cavity length, L_{arm}	4 km	signal mode transmissivity, $T_{\text{SRM},b}$	0.046
signal-recycling cavity length, L_{SRC}	112.4 m	signal readout rate, γ_R^b	5 kHz
circulating arm power, P_{circ}	3 MW	arm intra-cavity loss, $T_{l,a}$	100 ppm
test mass mass, M	200 kg	signal mode intra-cavity loss, $T_{l,b}$	1000 ppm
input test mass transmissivity, T_{ITM}	0.0197	detection loss, R_{PD}	10%

Table 3.1: Parameter set based on LIGO Voyager [54] but with deviations to achieve the slushing frequency and readout rate shown. In particular, the signal-recycling cavity is made longer to increase the peak sensitivity via narrowing the peak. I use realistic future optical losses [55, 56] in parts-per-million (ppm). There is debate about $2 \mu\text{m}$ versus $1.064 \mu\text{m}$ as the preferred carrier wavelength [57], but I will only consider $2 \mu\text{m}$.

coupled cavities [23]. The second term in the Hamiltonian is the same as the degenerate OPO in Section 2.2.1 ⁴. The model also includes an intra-cavity loss port in the arms with transmissivity $T_{l,a}$ to vacuum \hat{n}_a^L as shown in Fig. 3.1 ⁵. Using this model, the sensitivity of the detector to a gravitational-wave strain $h(t)$ is the signal-to-noise ratio $\frac{|T|}{\sqrt{S_X}}$ in the measured quadrature $\hat{X}_{\text{PD}}(\Omega) = \sum_i R_i \hat{X}_i^{\text{vac}}(\Omega) + T\tilde{h}(\Omega)$, given by the noise $\sqrt{S_X}$ and signal T responses (also called “transfer functions”). However, I will plot the noise-to-signal ratio throughout this thesis, i.e. $\sqrt{S_h} = \frac{\sqrt{S_X}}{|T|}$ which has units of $\text{Hz}^{-1/2}$ [38], as it is the convention in the gravitational-wave literature (e.g. see Ref. [12]), and, therefore, smaller values in $\text{Hz}^{-1/2}$ indicate better sensitivity.

The resulting *noise and signal responses and the sensitivity* are shown in Fig. 3.2 without optical losses and for the parameter set of LIGO Voyager but with a readout rate of 5 kHz ⁶ as shown in Table 3.1. LIGO Voyager [54] is a planned series of upgrades to the Advanced LIGO detectors that I use throughout this thesis to represent the next generation of gravitational-wave detectors. The squeezer parameter χ affects the sensitivity as shown in Fig. 3.2 and needs to be optimised for each configuration separately. With the squeezer turned off, the configuration becomes the detector in Fig. 1.2. Turning the squeezer on (1) squeezes the shot noise and de-amplifies the signal around the sloshing frequency ω_s , (2) does not affect the radiation-pressure noise below 100 Hz, and therefore (3) improves sensitivity around the sloshing frequency while not affecting it at lower frequencies. Threshold in the lossless case is $\chi_{\text{thr}} = \gamma_R^b$ where the squeezed noise goes to zero at $\Omega = \omega_s$ ⁷. In the lossy case, the situation is more complicated and the threshold is not quoted in the literature, which I will address in Section 4.4.2. Since configurations must be stable to be feasible, I confirm that degenerate internal squeezing is stable below threshold in Appendix A. Degenerate internal squeezing can be operated in two regimes depending on the choice of the sloshing frequency (ω_s) and the bandwidth of the signal-recycling cavity (γ_R^b) ⁸: (1) broadband sensitivity when γ_R^b is large (e.g. L_{SRC} is short) and the sensitivity is improved typically from around 0.1 to 10 kHz [23] or (2)

⁴Up to the phase of the pump.

⁵Ref. [23] does not include this but I include it in my model for completeness.

⁶I increase the readout rate from 0.5 to 5 kHz but keep the sloshing frequency fixed at 5 kHz by shortening the signal-recycling cavity and decreasing the transmission through the input test mass.

⁷And the anti-squeezed quadrature diverges.

⁸Not to be confused with the overall bandwidth of the signal response which is from the arm cavities.

kilohertz sensitivity when γ_R^b is small (e.g. L_{SRC} is long) and the sensitivity is narrowly, but strongly, improved around ω_s (e.g. 5 kHz) by more than an order of magnitude at the peak as shown in Fig. 3.2 [24]. I consider this latter regime because I am interested in kilohertz improvement.

With degenerate internal squeezing, the squeezing of the shot noise and signal is localised to the sloshing frequency because of the *resonance structure of the coupled cavity system*. At the sloshing frequency, energy is strongly coupled from the arm cavity into the signal-recycling cavity which becomes resonant⁹ [58]. As the squeezer is only effective when the cavity is resonant, e.g. the squeezing drops off beyond γ_R^b away from the peak in Fig. 2.5, the signal and noise are only squeezed around the sloshing frequency. Away from the sloshing frequency, the cavity is not resonant and degenerate internal squeezing does not affect the sensitivity¹⁰.

3.1.2 Limitation: tolerance to optical loss

Degenerate internal squeezing has different tolerances to the three types of optical loss it experiences: detection loss in the readout, intra-cavity loss in the signal mode of the signal-recycling cavity, and intra-cavity loss in the arms. The general effects of these losses are shown in Fig. 3.3. Firstly, detection loss uniformly pulls the noise towards the vacuum and pulls the signal towards zero because it uniformly mixes in vacuum. Secondly, signal intra-cavity loss behaves differently to the degenerate OPO, as the noise response remains within the lossless envelope, the radiation-pressure noise is increased, and the signal and noise are worsened around the sloshing frequency. Finally, arm intra-cavity loss diminishes the squeezing of the noise, worsens the DC response to the signal, but improves the radiation-pressure noise.

With losses included in the model, the *optimal squeezing* can be below threshold [25]. For example, once the noise is limited by detection loss, which is not squeezed by the internal squeezer, further squeezing will only decrease the signal and the sensitivity. Moreover, in

⁹The phase acquired upon reflecting off the input test mass depends on whether the arm cavity is resonant and means that the signal-recycling cavity can be chosen to be resonant at frequencies where the arm cavity is not resonant. At the sloshing frequency, the arm cavity is not resonant, as seen in the falling signal response in Fig. 3.2.

¹⁰Assuming that the arm cavity loss is realistically small.

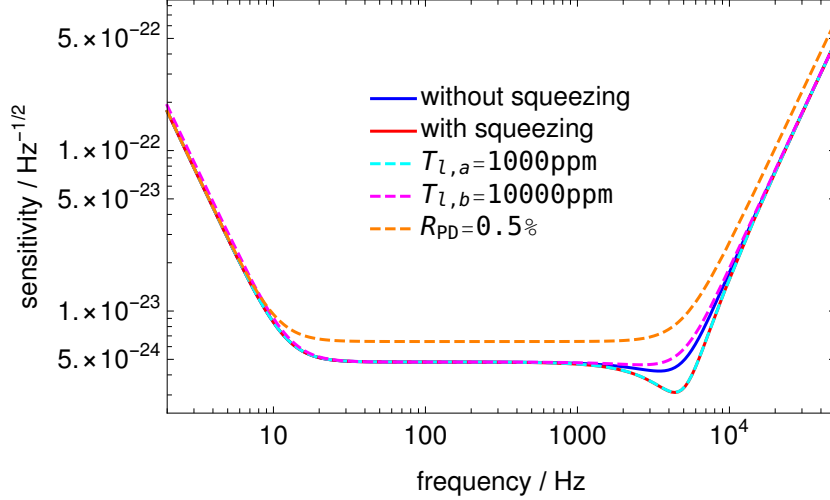


Figure 3.3: Degenerate internal squeezing sensitivity for realistic losses. The dashed curves show the effect on the sensitivity of increasing the loss from the realistic value in Table 3.1 to show the tolerance to each loss. Increasing each of the three losses separately shows that realistic arm loss ($T_{l,a}$) is negligible (the cyan curve lies on top of the red curve), signal mode loss ($T_{l,b}$) decreases the peak sensitivity (i.e. diminishes the trough shown around 4 kHz but I will refer to this as a “peak” henceforth), and detection loss (R_{PD}) broadly decreases sensitivity. This means that the detection loss dominates the losses but the signal loss would matter around the peak if it was worse than the desired 1000 ppm. I use the parameters in Table 3.1.

the high loss regime, any amount of squeezing is detrimental and it is instead optimal to anti-squeeze internally [25]. This improves sensitivity because the signal is anti-squeezed more than the noise, and also improves the tolerance to losses because they now decrease the signal and the noise since the noise is above the vacuum value ¹¹. However, future detectors do not belong to this high loss regime.

If the *realistic losses* in Table 3.1 ¹² are assumed, then the sensitivity improvement significantly degrades to less than a factor of two at the sloshing frequency as shown in Fig. 3.3 compared to the lossless case in Fig. 3.2 that improved it by over an order of magnitude. For these realistic losses, detection loss is responsible for most of the degradation seen in Fig. 3.3 since it dominates the noise apart from the readout port vacuum. The low tolerance to detection loss of degenerate internal squeezing motivates investigating other methods which might improve sensitivity more given the same losses.

I emphasise two aspects of this configuration: (1) its dependence on the optomechanical and optical coupling rates and (2) its vulnerability to mechanical loss. In the lossless case, comparing the coupling rates of the arm and the signal, and the signal and the mechanical idler, shows that when the two coupling rates are equal, the behaviour is exceptional. Let the interaction Hamiltonian of the system be [1] ¹⁵

$$\hat{H}_I = i\hbar\omega_s(\hat{a}\hat{b}^\dagger - \hat{a}^\dagger\hat{b}) + i\hbar\chi_m(\hat{b}^\dagger\hat{c}_m^\dagger - \hat{b}\hat{c}_m). \quad (3.2)$$

Here $\hat{a}, \hat{b}, \omega_s$ are the same notation as degenerate internal squeezing, \hat{c}_m annihilates the mechanical mode, and χ_m is the optomechanical coupling rate. When this coupling rate χ_m equals the sloshing frequency (ω_s), the interaction Hamiltonian becomes invariant under the transformation $\hat{a} \mapsto \hat{c}_m^\dagger, \hat{c}_m \mapsto \hat{a}^\dagger$ which corresponds to the composition of parity, $\hat{a} \leftrightarrow \hat{c}_m$, and time, $\hat{a} \leftrightarrow \hat{a}^\dagger, \hat{c}_m \leftrightarrow \hat{c}_m^\dagger$, transformations, and that leaves \hat{b} invariant. This *parity-time (PT) symmetry* causes other changes in the system, namely, the lossless, PT-symmetric system is borderline stable, with one complex Ω pole on the real axis; is at an Exceptional Point of its eigenmodes as two or more eigenvalues are degenerate; and the shot noise-limited, integrated sensitivity becomes unbounded [1] ¹⁶. With radiation pressure included in the model ¹⁷, the integrated sensitivity becomes bounded and, although the kilohertz sensitivity improves, the main improvement is from 100-1000 Hz.

3.2.1 Limitation: tolerance to mechanical loss

Stable optomechanical filtering could potentially improve the sensitivity of future detectors but addressing its vulnerability to *mechanical loss* demands progress beyond current technology. Mechanical loss damps the mechanical mode due to the dissipation of energy into the thermal bath of the mass and its surroundings. This raises the temperature of the mass and increases the thermal noise, which becomes radiation pressure noise in the filter cavity mode, and then degrades sensitivity. The thermal noise from me-

¹⁵This is similar to the Hamiltonian I will use in my work which I will detail in Chapter 4.

¹⁶A review of PT-symmetry is given in Ref. [60]. I leave checking that the PT-symmetry causes this sensitivity improvement to future work.

¹⁷There is a complication with radiation pressure coupling the arm cavity mode to the test mass mechanical mode, as for PT-symmetry to be maintained the filter cavity mechanical mode must then be coupled to a back-action evasion mode with negative effective mass [1], but I will not consider this for simplicity.

chanical loss dominates the losses of stable optomechanical filtering [1]. The results in Ref. [1] assume the ratio of the environmental temperature T_{env} to quality factor Q_m to be small, i.e. $T_{\text{env}}/Q_m \leq \hbar\gamma_{\text{single-cavity}}/(8k_B) \approx 6 \times 10^{-10}K$ [26]. Here $\gamma_{\text{single-cavity}}$ is the bandwidth of the Fabry-Perot Michelson interferometer, i.e. without the signal-recycling cavity, and k_B is the Boltzmann constant. The quality factor required to satisfy this bound is $Q_m = 8 \times 10^9$ [26] which is beyond that possible with current technology [61, 31]. Therefore, an all-optical alternative ¹⁸ is appealing because the losses required might be more realistic; this is the focus of my work in the following chapters.

3.3 Chapter summary

In this chapter, I have reviewed two configurations proposed to improve the kilohertz sensitivity of future gravitational-wave detectors: degenerate internal squeezing and stable optomechanical filtering. The low tolerance to realistic losses limits the feasibility of these two configurations. This motivates investigating configurations that are more resistant to loss.

¹⁸Since all other systems that use optomechanical filtering have the same requirement [26].

Analytic model of nondegenerate internal squeezing

In this chapter, I present my analytic Hamiltonian model of nondegenerate internal squeezing and discuss its results. Firstly, in Section 4.1, I describe nondegenerate internal squeezing and how it is motivated by the existing proposals introduced in the previous chapter. Secondly, in Sections 4.2 and 4.3, I derive my model and use it to characterise the sensitivity of nondegenerate internal squeezing. Finally, in Section 4.4, I find the stability and squeezing threshold of the configuration. This chapter is directed at understanding nondegenerate internal squeezing for general quantum metrology. In subsequent chapters, I will return to the problem of kilohertz gravitational-wave detection.

4.1 Motivation

Nondegenerate internal squeezing consists of a nondegenerate squeezer placed inside the signal-recycling cavity of the detector in Fig. 1.2 as shown in Fig. 4.1 [1]. It is the same configuration as degenerate internal squeezing except that the squeezer is operated nondegenerately – similar to the relationship between the nondegenerate and degenerate OPOs in Section 2.2. The central idea is to anti-squeeze the noise¹ but amplify the signal more, as shown in Fig. 4.1, to improve sensitivity (the signal-to-noise ratio). As a general principle [39], when the noise is anti-squeezed a given optical loss decreases the noise towards the vacuum value of one, but when the signal is amplified it decreases towards

¹I will show that the noise is amplified in all quadratures which means that “anti-squeezing” is “amplifying” here.

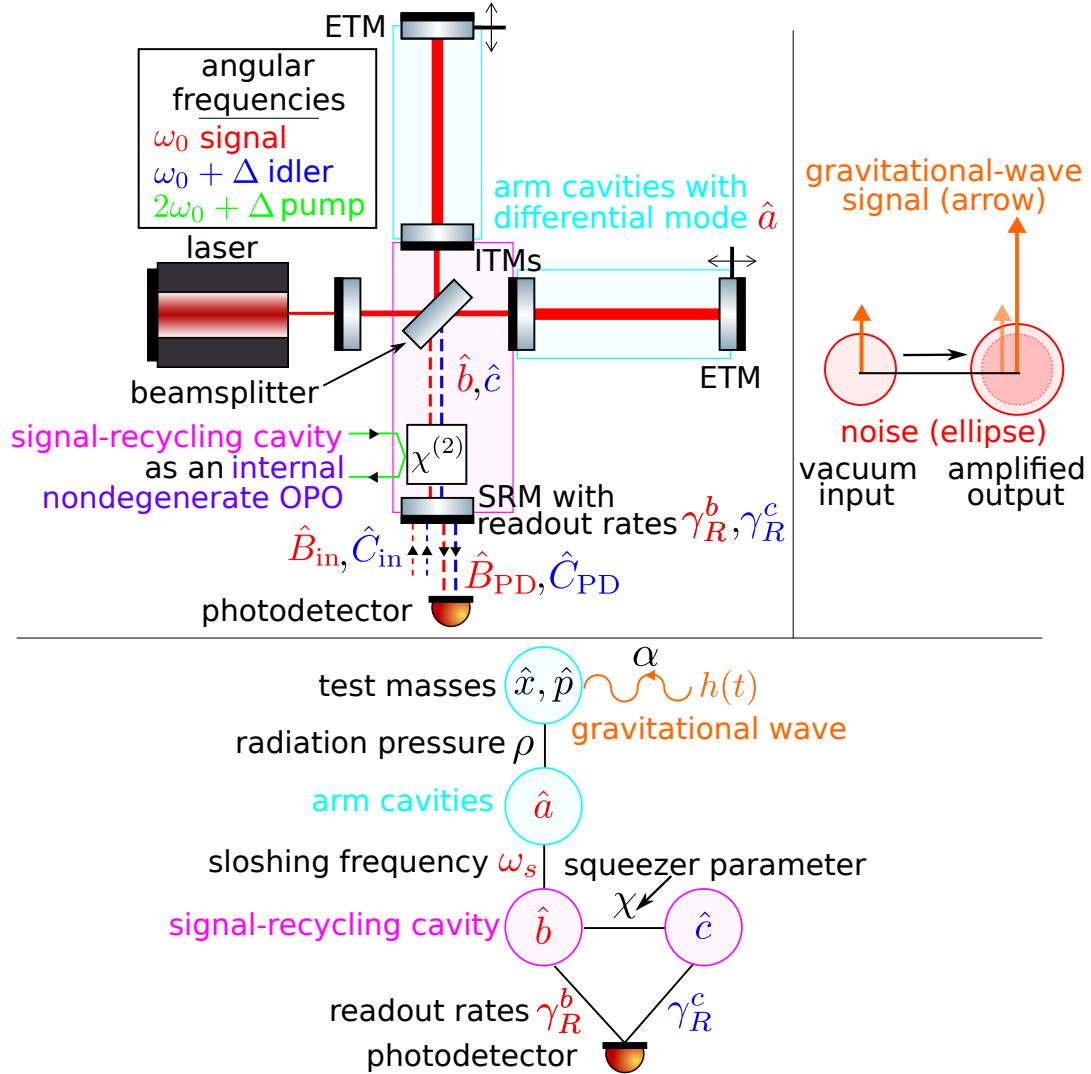


Figure 4.1: Nondegenerate internal squeezing configuration (upper-left panel), simplified effect on the signal and noise using the representation introduced in Fig. 3.1 (upper-right panel), and abstract mode diagram (bottom panel). The signal-recycling cavity resembles the nondegenerate OPO in Fig. 2.3. Abstractly, the system consists of three coupled optical modes $\hat{a}, \hat{b}, \hat{c}$ through which the gravitational-wave signal is coupled and measured at the photodetector. The noise is increased but the gravitational-wave signal is amplified more so that the sensitivity improves. Optical losses are not shown.

zero by the same ratio as when it is not amplified ². Therefore, if nondegenerate internal squeezing works as shown in Fig. 4.1 ³, then the decrease in sensitivity caused by a given loss would be less than the decrease without anti-squeezing because in the latter case the noise is already at the vacuum value and does not change with the loss. This resistance to loss would increase with the amount of anti-squeezing until, in the limit, the decreases in signal and noise would be the same and the sensitivity would not change. This motivates nondegenerate internal squeezing since it might be more resistant to optical loss than, for example, degenerate internal squeezing.

The *abstract structure of the coupled modes* of nondegenerate internal squeezing is shown in Fig. 4.1. Here, while both the signal and idler modes are resonant in the signal-recycling cavity, only the signal mode \hat{b} is resonant in the arms so that the differential arm \hat{a} and idler \hat{c} modes are not directly coupled. Nondegenerate internal squeezing is equivalent to stable optomechanical filtering under the mapping of the optical idler mode \hat{c} at $\omega_0 + \Delta$ and squeezer parameter χ to the mechanical idler mode \hat{c}_m at ω_m and optomechanical coupling χ_m , respectively, in the Hamiltonian [1]. I represent this in Appendix B where I compare their mode structures. In this sense, nondegenerate internal squeezing is an all-optical analogue of the optomechanical configuration. Moreover, the loss mechanisms in the two configurations are equivalent under the same mapping which maps intra-cavity idler optical loss to mechanical idler loss. However, in practice, the two configurations are not equivalent because of the different realistic levels of optical and mechanical loss. This motivates investigating nondegenerate internal squeezing since its loss requirements might be more realistic than the optomechanical analogue's to achieve the same sensitivity.

4.2 Analytic Hamiltonian model

I model nondegenerate internal squeezing using the Hamiltonian method from Section 2.2 which was also used to model the results for degenerate internal squeezing in Section 3.1.1 [23] and stable optomechanical filtering in Ref. [1]. When deriving my model, my approach was to start with the lossless model for the optomechanical analogue in

²Because the loss mixes in vacuum which has noise but no signal

³Which I will show to be the case.

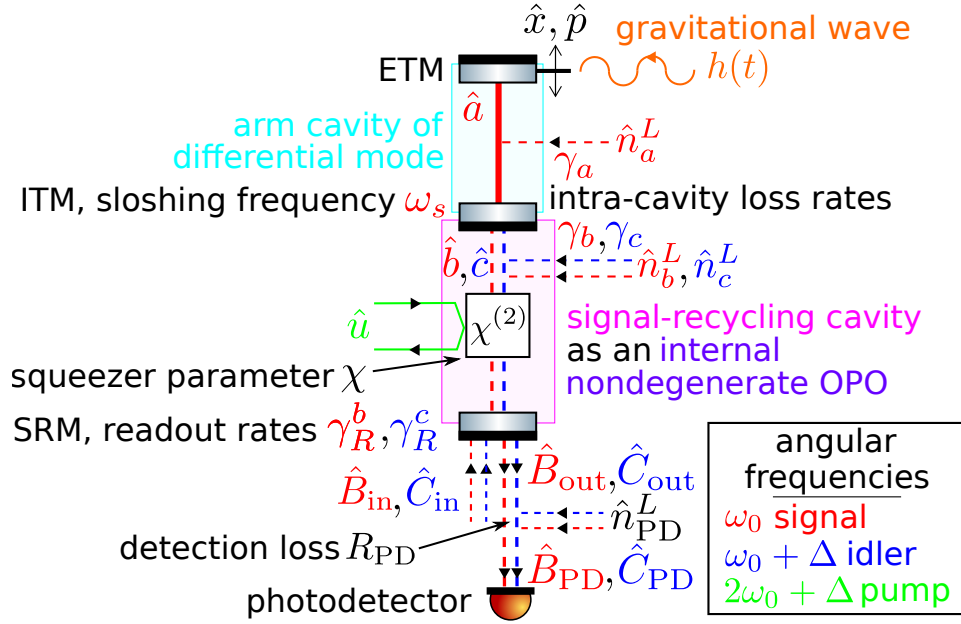


Figure 4.2: Nondegenerate internal squeezing configuration simplified from Fig. 4.1 for modelling. All modes and losses are explained in the text. I simplify the arm cavities in Fig. 4.1 into a single cavity that represents the single-mode approximation to the differential mode \hat{a} .

Ref. [1] and progressively add the complexities of optical loss in each mode, pump phase, and radiation pressure so that I could study each complication separately. At each stage, I verified that the model recovered the previous stage in the appropriate limits. For brevity, I now present the complete model.

Let the modes be labelled as shown in Fig. 4.2. Here, I assume a single-mode approximation to the light in the arm cavities such that the detector in Fig. 4.1 is simplified to a three-mirror coupled cavity system between a single “arm” cavity, with resonant mode as the differential mode \hat{a} of the detector, and the signal-recycling cavity⁴. This “coupled-cavity” approximation is common in the literature [24, 1, 26], was used in the degenerate internal squeezing model in Section 3.1 [23], and is valid below one “free spectral range” of the arm cavities (e.g. below 37.5 kHz for 4 km arms [26]). To the nondegenerate OPO model in Section 2.2.2, I add the differential arm cavity mode \hat{a} at carrier frequency ω_0 with an intra-cavity loss port with transmissivity $T_{l,a}$ into vacuum \hat{n}_a^L , and detection loss R_{PD} into vacuum \hat{n}_{PD}^L modelled using the beamsplitter convention from Fig. 2.4⁵. Let the gravitational-wave signal $h(t)$ from Section 1.1 be coupled to the arm cavity mode by

⁴The laser source and the power-recycling cavity are abstracted into the fixed circulating power in the arm cavity.

⁵I assume that the detection loss R_{PD} is symmetric between the signal and idler.

the test mass mechanical mode given by displacement \hat{x} and momentum \hat{p} (approximated as free-falling horizontally as explained in Section 2.3). The *Hamiltonian* of this system is $\hat{H} = \hat{H}_0 + \hat{H}_I + \hat{H}_\gamma + \hat{H}_{\text{GW+RP}}$ where [1]

$$\begin{aligned}
\hat{H}_0 &= \hbar\omega_0\hat{a}^\dagger\hat{a} + \hbar\omega_0\hat{b}^\dagger\hat{b} + \hbar(\omega_0 + \Delta)\hat{c}^\dagger\hat{c} + \hbar(2\omega_0 + \Delta)\hat{u}^\dagger\hat{u} \\
\hat{H}_I &= i\hbar\omega_s(\hat{a}\hat{b}^\dagger - \hat{a}^\dagger\hat{b}) + \hbar\frac{g}{2}(\hat{u}\hat{b}^\dagger\hat{c}^\dagger + \hat{u}^\dagger\hat{b}\hat{c}) \\
\hat{H}_\gamma &= i\hbar\sqrt{2} \int \left(\sqrt{\gamma_a} (\hat{a}^\dagger(\Omega)\hat{n}_a^L(\Omega) - \hat{a}(\Omega)\hat{n}_a^{L\dagger}(\Omega)) \right. \\
&\quad + \sqrt{\gamma_R^b} (\hat{b}^\dagger(\Omega)\hat{B}_{\text{in}}(\Omega) - \hat{b}(\Omega)\hat{B}_{\text{in}}^\dagger(\Omega)) + \sqrt{\gamma_b} (\hat{b}^\dagger(\Omega)\hat{n}_b^L(\Omega) - \hat{b}(\Omega)\hat{n}_b^{L\dagger}(\Omega)) \\
&\quad \left. + \sqrt{\gamma_R^c} (\hat{c}^\dagger(\Omega)\hat{C}_{\text{in}}(\Omega) - \hat{c}(\Omega)\hat{C}_{\text{in}}^\dagger(\Omega)) + \sqrt{\gamma_c} (\hat{c}^\dagger(\Omega)\hat{n}_c^L(\Omega) - \hat{c}(\Omega)\hat{n}_c^{L\dagger}(\Omega)) \right) d\Omega \\
\hat{H}_{\text{GW+RP}} &= -\alpha(\hat{x} - L_{\text{arm}}h(t)) \left(\frac{\hat{a} + \hat{a}^\dagger}{\sqrt{2}} \right) + \frac{1}{2\mu}\hat{p}^2.
\end{aligned} \tag{4.1}$$

Here, $\alpha = \sqrt{\frac{2P_{\text{circ}}\omega_0\hbar}{cL_{\text{arm}}}}$ is the coupling strength to the gravitational-wave signal [1]⁶, $\mu = M/4$ is the “reduced” mass of the test masses of mass M , and $\omega_s \approx c\sqrt{\frac{T_{\text{ITM}}}{4L_{\text{arm}}L_{\text{SRM}}}}$ is an approximation of the sloshing frequency between the coupled cavities (also known as the coupled cavity pole) which holds when ω_s (e.g. 5 kHz) is below one free spectral range of the arm cavities (e.g. 37.5 kHz) [23]. Of these terms in the Hamiltonian, \hat{H}_0 describes the decoupled optical system, \hat{H}_I describes the interaction between the optical modes including the same nondegenerate squeezing as Section 2.2.2, \hat{H}_γ describes the input/output coupling through the readout and loss ports, and $\hat{H}_{\text{GW+RP}}$ describes the coupling of the arm cavity mode to the gravitational-wave signal and the evolution of the test mass mechanical mode due to radiation pressure⁷. As shown in Fig. 4.2, there is vacuum entering the system into each intra-cavity mode $\hat{n}_a^L, \hat{n}_b^L, \hat{n}_c^L$, at the readout port $\hat{B}_{\text{in}}, \hat{C}_{\text{in}}$, and in the detection chain \hat{n}_{PD}^L (which will be included later). Only the vacuum entering the readout port was present in the lossless model in Ref. [1].

The *Heisenberg-Langevin equations-of-motion* for this system can be found using the bosonic commutation relations, the canonical commutation relation $[\hat{x}, \hat{p}] = i\hbar$, and with

⁶I use the value of α from Ref. [1] which is $\sqrt{2}$ more than the convention used in Ref. [23] for example.

⁷A more natural formulation of $\hat{H}_{\text{GW+RP}}$ couples the gravitational-wave strain to the mirror position and the mirror position to the cavity mode, as shown in Fig. 4.1, but the formula that I use is equivalent [62].

all other commutators zero. As in Section 2.2.2, I (1) make semi-classical and no-pump-depletion approximations that are valid below threshold to simplify the pump mode $\hat{u} \mapsto ue^{i\phi} = 2\chi/ge^{i\phi}$, (2) enter the Interaction Picture to ignore the decoupled evolution from \hat{H}_0 , and (3) take fluctuating components of each operator implicitly in the notation $\delta\hat{Q}(t) \mapsto \hat{Q}$ because it does not change the equations-of-motion. I find the equations-of-motion to be

$$\begin{cases} \dot{\hat{a}} = -\omega_s \hat{b} - \gamma_a \hat{a} + \sqrt{2\gamma_a} \hat{n}_a^L + \frac{i}{\hbar} \alpha (\hat{x} - L_{\text{arm}} h) \frac{1}{\sqrt{2}} \\ \dot{\hat{b}} = \omega_s \hat{a} - i\chi e^{i\phi} \hat{c}^\dagger - \gamma_{\text{tot}}^b \hat{b} + \sqrt{2\gamma_R^b} \hat{B}_{\text{in}} + \sqrt{2\gamma_b} \hat{n}_b^L \\ \dot{\hat{c}} = -i\chi e^{i\phi} \hat{b}^\dagger - \gamma_{\text{tot}}^c \hat{c} + \sqrt{2\gamma_R^c} \hat{C}_{\text{in}} + \sqrt{2\gamma_c} \hat{n}_c^L \\ \dot{\hat{x}} = \frac{1}{\mu} \hat{p} \\ \dot{\hat{p}} = \alpha \left(\frac{\hat{a} + \hat{a}^\dagger}{\sqrt{2}} \right). \end{cases} \quad (4.2)$$

I solve these equations in the *Fourier domain*. As in Section 2.2.2, let $\vec{\hat{d}}(\Omega) = (\hat{b}(\Omega), \hat{b}^\dagger(-\Omega), \hat{c}(\Omega), \hat{c}^\dagger(-\Omega))^T$, where I use the compact notation $\delta\hat{Q}(\Omega) \mapsto \hat{Q}(\Omega)$ for the Fourier transform of each mode, with similar signal-idler vectorisation for each signal and idler mode, e.g. $\vec{\hat{D}}_{\text{in}}(\Omega)$, $\vec{\hat{n}}_d^L(\Omega)$ ⁸. Let $\vec{h}(\Omega) = \tilde{h}(\Omega)(1, 1, 0, 0)^T$ (since $h(t)$ is real, $\tilde{h}(\Omega) = \tilde{h}(-\Omega)^*$), $\vec{\hat{a}}(\Omega) = (\hat{a}(\Omega), \hat{a}^\dagger(-\Omega), 0, 0)^T$ ⁹, and similarly for $\vec{\hat{n}}_a^L(\Omega)$. By Fourier transforming, vectorising, and then solving the resulting linear algebraic equations for $\vec{\hat{d}}(\Omega)$ using a similar process to Section 2.2, I find that the signal and idler intra-cavity modes, in terms of each vacuum input and the gravitational-wave signal, are

$$\vec{\hat{d}}(\Omega) = M_d^{-1} \left(\omega_s \begin{bmatrix} 1 & & & \\ & 1 & & \\ & & 0 & \\ & & & 0 \end{bmatrix} M_a^{-1} \left(\sqrt{2\gamma_a} \begin{bmatrix} 1 & & & \\ & 1 & & \\ & & 0 & \\ & & & 0 \end{bmatrix} \vec{\hat{n}}_a^L(\Omega) - i\beta \begin{bmatrix} 1 & & & \\ & -1 & & \\ & & 0 & \\ & & & 0 \end{bmatrix} \vec{h}(\Omega) \right) \quad (4.3)$$

$$+ \sqrt{2} \begin{bmatrix} \sqrt{\gamma_R^b} & & & \\ & \sqrt{\gamma_R^b} & & \\ & & \sqrt{\gamma_R^c} & \\ & & & \sqrt{\gamma_R^c} \end{bmatrix} \vec{\hat{D}}_{\text{in}}(\Omega) + \sqrt{2} \begin{bmatrix} \sqrt{\gamma_b} & & & \\ & \sqrt{\gamma_b} & & \\ & & \sqrt{\gamma_c} & \\ & & & \sqrt{\gamma_c} \end{bmatrix} \vec{\hat{n}}_d^L(\Omega) \quad (4.4)$$

$$M_a = (\gamma_a - i\Omega)\mathbf{I} + \frac{i\rho}{\Omega^2\sqrt{2}} \begin{bmatrix} 1 & & & \\ & 1 & & \\ & & -1 & \\ & & & -1 \end{bmatrix}$$

⁸Where the notation d indicates a similar vector to $\vec{\hat{d}}(\Omega)$ of both quadratures of the signal and idler.

⁹I substitute $\hat{x}(\Omega) = \frac{-\alpha}{\mu\Omega^2\sqrt{2}} (\hat{a}(\Omega) + \hat{a}^\dagger(-\Omega))$, found by Fourier transforming Eq. 4.2, in the equation for $\hat{a}(\Omega)$ before vectorising.

$$M_d = \begin{bmatrix} \gamma_{\text{tot}}^b & & & \\ & \gamma_{\text{tot}}^b & & \\ & & \gamma_{\text{tot}}^c & \\ & & & \gamma_{\text{tot}}^c \end{bmatrix} - i\Omega I + \chi \begin{bmatrix} 0 & & & ie^{i\phi} \\ & 0 & -ie^{-i\phi} & \\ & ie^{i\phi} & 0 & \\ -ie^{-i\phi} & & & 0 \end{bmatrix} + \omega_s^2 \begin{bmatrix} 1 & & & \\ & 1 & & \\ & & 0 & \\ & & & 0 \end{bmatrix} M_a^{-1} \begin{bmatrix} 1 & & & \\ & 1 & & \\ & & 0 & \\ & & & 0 \end{bmatrix}. \quad (4.5)$$

Here, I is the 4-by-4 identity matrix, all off-diagonal terms in each 4-by-4 matrix are zero unless otherwise shown, and the re-scaled coupling constants for the gravitational-wave signal and the radiation pressure¹⁰, respectively, are

$$\beta = \frac{\alpha L_{\text{arm}}}{\sqrt{2}\hbar} = \sqrt{\frac{P_{\text{circ}} L_{\text{arm}} \omega_0}{c\hbar}}, \quad \rho = \frac{\alpha^2}{\sqrt{2}\hbar\mu} = \frac{\sqrt{2}P_{\text{circ}}\omega_0}{c\mu L_{\text{arm}}}. \quad (4.6)$$

Using the input/output relation at the readout port like in Eq. 2.5, the beamsplitter model of detection loss (R_{PD}) in the output field ($\hat{B}_{\text{out}}, \hat{C}_{\text{out}}$), and $\Gamma = \frac{1}{\sqrt{2}} \begin{bmatrix} 1 & i \\ -i & 1 \\ & & 1 & i \\ & & -i & 1 \end{bmatrix}$ to convert to quadratures, I find the *signal and idler quadratures at the photodetector*¹¹ to be

$$\vec{\hat{X}}_{\text{PD}}(\Omega) = \sqrt{1 - R_{\text{PD}}} \vec{\hat{X}}_{\text{in}}(\Omega) + \sqrt{R_{\text{PD}}} \vec{\hat{X}}_{\text{PD}}^L(\Omega) - \sqrt{2(1 - R_{\text{PD}})} \Gamma \begin{bmatrix} \sqrt{\gamma_R^b} & & & \\ & \sqrt{\gamma_R^b} & & \\ & & \sqrt{\gamma_R^c} & \\ & & & \sqrt{\gamma_R^c} \end{bmatrix} \vec{d}(\Omega). \quad (4.7)$$

Substituting Eq. 4.3 into Eq. 4.7 and using Γ to convert the remaining vacuum inputs to quadratures, e.g. $\vec{\hat{n}}_a^L(\Omega)$ to $\Gamma^{-1} \vec{\hat{X}}_a^L(\Omega)$, I find the output quadratures at the photodetector in terms of the input quadratures and the gravitational-wave signal to be

$$\vec{\hat{X}}_{\text{PD}}(\Omega) = T \vec{h}(\Omega) + R_{\text{in}} \vec{\hat{X}}_{\text{in}}(\Omega) + R_a^L \vec{\hat{X}}_a^L(\Omega) + R_b^L \vec{\hat{X}}_b^L(\Omega) + R_{\text{PD}}^L \vec{\hat{X}}_{\text{PD}}^L(\Omega) \quad (4.8)$$

$$T = -\sqrt{1 - R_{\text{PD}}}\omega_s(-i\beta)\Gamma\sqrt{2} \begin{bmatrix} \sqrt{\gamma_R^b} & & & \\ & \sqrt{\gamma_R^b} & & \\ & & \sqrt{\gamma_R^c} & \\ & & & \sqrt{\gamma_R^c} \end{bmatrix} M_d^{-1} \begin{bmatrix} 1 & & & \\ & 1 & & \\ & & 0 & \\ & & & 0 \end{bmatrix} M_a^{-1} \begin{bmatrix} 1 & & & \\ & -1 & & \\ & & 0 & \\ & & & 0 \end{bmatrix} \quad (4.9)$$

¹⁰Here, $\rho = 0$, i.e. $\mu = M/4 \rightarrow \infty$, turns off the radiation pressure noise.

¹¹Here, $\vec{\hat{X}}(\Omega) = (\hat{X}_{b,1}(\Omega), \hat{X}_{b,2}(\Omega), \hat{X}_{c,1}(\Omega), \hat{X}_{c,2}(\Omega))^T$, as in Section 2.2.2.

$$\mathbf{R}_{\text{in}} = \sqrt{1 - R_{\text{PD}}}\Gamma \left(\mathbf{I} - 2 \begin{bmatrix} \sqrt{\gamma_R^b} & & & \\ & \sqrt{\gamma_R^b} & & \\ & & \sqrt{\gamma_R^c} & \\ & & & \sqrt{\gamma_R^c} \end{bmatrix} \mathbf{M}_d^{-1} \begin{bmatrix} \sqrt{\gamma_R^b} & & & \\ & \sqrt{\gamma_R^b} & & \\ & & \sqrt{\gamma_R^c} & \\ & & & \sqrt{\gamma_R^c} \end{bmatrix} \right) \Gamma^{-1} \quad (4.10)$$

$$\mathbf{R}_a^L = -\sqrt{1 - R_{\text{PD}}}\omega_s\Gamma 2\sqrt{\gamma_a} \begin{bmatrix} \sqrt{\gamma_R^b} & & & \\ & \sqrt{\gamma_R^b} & & \\ & & \sqrt{\gamma_R^c} & \\ & & & \sqrt{\gamma_R^c} \end{bmatrix} \mathbf{M}_d^{-1} \begin{bmatrix} 1 & & & \\ & 1 & & \\ & & 0 & \\ & & & 0 \end{bmatrix} \mathbf{M}_a^{-1} \begin{bmatrix} 1 & & & \\ & 1 & & \\ & & 0 & \\ & & & 0 \end{bmatrix} \Gamma^{-1} \quad (4.11)$$

$$\mathbf{R}_b^L = -\sqrt{1 - R_{\text{PD}}}\Gamma 2 \begin{bmatrix} \sqrt{\gamma_R^b} & & & \\ & \sqrt{\gamma_R^b} & & \\ & & \sqrt{\gamma_R^c} & \\ & & & \sqrt{\gamma_R^c} \end{bmatrix} \mathbf{M}_d^{-1} \begin{bmatrix} \sqrt{\gamma_R^b} & & & \\ & \sqrt{\gamma_R^b} & & \\ & & \sqrt{\gamma_R^c} & \\ & & & \sqrt{\gamma_R^c} \end{bmatrix} \Gamma^{-1} \quad (4.12)$$

$$\mathbf{R}_{\text{PD}}^L = \sqrt{R_{\text{PD}}}\mathbf{I}. \quad (4.13)$$

The *total quantum noise* is given by the spectral density matrix Eq. 2.8, which simplifies, assuming uncorrelated vacuum at each loss port, to

$$\mathbf{S}_X = \mathbf{R}_{\text{in}}\mathbf{R}_{\text{in}}^\dagger + \mathbf{R}_a^L\mathbf{R}_a^{L\dagger} + \mathbf{R}_b^L\mathbf{R}_b^{L\dagger} + \mathbf{R}_{\text{PD}}^L\mathbf{R}_{\text{PD}}^{L\dagger}. \quad (4.14)$$

The structure of \mathbf{S}_X is divided into 2-by-2 blocks of signal-signal, signal-idler, and idler-idler (co)variances as in Section 2.2.2 but now with terms for the radiation-pressure noise such that the variances and covariances no longer reduce to 1 and 0, respectively, when the squeezer is off. The pump phase only appears in the off-diagonal, signal-idler covariances. The *signal response* for a given quadrature is defined with respect to the signal $\tilde{h}(\Omega)$, not $\vec{h}(\Omega)$, and therefore the vector of the signal response for each signal and idler quadrature at the photodetector is

$$\mathbf{T} \begin{pmatrix} 1 \\ \frac{1}{0} \\ 0 \end{pmatrix} = \frac{2\beta\sqrt{1 - R_{\text{PD}}}\omega_s}{(\gamma_a - i\Omega)(\chi^2 - (\gamma_{\text{tot}}^b - i\Omega)(\gamma_{\text{tot}}^c - i\Omega)) - \omega_s^2(\gamma_{\text{tot}}^c - i\Omega)} \begin{pmatrix} 0 \\ -\sqrt{\gamma_R^b}(\gamma_{\text{tot}}^c - i\Omega) \\ \sqrt{\gamma_R^c}\chi\cos(\phi) \\ \sqrt{\gamma_R^c}\chi\sin(\phi) \end{pmatrix}. \quad (4.15)$$

Here, $\mathbf{T}\vec{h}(\Omega) = \mathbf{T} \begin{pmatrix} 1 \\ \frac{1}{0} \\ 0 \end{pmatrix} \tilde{h}(\Omega)$ gives the signal in each quadrature. Therefore, by Eq. 4.15, the gravitational-wave signal is in the second signal quadrature as well as each idler quadrature when the squeezer is on ($\chi \neq 0$). For simplicity and to compare to Ref. [1],

signal-recycling cavity length, L_{SRC}	1.124 km	signal mode transmissivity, $T_{\text{SRM},b}$	0.046
input test mass transmissivity, T_{ITM}	0.197	signal readout rate, γ_R^b	500 Hz
sloshing frequency, ω_s	5 kHz	idler mode transmissivity, $T_{\text{SRM},c}$	0
idler mode intra-cavity loss, $T_{l,c}$	1000 ppm	idler readout rate, γ_R^c	0 Hz

Table 4.1: Nondegenerate internal squeezing signal readout parameter set is based on LIGO Voyager [54] and the same as Table 3.1 but with the deviations shown to make the sensitivity more sharply peaked (γ_R^b is now 0.5 kHz compared to 5 kHz) and the addition of the idler mode. Radiation pressure is included using $\rho \neq 0$ from Eq. 4.6 unless $\rho = 0$ is stated. The results shown use these parameters unless stated otherwise.

I will consider measuring the second signal quadrature, henceforth referred to as “signal readout”. However, this is not necessarily the optimum readout of the signal quadratures since the noise might be sufficiently lower in the first quadrature to preference measuring some quadrature between the two. I will consider this and alternative readout schemes involving the idler in Chapter 6.

The quantum noise and signal responses of the signal readout scheme are, respectively, $\sqrt{(S_X)_{2,2}}$ and $\left| \left(\text{T} \begin{pmatrix} 1 \\ 0 \\ 0 \end{pmatrix} \right)_2 \right|$, and the *sensitivity*, conventionally plotted as the noise-to-signal ratio, is

$$\sqrt{S_h} = \frac{\sqrt{(S_X)_{2,2}}}{\left| \left(\text{T} \begin{pmatrix} 1 \\ 0 \\ 0 \end{pmatrix} \right)_2 \right|}. \quad (4.16)$$

To partially validate this result, I have repeated its derivation using 2-by-2 matrices¹², and will compare it to the known limits below.

4.3 Results

I now examine some of the immediate results of the model: (1) the lossless behaviour of the system, (2) the general behaviour when losses are introduced, and (3) the high arm loss limit. Throughout the rest of this thesis, I will use the parameter set in Table 4.1. The choice of parameter set can bias the analysis of a configuration, and I mention, where relevant, the effects of varying the parameters (e.g. the readout rates which have a large variation in the literature [1, 8, 23]). These parameters have not been optimised for the sensitivity which I leave to future work.

¹²Which is not a physically meaningful difference, and therefore I will not present it here, but it separates the signal and idler such that the derivations are not identical.

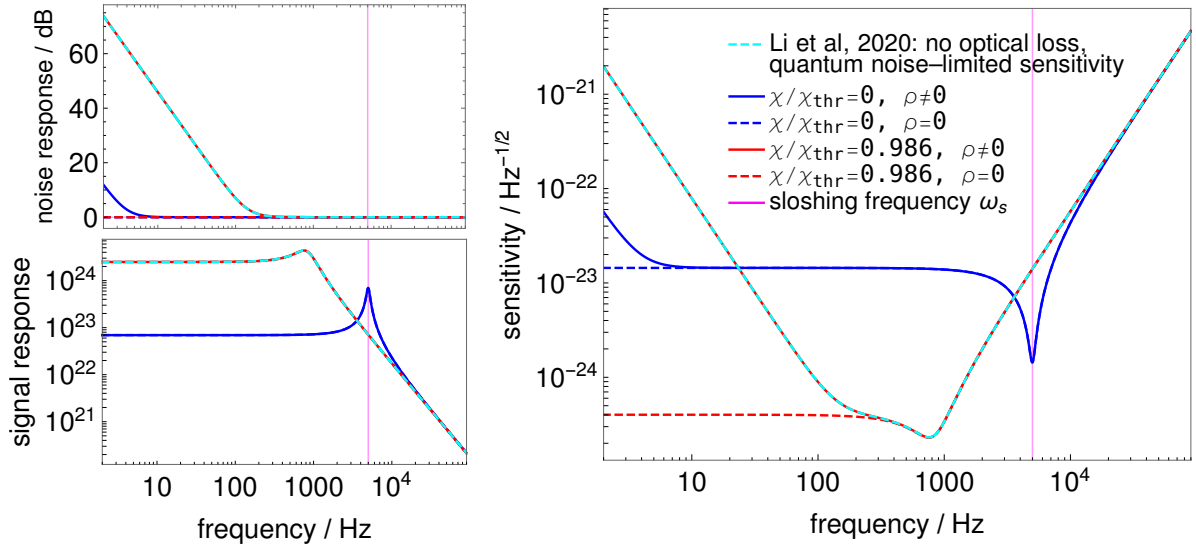


Figure 4.3: Nondegenerate internal squeezing in the lossless limit, showing the quantum noise (upper-left panel), signal response (bottom-left panel), and sensitivity (right panel) with squeezing (red curves) and without squeezing (blue curves). I also show the results with ($\rho \neq 0$, see Eq. 4.6) and without ($\rho = 0$) radiation pressure noise, and I compare them to the lossless optomechanical analogue from Section 3.2 (cyan curve) with the same ratio to threshold. I use the data from Fig. 5 in Ref. [1] with permission from the authors [63]. The noise and signal responses and sensitivity reduce to the expected lossless limit. I use the parameters in Table 4.1 but with no losses.

To partially validate the model, I check that it reduces to the expected *lossless limit* in Fig. 4.3. In the lossless limit, where $\gamma_a = \gamma_b = \gamma_c = R_{\text{PD}} = 0$, the equations-of-motion of nondegenerate internal squeezing in Eq. 4.2 reduce to those of the lossless optomechanical analogue in Ref. [1]¹³. The resulting noise and signal responses and sensitivity also reduce to this limit as shown in Fig. 4.3. This limit is expected from the comparison of the mode structure of the two lossless systems discussed in Section 4.1.

The *general behaviour of nondegenerate internal squeezing without losses* is shown in Fig. 4.3. With the squeezer off, the sensitivity curve is shaped by the radiation-pressure noise below 10 Hz and the signal response resonance at the sloshing frequency 5 kHz with bandwidth 500 Hz determined by the signal readout rate γ_R^b , as discussed in Section 3.1.1. With the squeezer on, lossless nondegenerate internal squeezing (1) amplifies the radiation-pressure noise to dominate below 100 Hz and further amplifies it with increased squeezer parameter and (2) amplifies the signal response from DC up to the peak frequency. The peak frequency without squeezing is at the sloshing frequency but de-

¹³Compare \hat{H}_I from Eq. 3.2 to Eq. 4.1 with the semi-classical approximation to the pump mode \hat{u} .

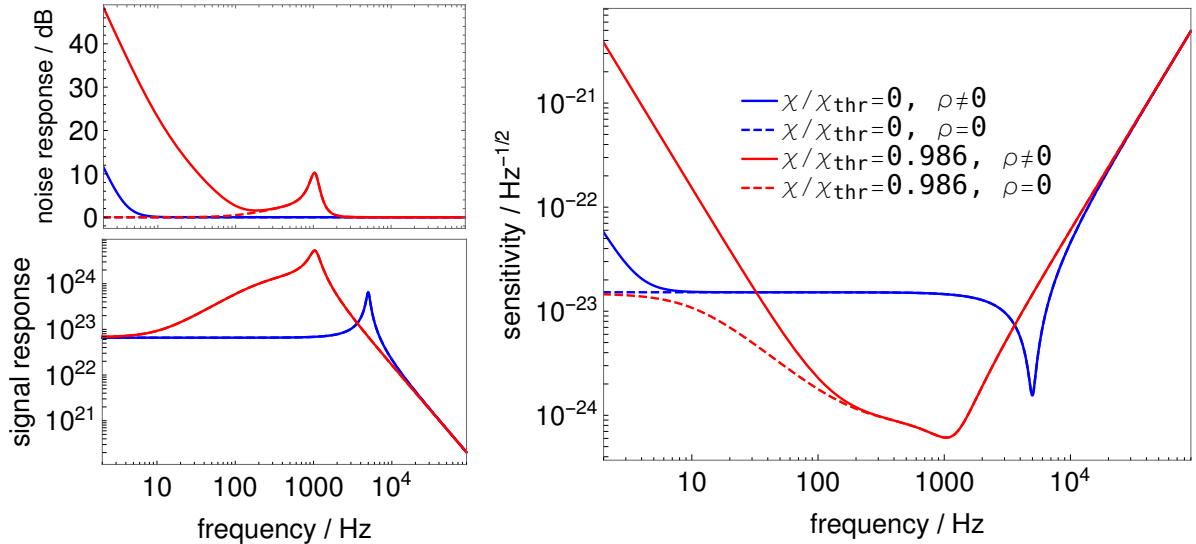


Figure 4.4: Nondegenerate internal squeezing with all the optical losses included, showing the noise (upper-left panel), signal (bottom-left panel), and sensitivity (right panel). The effect of the squeezer and the radiation pressure noise (turned off by setting $\rho = 0$) on the sensitivity are shown; the squeezer anti-squeezes the noise around the peak frequency of the signal response. The losses change the slope of the radiation pressure noise around 10 Hz and also cause the signal to not be amplified down to DC compared to the lossless case in Fig. 4.3. The squeezer parameter is normalised to the lossy threshold which will be found later. I use the parameters in Table 4.1.

creases with increased squeezer parameter which is related to the squeezing threshold and will be discussed later. The signal response is amplified by the white-light cavity effect similarly to the optomechanical analogue in Section 3.2. The changes are not localised to the sloshing frequency, e.g. the radiation-pressure noise is anti-squeezed, unlike degenerate internal squeezing, because coupling to the idler mode changes the response of the detector.

The *general lossy behaviour* of nondegenerate internal squeezing is shown in Fig. 4.4. The behaviour with losses is the same as the lossless case in Fig. 4.3 except that (1) the shot noise is anti-squeezed around the peak frequency, (2) the radiation-pressure noise is anti-squeezed less, and (3) the signal amplification drops off below 100 Hz and converges to the response without squeezing below 10 Hz. The bandwidth of the signal amplification is determined by the losses and therefore does not extend to DC with losses present. The peak frequency around which the signal and shot noise are amplified is determined by the squeezer parameter, sloshing frequency, and loss rates. Like the signal, the shot noise is also anti-squeezed around the peak frequency because the internal squeezer affects both

the signal and noise. Inspecting the limit of smaller and smaller losses confirms that the shot noise peak decreases until it vanishes in the lossless limit as expected by analogy to the optomechanical configuration [1]. Overall, the squeezer now improves sensitivity from around 40–3000 Hz and worsens it outside that band except above 10 kHz where the sensitivity is the same without squeezing. This is largely the same behaviour as the lossless case, but I will more closely examine the effects of each loss in the next chapter. These quoted frequencies are specific to this parameter set but the general performance is the same: nondegenerate internal squeezing improves sensitivity at some broad range of “middle” frequencies at the cost of “low” frequency sensitivity.

The *effect of each configuration parameter* is similar to the effect on the interferometer without squeezing discussed in Sections 1.2 and 3.1.1. To summarise, increasing the circulating power in the arms increases the signal response at all frequencies via β in Eq. 4.15. Increasing the arm length increases the same factor β as the power but also decreases the bandwidth of the signal response and the sloshing frequency which determines the peak. The sloshing frequency also decreases with decreased input test mass transmission and longer signal-recycling cavities. Increasing the signal-recycling length decreases the bandwidth of the signal peak ¹⁴, which is also decreased by decreased signal-recycling mirror transmission. The radiation-pressure noise increases with lighter test masses and increased pump power. Finally, increased pump power also increases the peak shot noise and signal amplification, and the pump phase does not affect signal readout.

To further validate the model, I check that it reduces to the expected limit when the arm loss is taken to infinity. In the *high arm loss limit*, $\gamma_a \rightarrow \infty$, the equations-of-motion of nondegenerate internal squeezing in Eq. 4.2 reduce to those in Eq. 2.12 for a nondegenerate OPO between the signal-recycling mirror and a fully-reflective input test mass. I have verified this limit by checking that each of the terms of the shot noise matrix $S_X|_{\rho=0}$ from Eq. 4.14 reduces to the OPO value [49] ¹⁵. Although I expected physically that the input test mass would instead become another loss port with its original transmissivity, this behaviour can be explained as in the limit the equation-

¹⁴The arm cavity bandwidth gives the overall shape of the signal response but the signal-recycling cavity bandwidth gives the width of the peak at the sloshing frequency.

¹⁵Moreover, I have checked that a similar limit holds for the model of degenerate internal squeezing in Section 3.1 that reduces to a degenerate OPO with the input test mass fully reflective.

of-motion for the fluctuating component becomes $\dot{\delta\hat{a}} \approx -\gamma_a\delta\hat{a}$ which quickly decays, and, therefore, any vacuum fluctuations $\delta\hat{n}_a^L$ cannot couple to $\delta\hat{b}$. However, I suspect that this is a false consequence of the single-mode approximation and that if a “transfer matrix” approach (e.g. in Refs. [23, 64])¹⁶ was instead used then the limit would instead be a degenerate OPO with added intra-cavity loss to account for the open input test mass port; I leave verifying this to future work. Therefore, this model predicts that lossy nondegenerate internal squeezing behaves somewhere between the lossless optomechanical analogue and the nondegenerate OPO but closer to the former since the realistic arm loss for future detectors is below this high loss regime (e.g. 100 ppm versus above 10000 ppm) and thus the exact behaviour in this regime is not of concern.

Even further validation of this analytic model could be performed by comparing it to a numerical model, which I leave to future work.

4.4 Stability and threshold

I now determine when nondegenerate internal squeezing is stable and below threshold.

4.4.1 Stability

Stability is a feature of nondegenerate internal squeezing that might not be fully inherited from its limiting configurations. I use the same method to determine stability as degenerate internal squeezing in Appendix A. The signal and noise responses are fractions of polynomials of Ω, χ with denominators¹⁷ given by $q(\Omega, \chi)$ and $\Omega^4 q(\Omega, \chi) q(\Omega, -\chi)$, respectively. Here, q only depends on χ^2 and so the noise response denominator is $\Omega^4 q(\Omega, \chi)^2$,

¹⁶Where the fields at a point are propagated inside the cavities and the cavity modes, e.g. \hat{a} , are not explicit. Not to be confused with the transfer matrices describing the signal T and noise R responses. The Hamiltonian method is more comprehensive than this approach and could also be modified to use the fields at a point rather than the cavity modes [38].

¹⁷I state these for the modulus-squared responses, i.e. $(S_X)_{2,2}$ from Eq. 4.14 and $\left| \left(T \begin{pmatrix} 1 \\ \frac{1}{0} \end{pmatrix} \right) \right|_2^2$ from Eq. 4.15, but the poles, i.e. zeros of q , do not change under the square root.

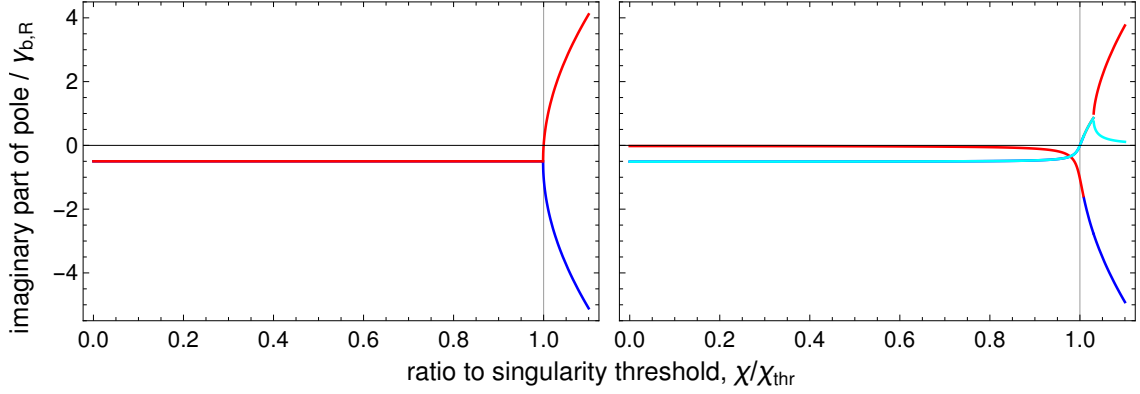


Figure 4.5: Stability of nondegenerate internal squeezing, for lossless (left panel) and lossy (right panel) cases. I show the imaginary part of the shared poles of the noise and signal responses versus the squeezer parameter; where the imaginary part becomes positive, the system becomes unstable. The different colours indicate different poles (zeros of q) found numerically, and any discontinuities are numerical or plotting artefacts. I will define the singularity threshold (χ_{thr}) such that the system is stable below threshold; the value of χ_{thr} is different between the two cases. I use the parameters in Table 4.1.

where q is some polynomial in Ω, χ ,

$$q(\Omega, \chi) = (\gamma_a^2 + \Omega^2) \left(\Omega^2 (\gamma_{\text{tot}}^b{}^2 + \gamma_{\text{tot}}^c{}^2 + 2\chi^2) + (\gamma_{\text{tot}}^b \gamma_{\text{tot}}^c - \chi^2)^2 + \Omega^4 \right) \quad (4.17)$$

$$- 2\omega_s^2 (\gamma_a \gamma_{\text{tot}}^c \chi^2 - \gamma_a \gamma_{\text{tot}}^b (\gamma_{\text{tot}}^c{}^2 + \Omega^2) + \Omega^2 (\gamma_{\text{tot}}^c{}^2 + \chi^2 + \Omega^2)) + \omega_s^4 (\gamma_{\text{tot}}^c{}^2 + \Omega^2).$$

This means that the poles of the responses are the shared zeros of q ¹⁸, except for the radiation-pressure noise singularity at $\Omega = 0$ which I ignore because it comes from the horizontally free-falling mass assumption and physically the resonance of the test mass is finite. Therefore, nondegenerate internal squeezing is unstable if any of the complex Ω zeros of q have a positive imaginary part and is marginally stable if any of them have no imaginary part [65]. As shown in Fig. 4.5, the *lossless system is stable below threshold* ($\chi \leq \chi_{\text{thr}} = \omega_s$) which agrees with Ref. [1]. The lossy system is also stable up to a point that I will shortly define to be the threshold. Since Eq. 4.17 only depends on the pump power, readout and loss rates, and sloshing frequency, therefore, other factors, such as radiation pressure or pump phase, do not affect the stability.

¹⁸The second factor of q in the noise response cancels with a term in the numerator meaning that the multiplicity is the same.

4.4.2 Singularity threshold

As discussed in Sections 2.2.1, 2.2.2, and 3.1.1, the threshold of a squeezing system is the boundary where gains balance losses and the no-pump-depletion assumption breaks. Beyond threshold the system begins lasing as the cavity field is (finitely) coherently amplified [48] and energy is taken from the pump mode. Finding the threshold of nondegenerate internal squeezing is required to understand where my model is valid because I assume no pump depletion and, experimentally, how high the pump power can be raised without lasing. The threshold of lossy degenerate and nondegenerate internal squeezing has not been discussed in the literature to date, and, in this section, I present my method for determining threshold in these models. Since I assume no pump depletion, beyond threshold, the net gain at the squeezer instead leads to unbounded, coherent amplification of the cavity mode [39], and therefore *the system becomes unstable*. Therefore, my method is to define threshold as the point of marginal stability of the system with no pump depletion and assume that whenever the system becomes unstable it is because of the squeezer reaching threshold.

To explain *how I first devised this method*, which was separate from considering stability, since lossless degenerate internal squeezing on threshold has a minimum squeezed quadrature of zero, I initially tried to maximise the anti-squeezed quadrature of lossy nondegenerate internal squeezing against (Ω, χ) . But doing so numerically encountered division-by-zero errors which lead me to examine the noise response and find the singularities, i.e. the real zeros of q , analytically. Then, I connected that the OPOs have singularities at $\Omega = 0$ in the anti-squeezed quadrature on threshold and that a pole on the real Ω axis corresponds to marginal stability.

Formally, my method is to define the “*singularity threshold*”¹⁹ as the smallest non-negative²⁰ value of the squeezing parameter such that the anti-squeezed quadrature of the quantum noise has a singularity at some (real) frequency. In particular, I look for points where the anti-squeezed quadrature, i.e. any of the diagonal terms of S_X , diverges to infinity in $(\Omega, \chi) \subset \mathbb{R}^2$ space²¹. I define threshold with respect to anti-squeezing

¹⁹Which might be better called the “stability threshold”.

²⁰Because pump phase is included explicitly in the models, the squeezer parameter is non-negative.

²¹To reduce confusion, I do not call these points poles since, unlike when considering stability, I am restricting Ω to be real and so the noise response is not defined on \mathbb{C} .

because the singularities of the anti-squeezed quadrature are robust to losses, unlike the zeros of the squeezed quadrature, as shown in Fig. 2.5. To validate this method, I find the (real) singularities²² of the noise response (squared), i.e. the zeros of the denominator of S_X , for the other configurations in this thesis with known threshold values, and for nondegenerate internal squeezing, to be

$$\text{degenerate OPO : } \Omega_{\text{thr}} = 0, \chi_{\text{thr}} = \gamma_{\text{tot}}^b \quad (4.18)$$

$$\text{nondegenerate OPO : } \Omega_{\text{thr}} = 0, \chi_{\text{thr}} = \sqrt{\gamma_{\text{tot}}^b \gamma_{\text{tot}}^c} \quad (4.19)$$

$$\text{degenerate internal squeezing : } \begin{cases} \Omega_1 = 0, \chi_1 = \gamma_{\text{tot}}^b + \frac{\omega_s^2}{\gamma_a}; & \gamma_a \neq 0 \\ \Omega_2 = \sqrt{\omega_s^2 - \gamma_a^2}, \chi_2 = \gamma_{\text{tot}}^b + \gamma_a; & \omega_s \geq \gamma_a \geq 0 \end{cases} \quad (4.20)$$

nondegenerate internal squeezing :

$$\begin{cases} \Omega_1 = 0, \chi_1 = \sqrt{\gamma_{\text{tot}}^c (\gamma_{\text{tot}}^b + \frac{\omega_s^2}{\gamma_a})}; & \gamma_{\text{tot}}^c \neq 0, \gamma_a \neq 0 \\ \Omega_2 = \sqrt{\frac{\gamma_{\text{tot}}^c \omega_s^2 - \gamma_a (\omega_s^2 + \gamma_a (\gamma_{\text{tot}}^b + \gamma_{\text{tot}}^c))}{\gamma_{\text{tot}}^b + \gamma_{\text{tot}}^c}}, \chi_2 = \sqrt{(\gamma_a + \gamma_{\text{tot}}^b)(\gamma_a + \gamma_{\text{tot}}^c + \frac{\omega_s^2}{\gamma_{\text{tot}}^b + \gamma_{\text{tot}}^c})}; & \gamma_{\text{tot}}^c \neq 0, (*) \end{cases} \quad (4.21)$$

$$(*) : \gamma_{\text{tot}}^c \omega_s^2 \geq \gamma_a (\omega_s^2 + \gamma_a (\gamma_{\text{tot}}^b + \gamma_{\text{tot}}^c))$$

I have *verified* these values by plotting the noise response and observing the singularity, e.g. as shown in Fig. 4.6. For squeezer parameter near threshold, e.g. $\chi = 0.95\chi_{\text{thr}}$ in Fig. 4.4, the peak frequency around which the shot noise and signal are amplified is determined by the threshold frequency²³. When multiple singularities are listed above, the singularity threshold is determined by the smallest χ value:

$$\chi_{\text{thr}} = \min_{i \in \{1,2\}} (\chi_i), \quad \Omega_{\text{thr}} = \Omega_{\text{argmin}(\chi_i)}. \quad (4.22)$$

Which singularity has the smallest squeezer parameter changes as the losses change, and where it changes, the singularities merge by inspection²⁴. The smallest squeezer

²²The reality condition is used to simplify the zeros of q , as in the solution for χ_{thr} there is an imaginary component that, when set to zero, gives the real Ω solution.

²³Consider this peak as a slice with constant χ of the region around the singularity in (real) (Ω, χ) space.

²⁴Therefore, the singularity threshold is continuous for these configurations.

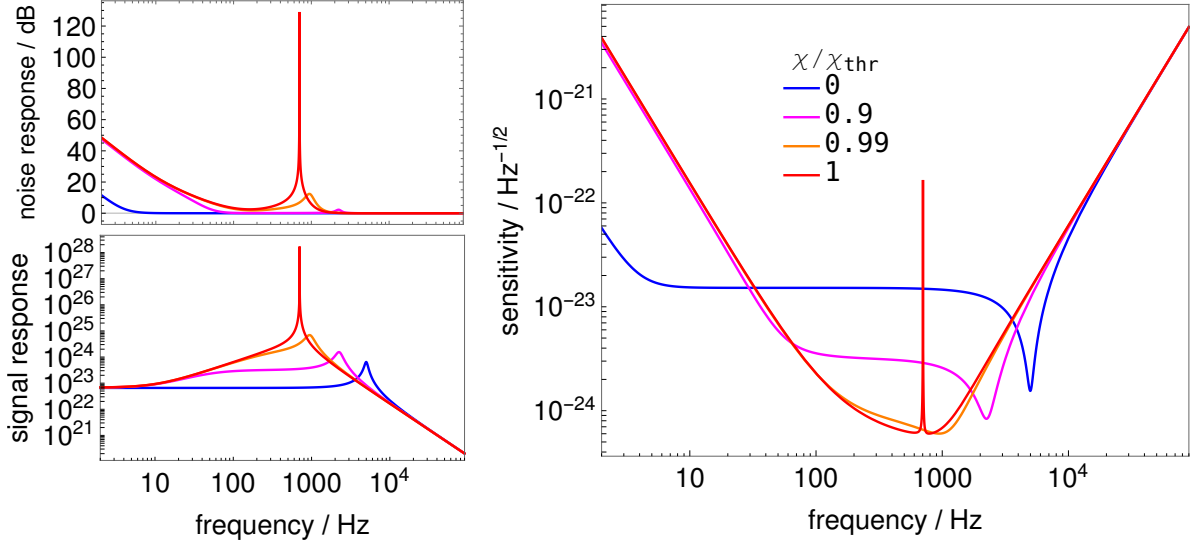


Figure 4.6: Nondegenerate internal squeezing noise (upper-left panel), signal (bottom-left panel), and sensitivity (right panel) when approaching and at threshold. At threshold, the no-pump-depletion assumption breaks and the responses are singular. A false peak appears in the sensitivity at the threshold frequency because of numerical error – the sensitivity should be finite and near the 99% threshold curve because the shared noise and signal singularities cancel analytically. I use the parameters in Table 4.1.

parameter gives the first singularity encountered (at any frequency) when increasing the pump power from zero. The singularity threshold is not affected by radiation pressure or pump phase since they do not affect the zeros of the denominator q of the noise response, as explained in Section 4.4.1. Physically, the radiation-pressure noise does not affect the gain-loss balance and the pump phase only affects where the anti-squeezed quadrature lies in the quadrature basis.

The singularity threshold in Eq. 4.18 recovers the known threshold values for the OPOs from Sections 2.2.1 and 2.2.2. Although it also recovers the threshold for degenerate internal squeezing from Section 3.1.1, it does not necessarily find the minimum of the squeezed quadrature, which I discuss in Appendix C. For *nondegenerate internal squeezing*, as shown in Fig. 4.7, in the lossless limit $\gamma_a = 0, \gamma_c \rightarrow 0$ the singularities approach $(0, \infty)$ and $(0, \omega_s)$ which recovers the exceptional value $\chi_m = \omega_s$ of the coupling rates of the optomechanical analogue from Section 3.2. In that configuration, the threshold can be defined by the same principle of gains and losses applied to the signal and mechanical idler modes driven by the blue-detuned pump laser. Moreover, the marginal stability of the optomechanical system at $\chi_m = \omega_s$ means that a pole in the complex Ω plane has

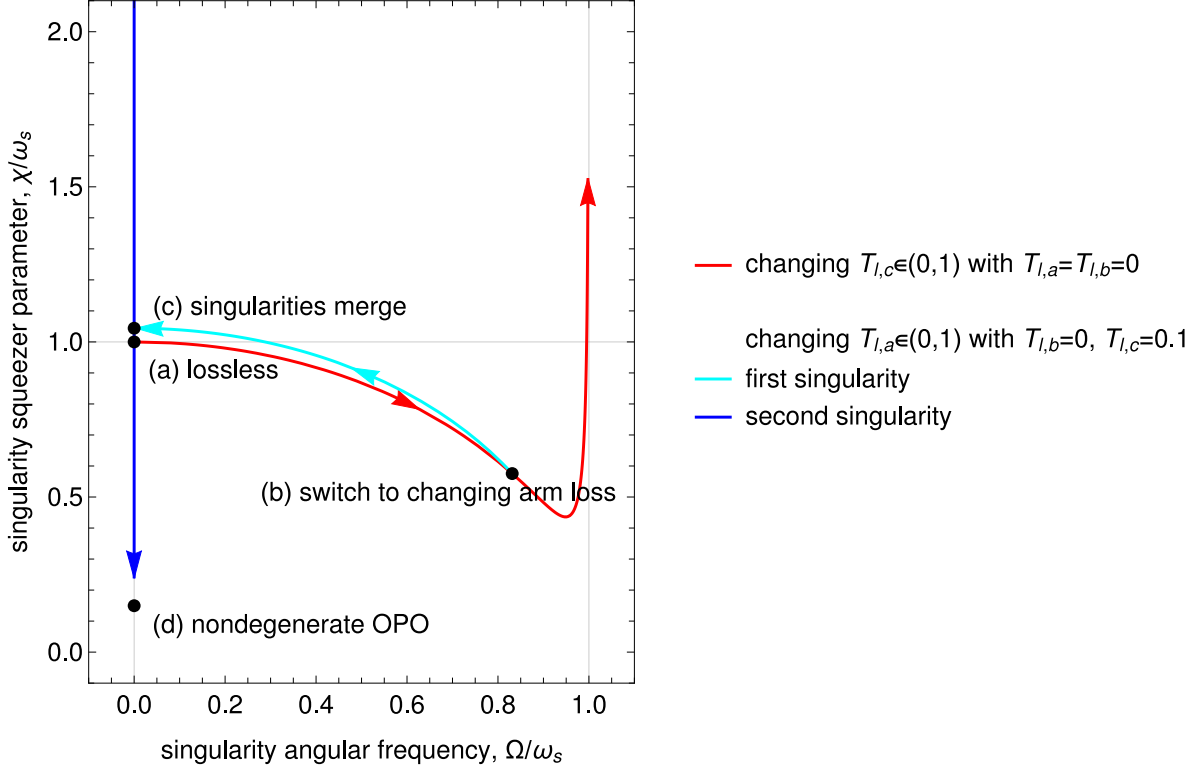


Figure 4.7: Nondegenerate internal squeezing trajectories of singularities of the anti-squeezed noise in (real) (Ω, χ) space as losses are changed. Two effects are shown: (1) the idler loss is changed and the arm loss is zero along the red curve and (2) the idler loss is fixed and the arm loss is changed along the cyan and blue curves. In the former case, the second singularity is at $(0, \infty)$. The path from the lossless case to the high arm loss limit goes from point (a) with no loss to point (b) with idler loss $T_{l,c} = 0.1$ along the red curve, then changes arm loss to point (c) with $T_{l,a} \approx 0.3$, $T_{l,c} = 0.1$ along the cyan curve, and, finally, to point (d) with $T_{l,a} = 1$, $T_{l,c} = 0.1$ along the blue curve. The blue curve does not reach point (d) because of limited numerical sampling. I use large idler loss ($T_{l,c} = 0.1$) to show the trajectories more clearly, but if it is realistic (e.g. $T_{l,c} = 1000\text{ppm}$), then (b) and (c) move closer to (a). I use the parameters in Table 4.1 with zero signal loss ($T_{l,b}$).

moved on to the real axis and therefore is a (real) singularity. As shown in Fig. 4.7, as the idler loss γ_c is increased from zero with arm loss $\gamma_a = 0$, one singularity remains at $(0, \infty)$ and the other converges to $(\omega_s, \sqrt{\gamma_{\text{tot}}^b \gamma_c})$ when $\gamma_c \rightarrow \infty$. Fixing the idler loss at $T_{l,c} = 0.1$ and changing the arm loss γ_a ²⁵, the singularities merge at the $\Omega = 0$ axis when $\gamma_{\text{tot}}^c \omega_s^2 = \gamma_a \omega_s^2 + \mathcal{O}(\gamma_a^2)$ which, assuming that γ_a is small compared to ω_s ²⁶, is when

²⁵Threshold remains poorly defined when the idler loss is zero like the nondegenerate OPO in Section 2.2.2. The lossless limit requires $\gamma_{\text{tot}}^c \rightarrow 0$ to be taken formally.

²⁶Which is reasonable for a gravitational-wave detector with 4 km arms and realistic $T_{l,a} = 100\text{ppm}$ since γ_a and ω_s are 1 Hz and 5 kHz respectively.

$\gamma_c \approx \gamma_a$. In the high arm loss limit $\gamma_a \gg \gamma_c$, the remaining singularity converges to the nondegenerate OPO threshold $(\Omega, \chi) \xrightarrow{\gamma_a \rightarrow \infty} (0, \sqrt{\gamma_{\text{tot}}^b \gamma_c})$, as expected.

Although there is more to understand about singularity threshold, *I will use the ratio to singularity threshold*, henceforth, to normalise the squeezer parameter between different losses and guarantee that the system is stable. For future work, pump depletion could be included in the model to verify threshold by calculating when the coherent amplitude of the output field is non-zero ²⁷. This would also provide a clearer physical explanation by directly finding the gain-loss balance instead of inferring it from instability under the no-pump-depletion assumption.

4.5 Chapter summary

In this chapter, I have derived and characterised a Hamiltonian model of nondegenerate internal squeezing from the perspective of general quantum metrology. After motivating the configuration, I derived its sensitivity, partially validating my model by showing that it reduced to the expected high and low loss limits. Finally, I presented my method to find the threshold of nondegenerate internal squeezing by finding where the system is stable.

²⁷The coherent amplitudes were discarded in the Hamiltonian model when fluctuating components $\delta\hat{Q}(t)$ were taken.

Nondegenerate internal squeezing for gravitational-wave detection

In this chapter, I now apply my model to consider the potential use of nondegenerate internal squeezing in a future gravitational-wave detector. This is exploratory work and I do not determine the optimal configuration for a future detector, instead, I focus on the general feasibility of nondegenerate internal squeezing. Firstly, in Section 5.1, I examine the tolerance of nondegenerate internal squeezing to the realistic optical losses in a future detector and compare it to degenerate internal squeezing. Secondly, in Section 5.2, I discuss whether nondegenerate internal squeezing is a viable, all-optical alternative to stable optomechanical filtering. Finally, in Section 5.3, I determine if nondegenerate internal squeezing might feasibly improve kilohertz sensitivity and also consider applying it to improve broadband sensitivity.

5.1 Tolerance to optical loss

Using my model from the previous chapter and the parameter set in Table 4.1., I compare how the sensitivity of nondegenerate internal squeezing degrades with each of the optical losses. I examine the loss tolerance of the configuration to detection, signal, idler, and arm losses in turn by comparing the change in sensitivity when the losses are higher or lower than their realistic values in Table 4.1 ¹.

Firstly, as shown in Fig. 5.1, the realistic *detection loss* of 10% from Table 4.1 has only a

¹Although I also compare each loss to the sensitivity without squeezing and with realistic loss, technically each of the curves should only be compared to the sensitivity with the same loss but without squeezing.

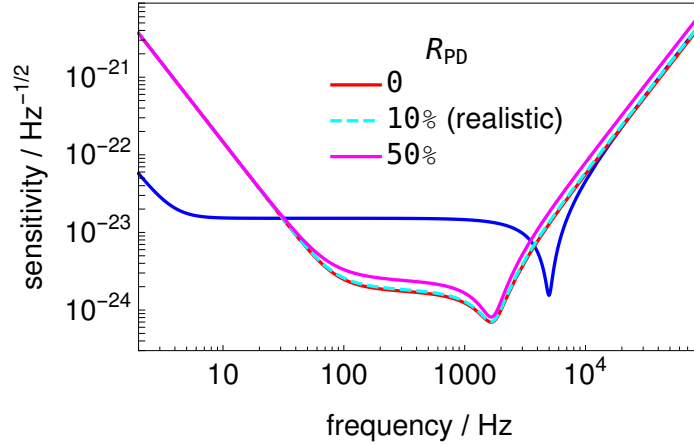


Figure 5.1: Nondegenerate internal squeezing tolerance to detection loss (R_{PD}). The blue curve shows the sensitivity without squeezing to show how much the sensitivity improvement degrades with loss; the other curves are for 95% threshold. The loss uniformly scales the signal to zero and the noise to the vacuum value. The system is more resilient around the anti-squeezed peak and where radiation-pressure noise dominates because the noise is far from the vacuum and decreases approximately the same amount as the signal. This is an advantage over degenerate internal squeezing, see Section 3.1.2. The tolerance is independent of the signal readout rate (γ_R^b). I use the parameter set in Table 4.1.

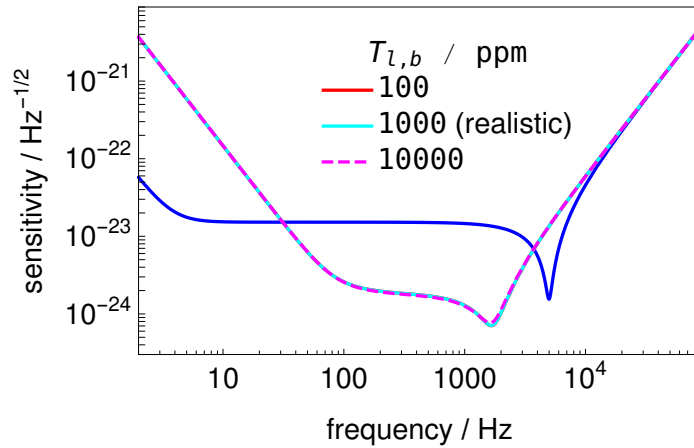


Figure 5.2: Nondegenerate internal squeezing tolerance to signal mode intra-cavity loss ($T_{l,b}$). The blue curve shows the sensitivity without squeezing; the other curves are for 95% threshold. The system is highly resilient to realistic levels of this loss (the cyan 1000 ppm curve is on top of the red 100 ppm curve which cannot be seen), e.g. even unrealistically high 10% loss (not shown) causes less than a factor of two decrease in the peak sensitivity. I show this plot for later comparison in the next chapter. The tolerance to realistic loss is the same at different readout rates. I use the parameter set in Table 4.1.

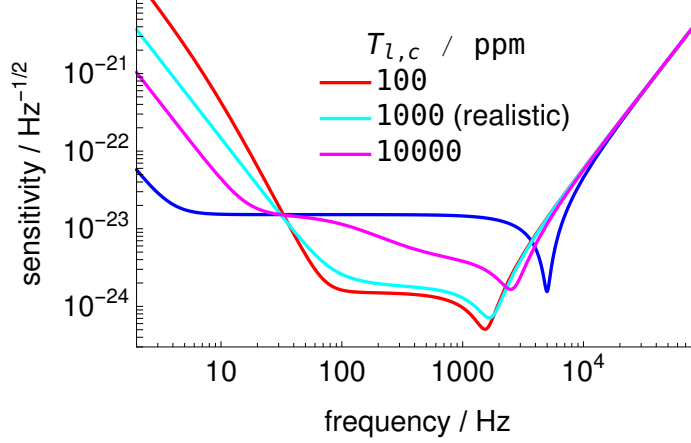


Figure 5.3: Nondegenerate internal squeezing tolerance to idler mode intra-cavity loss ($T_{l,c}$). The blue curve shows the sensitivity without squeezing; the other curves are for 95% threshold. The loss decreases the peak sensitivity and sensitivity from 100-1000 Hz but improves the radiation-pressure noise. The system is less tolerant to realistic levels of idler loss, e.g. 1000 ppm, than the other losses. If the signal readout rate is increased, then this tolerance worsens until at 50 kHz readout rate where the squeezer no longer improves sensitivity. The peak frequency changes with the loss because the threshold frequency changes. I use the parameter set in Table 4.1.

small effect on the sensitivity, at most a 10% decrease, and the tolerance is better around the peak ² and below 100 Hz. Detection loss scales down the signal response and pulls the noise response towards the vacuum level. At the peak, and where radiation pressure noise dominates, the noise is far enough above the vacuum level that the reduction in noise and signal are roughly the same and the sensitivity does not worsen. Away from the peak, the tolerance to detection loss diminishes as the noise is closer to vacuum but the tolerance is never worse than the tolerance of the detector without squeezing.

Secondly, as shown in Fig. 5.2, *signal mode intra-cavity loss* at the realistic level has a negligible effect on nondegenerate internal squeezing. This is because the signal mode is dominated by loss through the readout port at $T_{\text{SRM}} = 0.046 = 46000$ ppm compared to $T_{l,b} = 1000$ ppm ³.

Thirdly, as shown in Fig. 5.3, *idler intra-cavity loss* at the realistic level significantly degrades sensitivity (e.g. by a factor of 1.6 at 100 Hz). For signal readout, opening the

²The peak sensitivity is the lowest value of the noise-to-signal ratio shown.

³The tolerance is the same at higher readout rates because I change the readout rate by fixing the transmissivity of the signal-recycling mirror and changing the cavity length.

idler readout port further increases the effective idler loss ⁴, and, therefore, the idler readout port should be closed for signal readout. Increasing the idler loss also decreases the radiation-pressure noise. With the idler readout port closed, the decrease in sensitivity from 100–1000 Hz by introducing 1000 ppm of realistic idler loss is comparable to introducing an unrealistic amount of detection loss ($\sim 50\%$). The sensitivity is decreased more as the length of the cavity decreases (e.g. at higher readout rates) because all of the signal and idler loss rates increase.

Finally, realistic *arm intra-cavity loss* has a negligible effect on the sensitivity if the circulating power is fixed. Even increasing the arm loss a hundredfold only affects the sensitivity by less than a factor of two. Moreover, unlike the rest of the realistic future losses in Table 4.1, the arm loss is achievable today and therefore a high loss regime is irrelevant [22, 55].

Therefore, the *dominant realistic loss is idler loss* even when the idler readout port is closed, the detection loss has a smaller effect, and the signal and arm intra-cavity losses are negligible. However, the dominant noise above 100 Hz is the shot noise from the readout port because of the relative sizes of the readout rate $T_{\text{SRM}} = 46000$ ppm compared to the realistic loss rates, e.g. 1000 ppm ⁵. This agrees with the optomechanical analogue being limited by mechanical idler loss, see Section 3.2.1.

5.1.1 Comparison to degenerate internal squeezing

The tolerance to optical loss is different between nondegenerate and degenerate internal squeezing, in particular, the nondegenerate case is more resilient to some losses. For example, compare the effect of increasing the detection loss from 10% to 50% between Fig. 3.3 and Fig. 5.1 ⁶. Or, the effect of increasing the signal loss from 1000 ppm to 10000 ppm between Fig. 3.3 and Fig. 5.2. This is because of the general loss tolerance of squeezing versus anti-squeezing, as discussed before, squeezed noise is below the vacuum

⁴For example, a readout port symmetric between signal and idler increases the effective idler loss to a transmissivity of 46000 ppm in Fig. 5.3.

⁵Here, the detection loss $R_{\text{PD}} = 0.1$ should instead be compared to $1 - R_{\text{PD}} = 0.9$ due to the vacuum reflected off the readout port also contributing.

⁶Although these results use the same realistic losses, degenerate internal squeezing uses 5 kHz readout rate and nondegenerate internal squeezing uses 0.5 kHz. However, I have checked that my conclusions here hold when using the same parameters and, in particular, the tolerance of each configuration to detection loss is independent of the readout rate.

value and increases with losses but anti-squeezed noise is above the vacuum value and decreases. However, the arm loss is negligible in both cases and the nondegenerate case has worse tolerance to idler loss than any of the degenerate case's tolerances by comparing Fig. 5.3 and Fig. 3.3. Therefore, the nondegenerate case is not universally more loss tolerant. Moreover, the sensitivity curves are not directly comparable and for different metrics, the degenerate case might be more suitable, e.g. the nondegenerate case worsens the 10–50 Hz sensitivity which the degenerate case does not affect. I conclude that the overall tolerance to losses of nondegenerate internal squeezing is at least comparable to degenerate internal squeezing and that, in particular, it is more resistant to realistic detection losses.

5.1.2 Optimal squeezing

The optimal amount of squeezing for the maximum sensitivity at a given frequency is not necessarily on threshold ⁷. As shown in Fig. 5.4, the sensitivity at a given frequency ⁸, here 2.5 kHz, peaks at a point before threshold beyond which the amount that the signal is amplified more than the noise decreases. This is because the peak frequency of the signal and noise changes with the squeezer parameter ⁹, and the optimal sensitivity is when it is aligned with the given frequency. For example, in Fig. 5.2, the peak sensitivity is at 5 kHz when the squeezer is off, at ~ 2 kHz at 95% threshold, and at 2.5 kHz at $\sim 85\%$ threshold which is the optimum squeezer parameter for 2.5 kHz. This is unlike degenerate internal squeezing where the peak remains at the sloshing frequency. Conversely, this demonstrates that using the sensitivity at a particular frequency cannot reliably find threshold for nondegenerate internal squeezing.

5.2 Comparison to stable optomechanical filtering

I now consider whether nondegenerate internal squeezing is a viable, all-optical alternative to stable optomechanical filtering. As discussed in Section 4.1, the only difference

⁷I make this point to clarify the effect of the squeezer parameter, however, for future detectors, the integrated sensitivity (e.g. from 1–4 kHz) is the more useful metric.

⁸That is not the threshold frequency Ω_{thr} .

⁹In particular, it moves from the sloshing frequency to the threshold frequency.

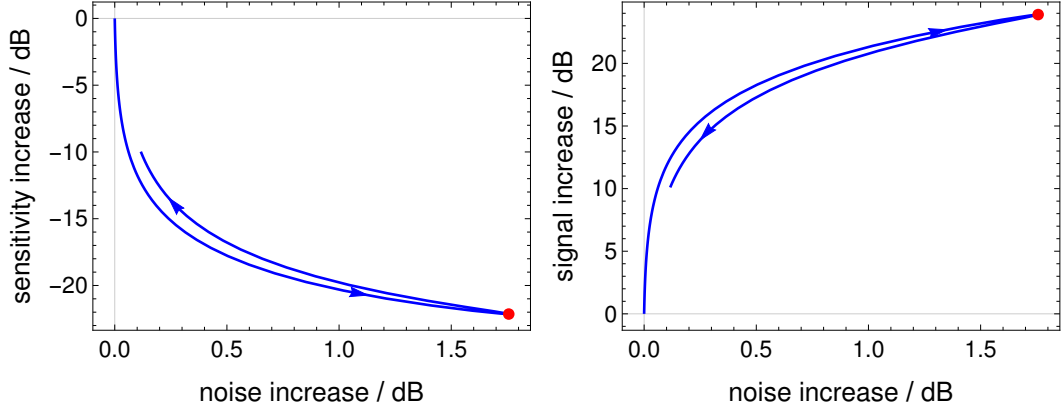


Figure 5.4: Nondegenerate internal squeezing’s sensitivity versus noise (left panel) and signal versus noise (right panel) at a given frequency of 2.5 kHz (in the middle of the 1–4 kHz band), varying the squeezing parameter up to threshold. The sensitivity (as the noise-to-signal ratio), noise, and signal are measured relative to their respective values at 2.5 kHz without squeezing, i.e. the signal increase is $20 \log_{10}(T_f/T_i)$ where T_i is the signal response at 2.5 kHz without squeezing and T_f is with squeezing. Increasing the squeezing parameter increases the signal more than the noise up to a point (the red dot at $\sim 85\%$ threshold) beyond which the signal decreases more than the noise as the peak frequency passes 2.5 kHz. This shows that the optimal squeezer parameter for maximum sensitivity at 2.5 kHz is below threshold. I use the parameter set in Table 4.1.

between the models of nondegenerate internal squeezing and stable optomechanical filtering is that the idler mode is optical and mechanical, respectively. This means that the idler loss has different values depending on whether it is optical or mechanical loss. In Fig. 5.5, I find the optical loss required to achieve the same sensitivity as the results for the optomechanical analogue in Ref. [1] that assume low mechanical loss determined by $T_{\text{env}} = 4 \text{ K}$ and $Q_m = 8 \times 10^9$. To validate this comparison¹⁰, I check that the lossless sensitivity and the sensitivity of a single-cavity detector agree with Ref. [1]. I show the sensitivity for the realistic losses from Section 3.1.2 and the more optimistic losses of 75 ppm arm loss and 100 ppm idler loss in Table 5.1. For these optimistic optical losses, the peak sensitivity and bandwidth are better than the optomechanical analogue with low mechanical loss, but for the realistic optical losses, the peak sensitivity is worse as shown in Fig. 5.5. Although predicting future technological progress is not rigorous, achieving

¹⁰Although I update χ to the lossy threshold χ_{thr} to maintain the same ratio as the lossless case, the authors in Ref. [1] do not update χ_m for the mechanical loss. By analogy to Fig. 4.7, I suspect that their squeezing and therefore sensitivity is higher than it would be for a fixed ratio, but the effect is small, e.g. my lossy threshold values are 99% and 99.9% of the lossless threshold and the change in sensitivity is less than the difference between any of my curves in Fig. 5.5. Therefore, I ignore this effect and I leave a more accurate comparison to future work.

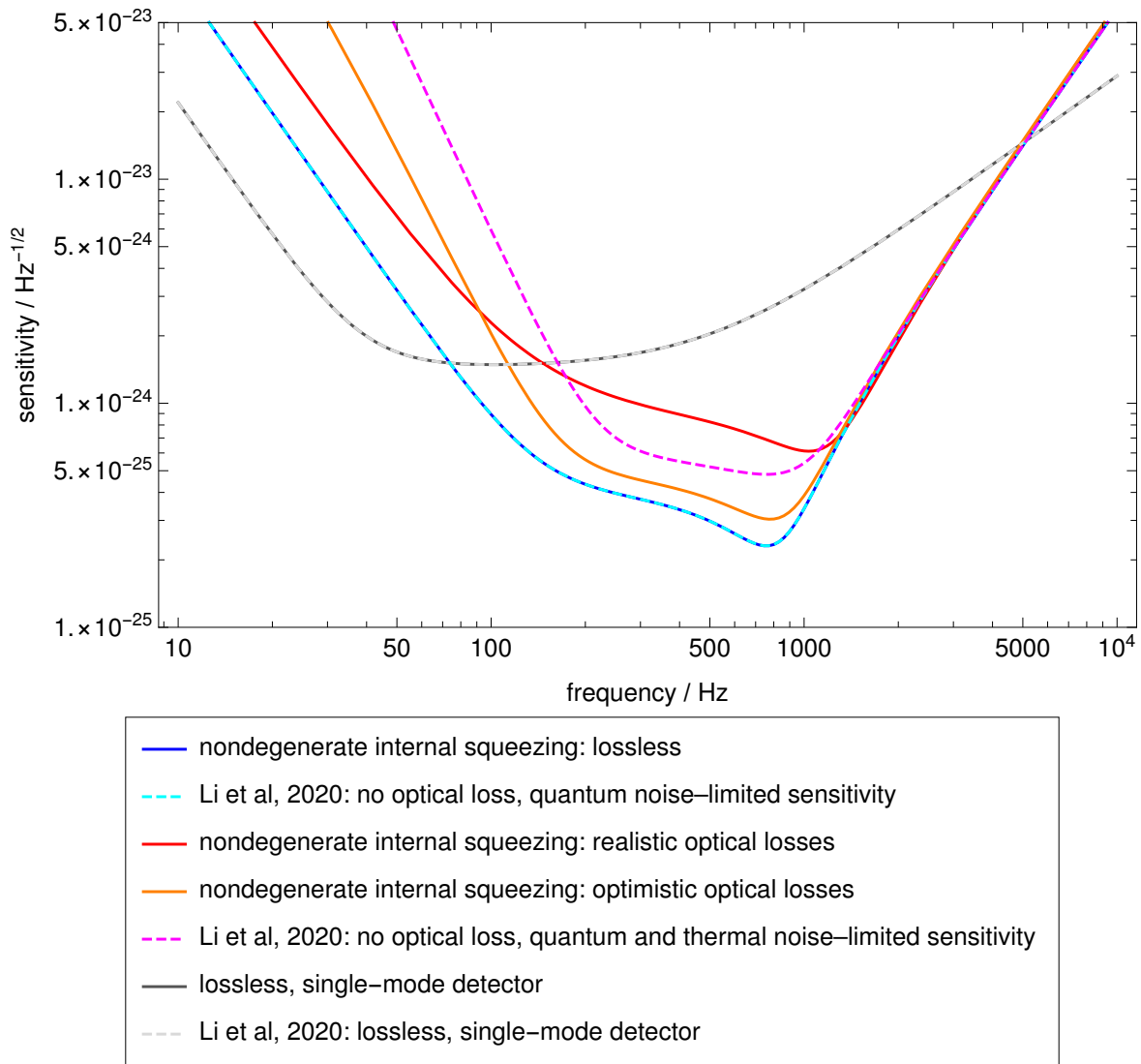


Figure 5.5: Nondegenerate internal squeezing (solid curves) compared to stable optomechanical filtering (dashed curves) where I use the data from Fig. 5 in Ref. [1] with permission from the authors [63]. Nondegenerate internal squeezing’s quantum noise-limited sensitivity with realistic optical loss is worse than the optomechanical system’s quantum and thermal noise-limited sensitivity with low mechanical loss ($T_{\text{env}} = 4 \text{ K}$ and $Q_m = 8 \times 10^9$) but is better than it with the optimistic optical loss in Table 5.1. I use the same 98.6% ratio to threshold as the lossless case and Ref. [1]. I validate this comparison using the lossless models and the model for a single-cavity detector (i.e. a Fabry-Perot Michelson interferometer with no signal-recycling cavity), which agree with Ref. [1]. I use the parameter set in Table 4.1 which is the same as Ref. [1].

arm intra-cavity loss, $T_{l,a}$ 75 ppm	idler mode intra-cavity loss, $T_{l,c}$ 100 ppm
---	---

Table 5.1: Optimistic optical losses for nondegenerate internal squeezing where the other losses and the rest of the parameter set are the same as Table 4.1.

losses somewhere between these realistic and optimistic optical losses appears at least as possible as the technological assumptions of the optomechanical analogue. In particular, the 100 ppm arm loss is already achievable and 75 ppm in the future is conservative [22], and the 1000 ppm idler loss inside the signal-recycling cavity is only a factor of two away from current technology [66]¹¹ compared to the mechanical requirements which are at least a factor of 16 away¹². Therefore, I conclude that nondegenerate internal squeezing is a viable, all-optical alternative to stable optomechanical filtering.

5.3 Feasibility for gravitational-wave detection

I now return to the motivating problem of improving kilohertz gravitational-wave sensitivity to detect new astrophysical sources. I explore the feasibility of nondegenerate internal squeezing for both kilohertz (e.g. 1–4 kHz) and broadband (e.g. 0.1–4 kHz) detection but do not aim to find the best configuration for future detectors.

I consider using nondegenerate internal squeezing to detect *kilohertz* gravitational waves from Section 1.1.1, which I represent with the case example of the binary neutron-star merger¹³. The estimated sensitivity required to reliably detect a typical such “post-merger” signal is $\sqrt{S_h} = 5 \times 10^{-25} \text{Hz}^{-1/2}$ from 1–4 kHz [8]¹⁴. In Fig. 5.6, I compare this target to the sensitivity of nondegenerate internal squeezing with the realistic losses in Table 4.1 and the optimistic losses in Table 5.1. For 500 Hz readout rate at 95% threshold, the target is achieved at the peak frequency of ~ 1.5 kHz with optimistic losses but is not achieved for realistic losses and/or decreased squeezing (it is around a factor of two away for realistic losses and 90% threshold). However, this target sensitivity and frequency range are not definitive as they depend on the equation-of-state of the neutron stars

¹¹Therefore, the optimistic 100 ppm idler loss is a factor of 20 away.

¹² $T_{\text{env}}/Q_m = 9.7 \times 10^{-9} K$ [61] compared to $6 \times 10^{-10} K$ required in Ref. [26].

¹³Other kilohertz astrophysical sources are predicted to require similar or greater sensitivity [8].

¹⁴This target assumes the maximal detector response, i.e. from a gravitational wave with polarisation aligned to the arms.

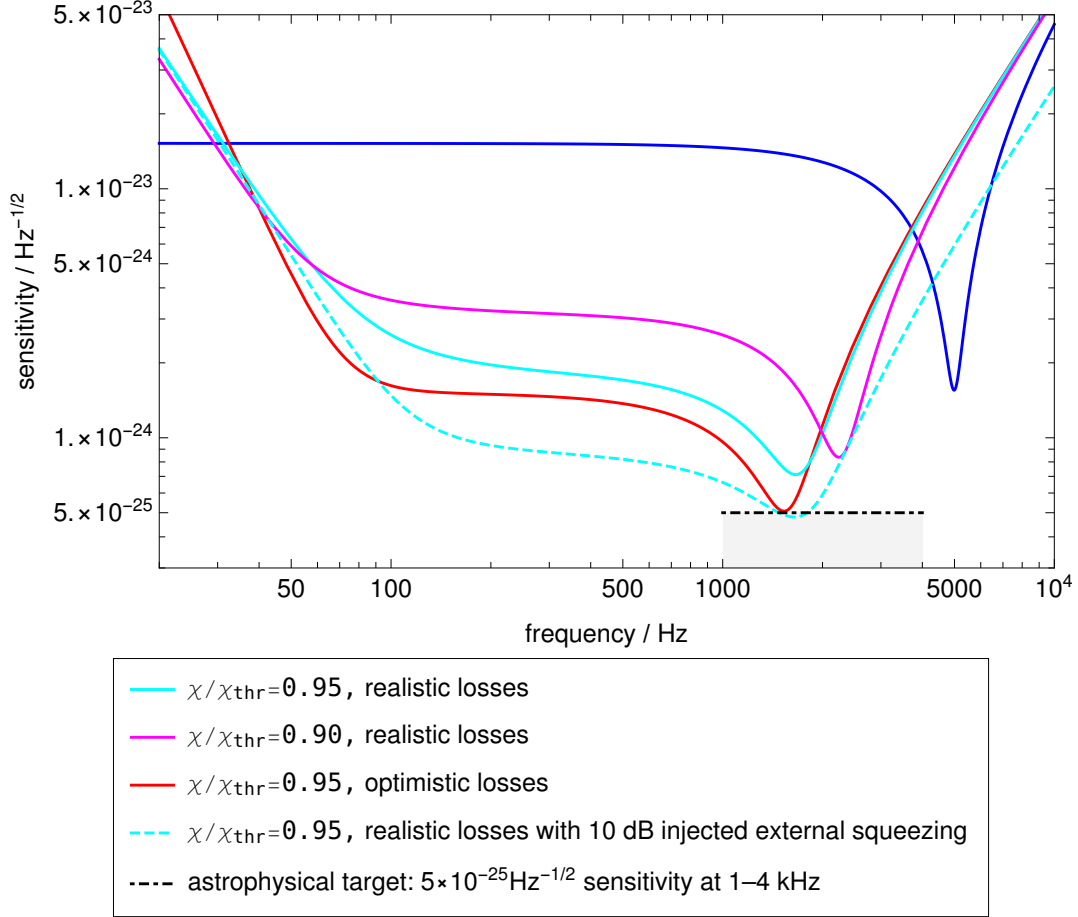


Figure 5.6: Nondegenerate internal squeezing’s sensitivity compared to the astrophysical, kilohertz sensitivity target [8]. The blue curve shows the sensitivity without squeezing. Under ideal conditions, i.e. 95% threshold ($\chi/\chi_{\text{thr}} = 0.95$), optimistic losses from Table 5.1, 500 Hz signal readout rate, and with zero idler readout rate, the target can be achieved at the peak frequency. For more realistic losses from Table 4.1, decreased squeezer parameter (e.g. 90% threshold), and/or higher readout rate (not shown, e.g. 5 kHz) the target is not achieved. These results are without external squeezing. With 10 dB injected, frequency-dependent external squeezing as discussed in Section 2.3.1, realistic losses and 95% threshold can achieve the target at the peak frequency, where the losses mean that the measured noise is only reduced by 7.2 dB. I use the parameter set in Table 4.1 which has not been optimised for 1–4 kHz detection, and these results are without increased circulating power.

which is not fully constrained to date [7, 8], indeed, understanding it better is one of the goals of kilohertz detection, kilohertz improvement close to this target might be sufficient. Although nondegenerate internal squeezing does not meet the target sensitivity across the full 1–4 kHz band, it improves kilohertz sensitivity enough by itself that together with other improvements, such as external squeezing, it would be feasible with realistic losses, 90–95% squeezer parameter, and low readout rate to achieve it for part of the band, as shown for 10 dB external squeezing and realistic losses in Fig. 5.6. This agrees with Ref. [8] which achieved the target across 1–4 kHz using unstable optomechanical filtering¹⁵ with 10 dB injected squeezing but with twice the circulating power. In summary, although nondegenerate internal squeezing does not achieve the target sensitivity across the full 1–4 kHz, its feasibility for kilohertz detection is still promising.

Although kilohertz detection motivated this work, the *broadband improvement* from 0.1–4 kHz using nondegenerate internal squeezing could be used to detect more of the sources that detectors like Advanced LIGO currently see but over a broader range of frequencies [6]. As shown in Fig. 5.6, nondegenerate internal squeezing improves sensitivity from 100–1000 Hz, along with the 1–4 kHz improvement above, for realistic losses, 95% threshold, and readout rates below 5 Hz¹⁶. Here, this broadband sensitivity improvement is less than the kilohertz improvement above (e.g. it does not improve it beyond $1 \times 10^{-24} \text{Hz}^{-1/2}$ for 100–1000 Hz) because of the trade-off between peak sensitivity and bandwidth. This improvement is feasible and promising as long as the worsened radiation-pressure noise below 50 Hz is not an issue, e.g. for binary neutron-star mergers [8]. Therefore, the potential benefits of nondegenerate internal squeezing should not just be considered for kilohertz sensitivity.

5.4 Chapter summary

In this chapter, I have applied my model of nondegenerate internal squeezing to gravitational-wave detection. Firstly, I showed that the signal readout is limited by idler

¹⁵There is not an exact correspondence between nondegenerate internal squeezing and the unstable case, but I reference it as a similar configuration that cannot achieve the target by itself but can with other improvements.

¹⁶For reference, the current sensitivity of Advanced LIGO at 100 Hz is $\sqrt{S_h} = 8 \times 10^{-24} \text{Hz}^{-1/2}$ [67].

loss and affected by detection loss. The nondegenerate case's low tolerance to idler loss means that it is not universally more loss tolerant than degenerate internal squeezing, but it is more tolerant to detection loss. Then, I showed that nondegenerate internal squeezing is a viable, all-optical alternative to stable optomechanical filtering. Finally, I showed that nondegenerate internal squeezing improves kilohertz sensitivity by enough that it might feasibly enable the detection of kilohertz gravitational waves.

Alternative readout schemes for nondegenerate internal squeezing

In this chapter, I explore using the idler mode for the readout of nondegenerate internal squeezing. In the previous chapter, I showed that idler loss and the idler readout rate limit the sensitivity of signal readout. Here, I show how the idler readout rate can instead be used beneficially to measure the gravitational-wave signal. Since a readout scheme using the mechanical idler mode of stable optomechanical filtering has been proposed [29], a comprehensive understanding of nondegenerate internal squeezing also requires idler readout to be understood. This work emerged during the present research and is somewhat separate from my initial motivation to improve kilohertz sensitivity. Firstly, in Section 6.1, I define idler readout and explain how it can be combined, incoherently and coherently, with signal readout. Secondly, in Section 6.2, I characterise these alternative readout schemes, including their stability, threshold, and high loss limit. I also compare the general behaviour of idler readout to signal readout. Thirdly, in Section 6.3, I find the tolerance of idler readout to realistic optical losses compared to signal readout. I also find the effect of changing the pump phase. Finally, in Section 6.4, I consider the feasibility of using an alternative readout scheme for broadband gravitational-wave detection.

6.1 Conceptual understanding and model

The idler mode \hat{c} at $\omega_0 + \Delta$ can be used for measurement (called “*idler readout*”) because the squeezer couples the gravitational-wave signal from the signal mode \hat{b} at ω_0 into the idler mode. Therefore, unlike signal readout, the idler readout’s performance cannot be

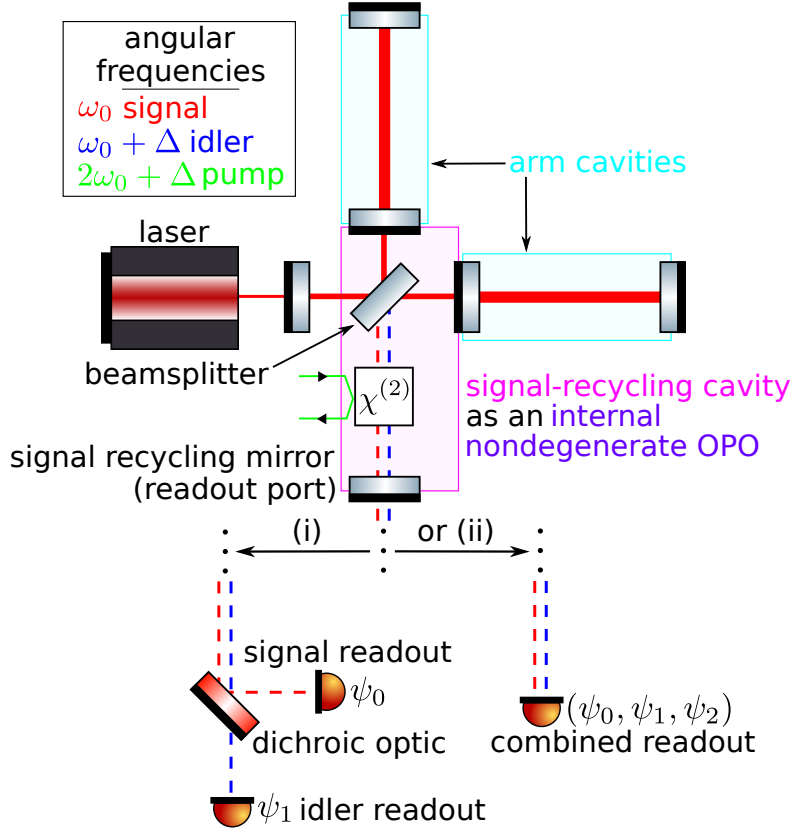


Figure 6.1: Nondegenerate internal squeezing possible readout schemes that were represented by the photodetector in Fig. 4.1. The light can either be (i) split at a dichroic optic to measure the signal and idler separately or (ii) coherently combined at the same photodetector, where the vertical ellipses represent where the readout schemes join the main configuration. When measuring the modes separately, the quadratures of the mode can be still be coherently combined, e.g. the idler quadratures can be combined at angle ψ_1 .

compared to when the squeezer is off because then there is no signal. This change in mode structure also means that idler readout is not PT-symmetric in the lossless limit and, therefore, I expect different behaviour than the signal readout ¹. The idler readout rate ², previously a source of loss for the signal readout, can be used to measure the idler mode separately or coherently combined with the signal mode as shown in Fig. 6.1. That measuring the idler mode simply requires detecting the light leaking out through the signal-recycling mirror is an advantage of this all-optical configuration in comparison to measuring the mechanical idler mode of stable optomechanical filtering [29].

Idler and coherently combined readout *use the same model as signal readout* from Sec-

¹Although the internal mode structure of the configuration is the same (see Appendix B), the idler readout scheme “sees” the configuration differently.

²Which can be made different to the signal readout rate by using a dichroic signal-recycling mirror.

tion 4.2 and combine the quadratures at the photodetector as described for the nondegenerate OPO in Section 2.2.2. Specifically, let the signal and idler quadratures of $\vec{X}_{\text{PD}}(\Omega)$ from Eq. 4.8 be coherently combined to measure ³

$$\hat{X}_{\text{com}}(\Omega) = (\cos(\psi_2) \cos(\psi_0), \cos(\psi_2) \sin(\psi_0), \sin(\psi_2) \cos(\psi_1), \sin(\psi_2) \sin(\psi_1)) \cdot \vec{X}_{\text{PD}}(\Omega). \quad (6.1)$$

By Eq. 4.15, there is gravitational-wave signal in every quadrature except the first signal quadrature $\hat{X}_{b,1}$ and the idler combination $-\sin(\phi)\hat{X}_{c,1} + \cos(\phi)\hat{X}_{c,2}$ for the pump phase ϕ . Therefore, \hat{X}_{com} contains the gravitational-wave signal unless $\psi_0 = \psi_2 = 0$ or $\psi_2 = \pi/2$, $\psi_1 = \phi + \pi/2$, respectively, as long as the squeezer is on. Let the coherently combined readout be defined to measure \hat{X}_{com} for some arbitrary combination of signal and idler that contains the gravitational-wave signal, where the readout angles (ψ_0, ψ_1, ψ_2) can change with frequency. Let the idler readout be defined to maximise the gravitational-wave signal response by measuring $\cos(\phi)\hat{X}_{c,1} + \sin(\phi)\hat{X}_{c,2}$, i.e. by matching ψ_1 to the pump phase ϕ ⁴. Like the signal readout measuring $\hat{X}_{b,2}$ in Eq. 4.16, this combination might not maximise the sensitivity because it does not consider the noise. Finally, *incoherently combined readout* uses the separate signal and idler readouts in Fig. 6.1 at different frequencies. This readout scheme does not measure the correlations between the signal and idler unlike the coherently combined readout as discussed in Section 2.2.2. Therefore, the incoherently combined readout can only achieve the envelope of the separate readouts' sensitivity curves but the coherently combined readout might achieve better, e.g. because the correlations might reduce the noise.

6.2 Results

I analyse these alternative readouts *using the same methodology as the signal readout* in the previous two chapters. To start with, some of the behaviour is the same as the signal readout. The idler and combined readouts have the same singularity threshold and

³Here, the combination angles $\psi_0, \psi_1, \psi_2 \in [0, 2\pi)$ can be chosen by the phase of the local oscillator in a homodyne readout scheme for example [38].

⁴This is the idler quadrature connected to the second signal quadrature, which maximises the signal, by the squeezer.

stability as signal readout in Section 4.4. This is because all of the (co)variances of the signal and idler modes at the photodetector from Eq. 4.14 have a common denominator that physically relates to them both being inside the signal-recycling cavity. The high arm loss limit is also the same as signal readout in Section 4.3 as the shot noise of idler readout reduces to that of a nondegenerate OPO between the signal-recycling mirror and a fully-reflective input test mass. The coherently, equally combined readout, i.e. with $\psi_2 = \pi/4$, reduces to a degenerate OPO as in Section 2.2.2 ⁵. Due to limited research time, I have not explored coherently combined readout further yet. I will leave it to future work and focus on the idler readout here.

The *general behaviour* of idler readout is different to signal readout which I compare to in Fig. 6.2 ⁶. The noise response of the idler readout has a peak with less anti-squeezing but at the same frequency as the signal readout because the peak frequency is determined by the common singularity threshold frequency. The idler also has worse radiation-pressure noise than the signal. The signal response of the idler decreases the response at and above the peak but improves it below the peak down to DC compared to the signal readout. The resulting sensitivity of the idler compared to the signal readout is the same below 30 Hz, improves from ~ 30 –500 Hz, and worsens above 500 Hz as shown in Fig. 6.2. The squeezer parameter must be non-zero for idler readout, and increasing the squeezer parameter improves the idler sensitivity from around 50 Hz up to the peak frequency but also increases the radiation-pressure noise. The result that the idler readout improves the sensitivity around 100 Hz agrees with Ref. [29] that considers idler readout of the mechanical mode for the optomechanical analogue.

signal mode transmissivity, $T_{\text{SRM},b}$	0	idler mode transmissivity, $T_{\text{SRM},c}$	0.046
signal readout rate, γ_R^b	0	idler readout rate, γ_R^c	500 Hz

Table 6.1: Idler readout parameter set is the same as Table 4.1 for the signal readout except with the signal and idler readout rates exchanged as shown. The idler readout results use these parameters unless stated otherwise.

⁵Although I thought that this readout might also make nondegenerate internal squeezing recover degenerate internal squeezing, this is not true as the noise response has squeezing and anti-squeezing at different frequencies in the same quadrature, unlike the degenerate case. I suspect that this is because the idler is not resonant in the arms and therefore the signal and idler modes are not symmetric. This could be verified by making the idler frequency resonant in the arms, which I leave to future work.

⁶Here, I change the readout rates from Table 6.1 by fixing the signal transmissivity and changing the signal-recycling cavity length and idler transmissivity.

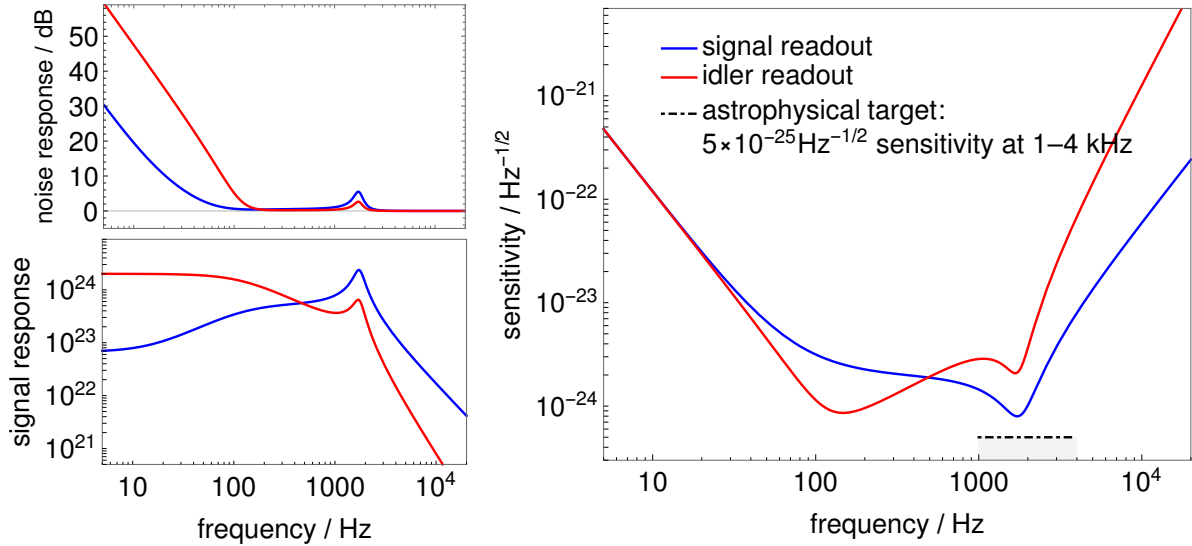


Figure 6.2: Nondegenerate internal squeezing idler readout compared to signal readout for the same squeezing (95% threshold), showing the noise (upper-left panel), signal (bottom-left panel), and sensitivity (right panel). I use the parameter set from Table 6.1 but with 500 Hz signal readout rate and 5 Hz idler readout rate by appropriately changing the signal-recycling length and respective transmissivities to adjust for the added loss with both ports open. The astrophysical kilohertz sensitivity target is shown for later comparison. Idler readout trades sensitivity above and at the peak (e.g. 0.5–10 kHz) for sensitivity below the peak (e.g. 50–500 Hz) down to where the improvement in the signal DC response cancels with the amplified radiation-pressure noise (e.g. 30 Hz). If the idler readout rate is instead greater than the signal readout rate (not shown) the two sensitivities are approximately equal except above 10 kHz.

For *different readout rates*, the general behaviour is the same: idler readout is better at “low–middle” frequencies and worse at “high” frequencies than signal readout. If the idler readout rate is increased, then the DC signal response improvement diminishes at the same rate that the radiation-pressure noise increases such that the “low” frequency sensitivity remains the same. The idler readout is most useful when the readout rates are comparable or the idler is smaller than the signal readout rate, e.g. the case shown in Fig. 6.2.

6.3 Idler readout tolerance to optical loss

I consider the tolerance of idler readout to optical loss using the parameter set in Table 6.1. I use a higher idler readout rate here than in Fig. 6.2 (500 versus 5 Hz respectively) because closing the signal readout port reduces the loss and narrows the peak, therefore,

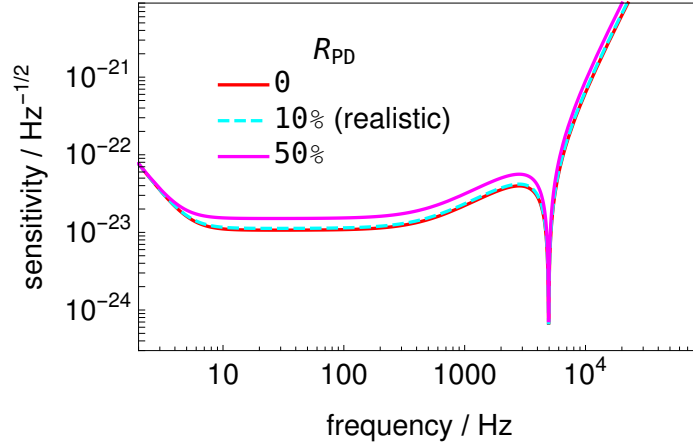


Figure 6.3: Nondegenerate internal squeezing idler readout tolerance to detection loss (R_{PD}). Idler readout's tolerance to detection loss is similar to signal readout's, shown in Fig. 5.1, with uniform loss of sensitivity except around the peak frequency and where the radiation-pressure noise dominates because there the loss in signal and noise are roughly equal. I do not compare the idler readout to the performance without squeezing because no gravitational-wave signal reaches the idler mode with the squeezer off. I use the parameter set in Table 6.1 and 95% threshold.

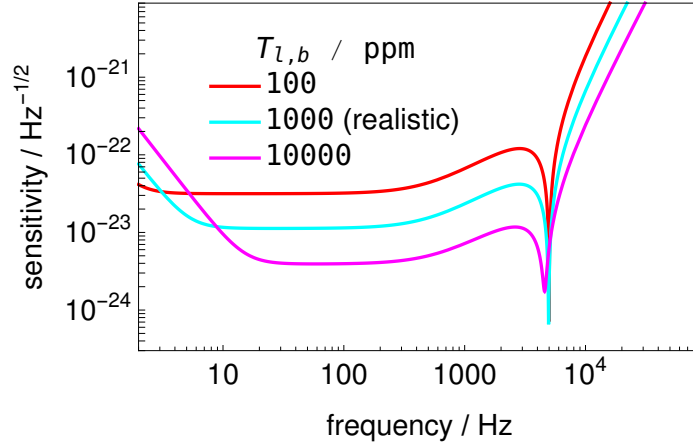


Figure 6.4: Nondegenerate internal squeezing idler readout tolerance to signal mode intra-cavity loss ($T_{l,b}$). Signal loss decreases the peak frequency and worsens the radiation pressure noise of idler readout but broadens the sensitivity (e.g. from 10–1000 Hz) independently of the idler readout rate. Opening the signal readout port as in Fig. 6.2 would introduce signal loss on the order of 10000 ppm. I use the parameter set in Table 6.1 and 95% threshold.

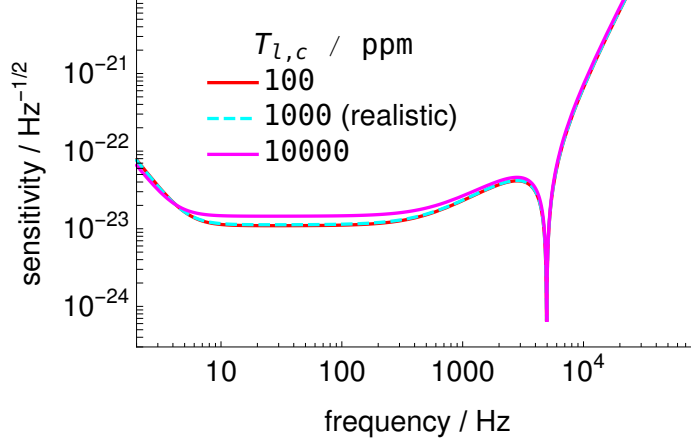


Figure 6.5: Nondegenerate internal squeezing idler readout tolerance to idler intra-cavity loss ($T_{l,c}$). Idler readout is tolerant to idler loss but less resistant than signal readout is to signal loss, shown in Fig. 5.2. In either case, the readout rate dominates the realistic intra-cavity loss rate. The idler readout is least tolerant at 10–1000 Hz, but increasing the idler loss ten-fold from the realistic level decreases sensitivity by less than a factor of two. I use the parameter set in Table 6.1 and 95% threshold.

meaning that a lower idler readout rate is not required to narrow the peak ⁷. Using the same methodology as the signal readout in Section 5.1, I consider the detection, signal, idler, and arm losses in turn.

Firstly, as shown in Fig. 6.3, the realistic *detection loss* affects the idler readout similarly to the signal readout as it uniformly worsens sensitivity by 10% except where the noise is far from vacuum, e.g. around the peak and below 3 Hz. This tolerance is independent of the idler readout rate.

Secondly, as shown in Fig. 6.4, the *signal mode intra-cavity loss* affects the idler readout differently than the way that any of the losses affected the signal readout, which reflects the change in mode structure. The signal loss increases the radiation-pressure noise, broadens the shot noise peak, and decreases the signal peak, but uniformly, strongly (e.g. by at least a factor of two) amplifies the signal response away from the peak. The effect on the signal response is similar to how loss damps a harmonic oscillator resonance, lowering the peak but broadening the bandwidth, except that the broadening extends to all frequencies away from the peak. The net result of signal loss is that the sensitivity worsens at the peak and at low frequencies below ~ 10 Hz where the radiation-pressure

⁷Narrowing the peak increases its height, trading bandwidth for peak sensitivity.

noise dominates, but improves at all other frequencies. I find that idler readout is strongly affected by realistic signal loss and that changing the idler readout rate does not improve the tolerance. When the signal readout port is open, the signal loss effectively increases by 46000 ppm and the idler readout sensitivity resembles Fig. 6.2 with diminished a peak but broad sensitivity from 10–1000 Hz. I will later consider whether purposefully opening the signal readout port could be used to improve broadband sensitivity.

Thirdly, as shown in Fig. 6.5, the *idler mode intra-cavity loss* decreases the idler readout’s sensitivity away from the peak. This is unlike the signal readout’s tolerance to either signal loss, which decreased the sensitivity at the peak in Fig. 5.2, or to idler loss, which decreased the sensitivity everywhere but improved the radiation-pressure noise in Fig. 5.3. However, at realistic 1000 ppm idler loss, the effect on idler readout is negligible because it is dominated by the noise through the readout port, in the same way that realistic signal loss is negligible for signal readout.

Finally, similarly to signal readout, realistic *arm intra-cavity loss* has a negligible effect on idler readout if the circulating power is fixed, e.g. increasing the arm loss a hundredfold affects the peak sensitivity by less than a factor of two.

In summary, idler readout is affected differently to signal readout by some of the losses, which is due to the different mode structure, i.e. which losses the noise and signal encounter on their way to each readout. For realistic losses, arm and signal losses affect the noise negligibly compared to idler and detection loss. However, *the signal loss has the dominant effect on the sensitivity* out of the losses because of its effect on the signal response as seen by comparing Fig. 6.4 to Figs. 6.3 and 6.5. Like the signal readout, the dominant noise above 100 Hz remains the shot noise from the readout port rather than any of the losses.

6.3.1 Variational idler readout and tolerance to pump phase

In Section 6.1, I defined the idler readout to optimise the signal response by matching the readout combination angle to the pump phase, e.g. $\psi_1 - \phi = 0$. Now, I consider the tolerance to changes in the relative phase $\psi_1 - \phi$. As shown in Fig. 6.6, a change of $\pi/4$ in the relative phase changes the sensitivity by at most a factor of two, and since $\pi/4$ is

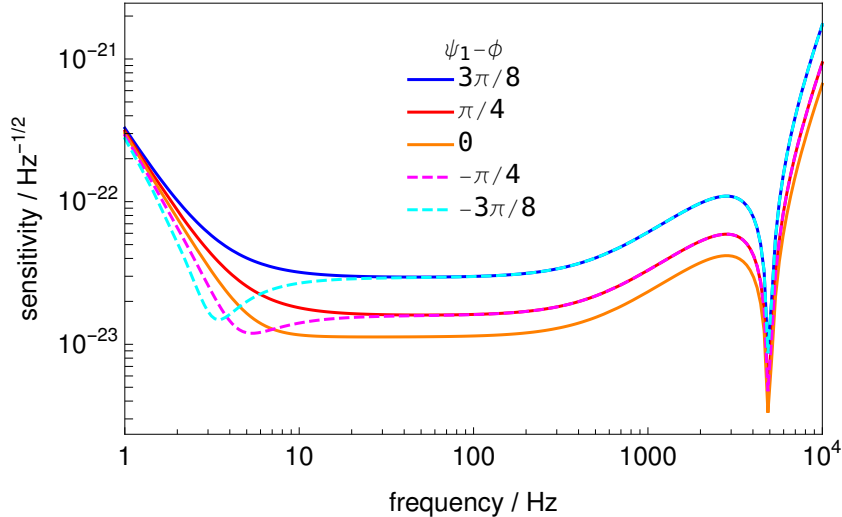


Figure 6.6: Nondegenerate internal squeezing idler readout tolerance to the relative phase between the pump phase ϕ and idler combination angle ψ_1 . Changing the relative phase affects the radiation-pressure noise, signal peak, and DC signal response. The signal response decreases because there is no signal response for a relative phase of $\pm\pi/2$ as discussed in Section 6.1. The tolerance is high to realistic variations in the relative phase (which are far smaller than $\pi/4$ [35]). If the relative phase is fixed within $(-\pi/2, 0)$, then the noise is squeezed between 1–20 Hz and the sensitivity is improved. If the idler readout rate is changed, then the position of the squeezing peak changes. I use the parameter set in Table 6.1.

far larger than the realistic variation in the controlled relative phase [35], I assume that the relative phase is fixed. The sign of the relative phase does not affect the sensitivity except at “low” frequencies where the noise for negative relative phases is squeezed, e.g. $\psi_1 - \phi = -\pi/4$ around 5 Hz in Fig. 6.6. This is because of correlations between the idler quadratures created by the radiation pressure interaction since the relevant off-diagonal terms in Eq. 4.14 and the squeezing vanishing if the radiation pressure is turned off⁸. Similar squeezing occurs when the signal quadratures are combined. This squeezing could be used in a variational readout scheme [55] where the relative phase is made frequency-dependent to squeeze the radiation-pressure noise around 1–10 Hz using $\psi_1 - \phi < 0$ but use the optimal signal response $\psi_1 - \phi = 0$ above 10 Hz. Although at these frequencies below 100 Hz, quantum noise is not the dominant noise source for current

⁸This is an example of “ponderomotive” squeezing where the optomechanical interaction at the test mass squeezes the reflected light and introduces correlations between the signal quadratures that appear in the idler via the squeezer [68]. The optomechanical interaction produces squeezing because it couples the amplitude of the light, which affects the radiation pressure, to the propagation phase of the light acquired by the displacement of the mass.

gravitational-wave detectors [18], it might limit future detectors as it is the fundamental noise floor and therefore this scheme is worth further examination. To determine whether this variational readout scheme could be feasible for future detectors, the relative size of the other 1–100 Hz frequency noise sources would have to be considered, e.g. thermal, seismic, Newtonian, and control-system noise [18]. This could form part of a broader study of the coherently combined readout scheme which I leave to future work.

6.4 Idler readout for gravitational-wave detection

I now consider the feasibility of using the idler readout for gravitational-wave detection. By Fig. 6.2, the idler readout performs worse at kilohertz than the signal readout and therefore I do not consider using the idler readout for improving kilohertz sensitivity. However, in my exploration of nondegenerate internal squeezing, the possibility of improving broadband sensitivity has emerged despite my initial motivation to improve kilohertz sensitivity. Signal readout is already promising for 0.1–4 kHz broadband detection as discussed in Section 5.3, but idler readout performs better from 10–1000 Hz than signal readout by Fig. 6.2⁹. An incoherently combined readout scheme could achieve the envelope of the signal and idler sensitivities such that the idler could be used at “low” frequencies (0.01–1 kHz) and the signal at “high” frequencies (1–4 kHz). In Fig. 6.2, the incoherently combined readout has at least $2 \times 10^{-24} \text{Hz}^{-1/2}$ sensitivity from around ~ 80 –2500 Hz which overcomes the loss associated with having both readout ports open¹⁰. Therefore, nondegenerate internal squeezing could feasibly use incoherently combined readout to better improve broadband 0.1–4 kHz gravitational-wave detection. Exploring coherently combined readout, including the variational readout suggested in Section 6.3.1, for the possibility of even greater improvement is left to future work and will be discussed in the next chapter.

⁹Another benefit of idler readout is that the frequency difference Δ can be chosen to match the highest quantum efficiency photodiodes available since Δ does not otherwise affect the sensitivity in Eq. 4.8. This is promising because $2\mu\text{m}$ signal readout currently has low quantum efficiency [69].

¹⁰This performs better than the idler readout separately with the signal readout port open.

6.5 Chapter summary

In this chapter, I have explored how measuring the idler mode changes the performance of nondegenerate internal squeezing. Firstly, I characterised the stability, threshold, high arm loss limit, and performance of idler readout, and showed that idler readout, compared to signal readout, improves “low” frequency sensitivity (around 100 Hz) at the cost of “high” frequency sensitivity (around 1 kHz). Then, I showed that idler readout is limited by signal loss followed by detection loss. Finally, for gravitational-wave detection, I showed that the most promising application of idler readout at present ¹¹ is to use incoherently combined signal and idler readouts for broadband detection from 0.1–4 kHz, possibly with variational readout of the idler to squeeze the radiation-pressure noise.

¹¹At least, among those that I considered.

Conclusions and future work

In this thesis, I have investigated nondegenerate internal squeezing from the perspectives of general quantum metrology and gravitational-wave detection. Firstly, using an analytic Hamiltonian method, I have developed a model of nondegenerate internal squeezing that I validated by showing that it reduces to the correct high and low optical loss limits. I have shown that the configuration is stable and calculated its squeezing threshold. I compared the different possible readout schemes and showed that signal readout is limited by idler loss and idler readout is limited by signal loss. Secondly, using my model, I have evaluated the feasibility of nondegenerate internal squeezing for gravitational-wave detection in comparison to two existing proposals. I have found that it is a viable all-optical alternative to stable optomechanical filtering and that it is more resistant than degenerate internal squeezing to detection loss. Finally, I have shown that nondegenerate internal squeezing using signal readout, and without increasing circulating power, can feasibly improve kilohertz sensitivity, e.g. to the predicted 1–4 kHz gravitational waves from the remnant of a binary neutron-star merger. I have also shown that using incoherently combined signal and idler readouts can improve broadband 0.1–4 kHz sensitivity. In summary, I have found that nondegenerate internal squeezing is a detection loss-resistant configuration that improves quantum noise–limited sensitivity and could be used for kilohertz (1–4 kHz) or broadband (0.1–4 Hz) gravitational-wave detection as an all-optical alternative to existing proposals.

This thesis *characterises nondegenerate internal squeezing* which was previously understood only in the lossless case and by analogy to stable optomechanical filtering. Although the Hamiltonians of nondegenerate internal squeezing and stable optomechanical filtering are theoretically equivalent under a certain mapping of optical to mechanical modes, I have shown that, in practice, the feasibility of each configuration is different and that the

loss requirements of nondegenerate internal squeezing are at least as realistic as stable optomechanical filtering. Moreover, I have characterised aspects of nondegenerate internal squeezing that were not present in the literature to date but are essential to a thorough understanding such as the squeezing threshold and the tolerance to the different sources of optical loss.

7.1 Future work

The results in this thesis indicate several possible avenues of future research into nondegenerate internal squeezing.

The *model in this thesis could be extended* to make stronger claims about the best configuration for future detectors by removing some of the simplifying assumptions used. Some of my assumptions limit the frequency range in which the estimated sensitivity is accurate such as to below the arm cavity free spectral range of 37.5 kHz to maintain the single-mode approximation ¹. These assumptions could be avoided to predict the behaviour of nondegenerate internal squeezing outside the 0.1–4 kHz frequency range that I study, e.g. by using a multi-mode model [29]. Similarly, the semi-classical pump and no-pump-depletion approximations should be dropped to predict the behaviour above threshold and more accurately at 95–100% threshold [39]. A pump depletion model could also validate my singularity threshold technique. There are other possible extensions to enrich understanding such as a more thorough stability analysis [29], verifying the high loss limit using a transfer matrix method (e.g. in Ref. [23]), and checking if nondegenerate internal squeezing with coherently combined readout reduces to degenerate internal squeezing when the idler is coupled to the arm mode (as discussed in Section 6.2).

When these extended models are used to judge the *feasibility of future detectors*, my assumptions about what losses are realistic and what sensitivity is required should be revisited given the unknowns of future technological and astrophysical progress. These assumptions are hard to improve upon and should be updated with the best understanding of the time. The extensions to the model might necessitate using numerical modelling

¹Other such assumptions include assuming that quantum noise is the dominant noise source and that the test masses are horizontally free-falling which both restrict the frequencies to be above 100 Hz.

in an optics simulation tool such as FINESSE [64]². Such a tool could also be used as further validation of the analytic model of nondegenerate internal squeezing, however, this is not a priority since I have already provided confidence in my model by showing that it reduces to the correct limits. Using either an analytic or numerical model, the sensitivity could then be optimised to discover the best design parameters for a realistic future detector and to determine whether such an optimised detector could meet the astrophysical sensitivity targets.

Coherently combined readout (as defined in Section 6.1) might lead to better sensitivity than the other readout schemes because of the signal-idler correlations which I have derived but not studied. This is motivated by promising results for the coherently combined readout of stable optomechanical filtering [29]. To characterise the coherently combined readout, I would first examine the effects of realistic optical loss, the readout rates, pump power, pump phase, and the readout angles on the signal and noise responses. Then, I would find a Wiener filter for the sensitivity, i.e. the readout angles to maximise the sensitivity at each frequency. Since the choice of angles can recover signal or idler readout, this Wiener filter would be at least as sensitive as either readout separately or incoherently combined³. Finally, I would compare this optimum sensitivity to the astrophysical targets to judge the feasibility of gravitational-wave detection. In summary, coherently combined readout should be studied to find the best possible sensitivity using nondegenerate internal squeezing.

The *PT-symmetry* of lossless nondegenerate internal squeezing at threshold (discussed in Sections 3.4 and 4.1) could also be further investigated [71]. In particular, it could be checked whether the PT-symmetry is responsible for the enhanced sensitivity. PT-symmetry theory only predicts there to be enhanced sensitivity if the Exceptional Point (see Section 3.2) is not accidental, i.e. that the degenerate real eigenvalue pair at threshold becomes a complex eigenvalue pair above threshold [72, 73]. This has not been shown and would mean that the Hamiltonian is not Hermitian above threshold which is a situation studied in PT-symmetry theory [60]. To determine if this is the case using a pump-

²This would require the addition of a nondegenerate internal squeezer component similar to the degenerate internal squeezer component (`nle`) currently available on the PyKat developer branch but otherwise could be modelled using the standard library [70].

³Also, variational readout restricted to only combining the signal quadratures could determine the optimum signal readout and, similarly, the optimum idler readout.

depletion model, either the boundedness-from-below of the Hamiltonian could be checked or the eigenvalues could be explicitly calculated. PT-symmetry could also be investigated in the lossy case, where it is expected to break, and with radiation pressure included (as in Ref. [1] for the optomechanical analogue).

Finally, the model in this thesis could be used to design an *experiment to demonstrate nondegenerate internal squeezing* and enhanced interferometer sensitivity. This would require using the parameters and losses realistic to a contemporary, table-top squeezing experiment (e.g. Ref. [74]).

Final word

The future work suggested above is only some of the potential research motivated by the promising results about nondegenerate internal squeezing in this thesis ⁴. By possibly improving the sensitivity of future gravitational-wave detectors, this thesis is part of the effort to detect and study new signals from astrophysical sources such as the predicted kilohertz gravitational-waves from the remnants of binary neutron-star mergers. This could lead to a better understanding of these astrophysical sources such as insights on the exotic states of matter within neutron stars. The results in this thesis also apply beyond gravitational-wave detection to general quantum metrology ⁵.

⁴The results in this thesis will form the core of a future journal paper.

⁵For example, as shown in Ref. [1], the Hamiltonian of nondegenerate internal squeezing is also equivalent to a device that potentially improves axion detection to constrain theories of dark matter [75, 76].

Stability of degenerate internal squeezing

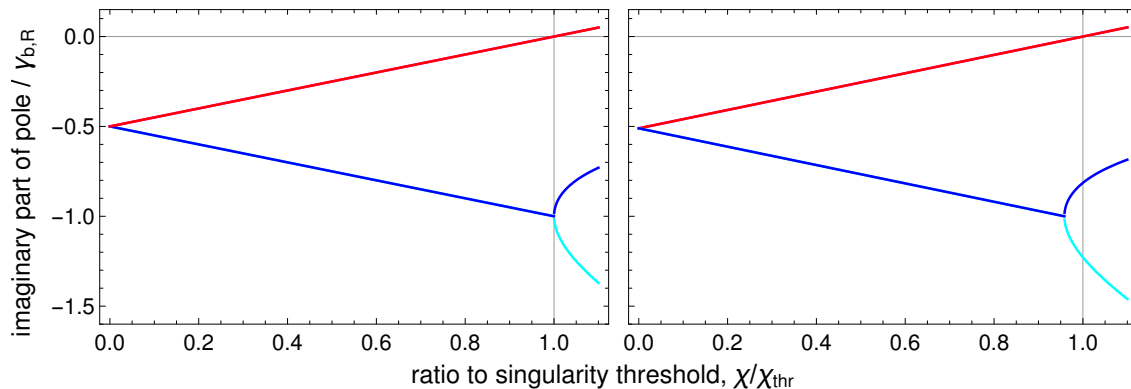


Figure A.1: Degenerate internal squeezing’s stability for lossless (left panel) and lossy (right panel) cases. The different colours indicate different poles found numerically. A positive imaginary part of a pole indicates instability. Both cases are stable below singularity threshold. I use the parameters in Table 3.1.

I determine the stability of degenerate internal squeezing via the poles of its noise and signal responses. These responses are related fractions of polynomials. The denominator of the noise response squared is $\Omega^4 q(\Omega, \chi)$ where q is a polynomial in Ω, χ [23]. Since the zero $\Omega = 0$ comes from the horizontally free-falling mass assumption, the remaining zeros of the noise denominator are the zeros of q (which are shared with the signal response [23]). In the complex Ω plane, if any of these poles ¹ have a positive imaginary part, then the system is unstable [65]. As shown in Fig. A.1, therefore, degenerate internal squeezing is stable in the lossless case below threshold and the lossy case below the singularity threshold determined in Section 4.4.2.

¹I check that the numerator is not also zero at that point.

Comparison of abstract mode structures

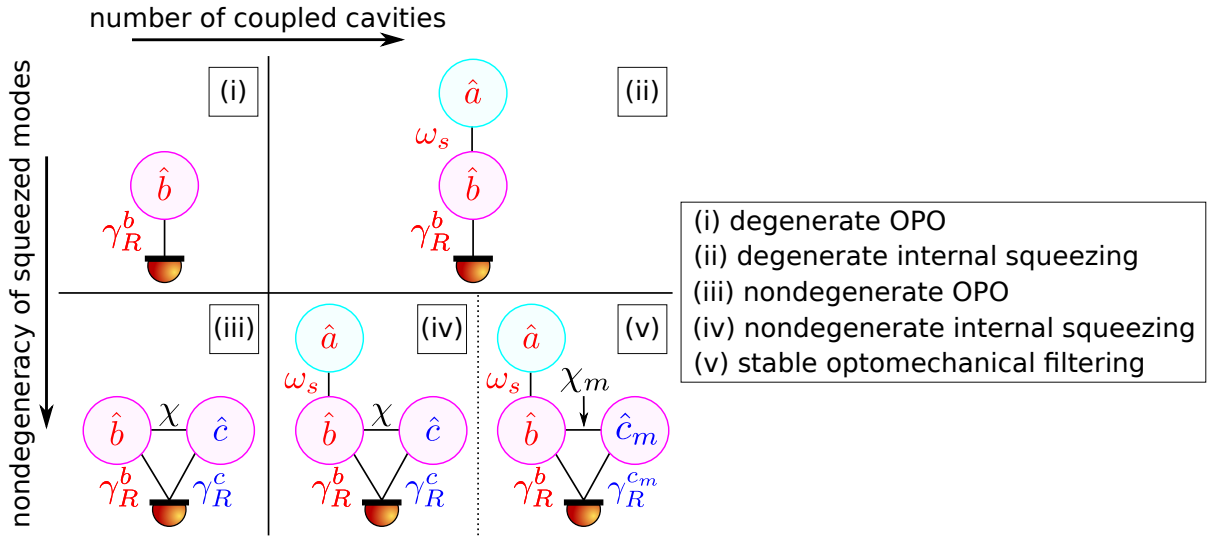


Figure B.1: Abstract mode diagrams of the different configurations considered in this thesis. The modes and coupling rates are explained in Sections 2.2, 3.1.1, 3.2, and 4.1. Whenever the arm mode \hat{a} is shown, it is implicitly connected to the test mass mechanical mode \hat{x} and the gravitational wave signal $h(t)$. Losses are not shown. The photodetector shows the possibility for idler (optical or mechanical) or signal readout.

In Fig. B.1, I compare the abstract mode structure of each of the configurations in this thesis. The parallels between the OPOs and the internal squeezing configurations can be seen. Nondegenerate internal squeezing and stable optomechanical filtering are modally equivalent but are optomechanical and all-optical, respectively, which means that their performance might be different given the different losses they encounter. When idler readout is used, although the internal mode structure is the same as signal readout, the photodetector “sees” the structure differently because it measures a different mode.

Singularity threshold for degenerate internal squeezing

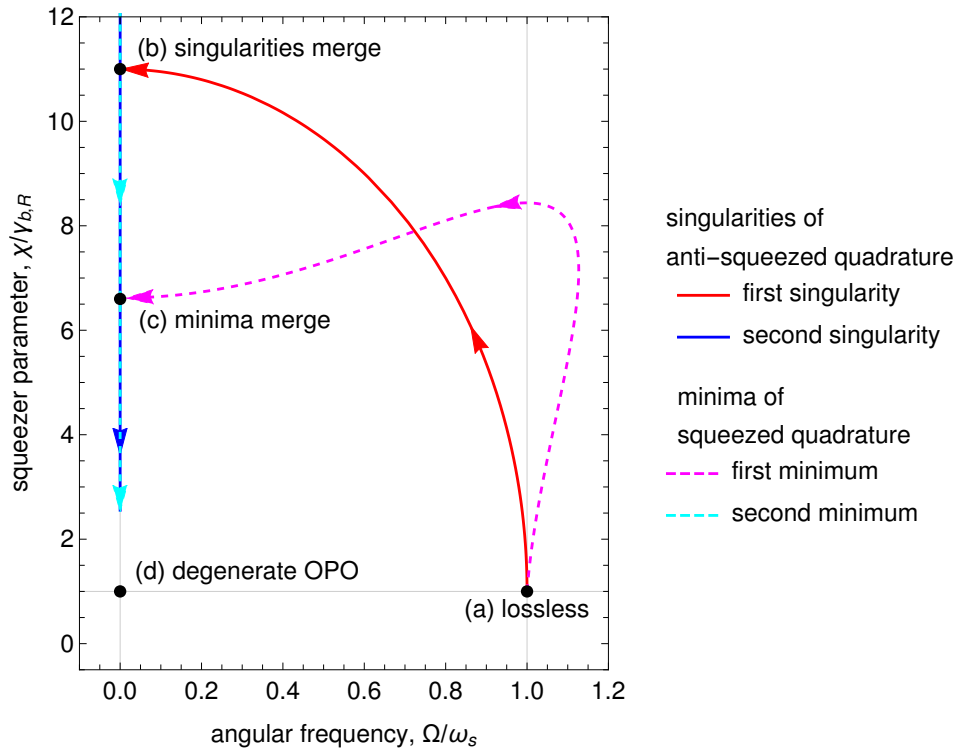


Figure C.1: Degenerate internal squeezing trajectories of the singularities of the anti-squeezed quadrature of the noise and the extrema of the squeezed quadrature in (Ω, χ) space as the arm loss is changed from $T_{l,a} \in (0, 1)$. I assume that the extrema are minima because of the shape of the noise response in Fig. 3.2. The singularities and minima both achieve the same (a) lossless and (d) high arm loss limits, where neither reaches (d) because of limited numerical sampling. However, the singularities and minima diverge at high arm losses (e.g. $T_{l,a} > 0.1$) and merge with their counterparts moving in from infinity at different squeezer parameters shown at (b) and (c), respectively. I use the parameters in Table 4.1 and zero signal loss.

The singularity threshold, see Section 4.4.2, for degenerate internal squeezing shows that maximising the anti-squeezed quadrature is not the same as minimising the squeezed quadrature. As shown in Fig. C.1, in the lossless case, the singularities (Ω, χ) are at $(0, \infty)$ and $(\omega_s, \gamma_{\text{tot}}^b)$ which recovers threshold from Section 3.1.1. As the arm loss γ_a is increased from zero, the singularities move and merge at the $\Omega = 0$ axis when $\gamma_a = \omega_s$, and then the remaining singularity converges to the degenerate OPO threshold $(\Omega_{\text{thr}}, \chi_{\text{thr}}) \xrightarrow{\gamma_a \rightarrow \infty} (0, \gamma_{\text{tot}}^b)$ in the high arm loss limit as expected. However, where the anti-squeezed quadrature is divergent does not necessarily correspond to where the squeezed quadrature has the minimum value. This is unlike the degenerate OPO in Eq. 2.10 where the squeezed quadrature is minimised on threshold. If the minima ¹ of the squeezed quadrature were used to define threshold, then their trajectories in (real) (Ω, χ) space would be as shown in Fig. C.1. Although they achieve the same limits, these trajectories are not the same as the singularity trajectories. This does not violate the Heisenberg Uncertainty Principle because the losses increase the uncertainty product. Moreover, the difference between the minima and singularities is only significant with high arm losses that are far above the realistic loss 100 ppm expected for future gravitational-wave detectors (e.g. the squeezing curves only diverge by more than 0.1 dB around $T_{l,a} = 0.1$). Therefore, this difference is not of concern for future work involving singularity threshold. For completeness, two possible explanations for this behaviour are that it comes from the different DC behaviour of the limiting degenerate OPO's quadratures in Fig. 2.5 or that the approximation to the sloshing frequency in Section 4.2 breaks down in the high arm loss limit ² [23]. This might be understood better if the singularity threshold is verified against a pump-depletion model in future work.

¹Since the zeros of the squeezed quadrature are not robust to losses, as shown for the OPO in Fig. 2.5, I consider the minima instead.

²In which case, this model would not represent the physical system in that limit.

Bibliography

- [1] X. Li, M. Goryachev, Y. Ma, et al. 2020. *arXiv:2012.00836 [quant-ph]*.
- [2] A. Franzen. 2009. <http://www.gwoptics.org/ComponentLibrary/>.
- [3] R.-G. Cai, Z. Cao, Z.-K. Guo, et al. 2017. *Natl. Sci. Rev.*, 4(5):687–706.
- [4] M. Maggiore. *Gravitational Waves: Volume 1: Theory and Experiments*. Oxford University Press, 2007.
- [5] B. P. Abbott, R. Abbott, T. D. Abbott, et al. 2019. *Phys. Rev. X*, 9(3):031040.
- [6] R. Abbott, T. D. Abbott, S. Abraham, et al. 2021. *Phys. Rev. X*, 11(2):021053.
- [7] M. Breschi, S. Bernuzzi, F. Zappa, et al. 2019. *Phys. Rev. D*, 100:104029.
- [8] H. Miao, H. Yang, and D. Martynov. 2018. *Phys. Rev. D*, 98(4):044044.
- [9] M. Shibata, K. Kyutoku, T. Yamamoto, et al. 2009. *Phys. Rev. D*, 79:044030.
- [10] C. D. Ott. 2009. *Class. Quantum Grav.*, 26(6):063001.
- [11] C. Messenger, K. Takami, S. Gossan, et al. 2014. *Phys. Rev. X*, 4:041004.
- [12] J. Aasi, B. P. Abbott, R. Abbott, et al. 2015. *Class. Quantum Grav.*, 32:074001.
- [13] A. Freise and K. Strain. 2010. *Living Rev. Relativ.*, 13(1).
- [14] B. P. Abbott, R. Abbott, T. D. Abbott, et al. 2016. *Phys. Rev. Lett.*, 116(6):061102.
- [15] B. J. Meers. 1988. *Phys. Rev. D*, 38(8):2317–2326.
- [16] D. E. McClelland. 1995. *Aust. J. Phys.*, 48(6):953.
- [17] N. Hodgson and H. Weber. *Optical Resonators*. Springer-Verlag, London, 1997.
- [18] A. Buikema, C. Cahillane, G. L. Mansell, et al. 2020. *Phys. Rev. D*, 102(6):062003.
- [19] H. Miao, R. X. Adhikari, Y. Ma, et al. 2017. *Phys. Rev. Lett.*, 119(5):050801.
- [20] A. F. Brooks, G. Vajente, H. Yamamoto, et al. 2021. *Appl. Opt.*, 60(13):4047.
- [21] M. Evans, S. Gras, P. Fritschel, et al. 2015. *Phys. Rev. Lett.*, 114:161102.
- [22] T. C. Hardwick. PhD thesis, Louisiana State University, 2019.
- [23] M. Korobko, Y. Ma, Y. Chen, et al. 2019. *Light Sci. Appl.*, 8(1):118.

- [24] V. B. Adya, M. J. Yap, D. Töyrä, et al. 2020. *Class. Quantum Grav.*, 37(7):07LT02.
- [25] M. Korobko, S. Steinlechner, J. Südbeck, et al. LVK September meeting, 2021.
- [26] H. Miao, Y. Ma, C. Zhao, et al. 2015. *Phys. Rev. Lett.*, 115(21):211104.
- [27] A. Wicht, K. Danzmann, M. Fleischhauer, et al. 1997. *Opt. Commun.*, 134(1):431–439.
- [28] J. Qin, C. Zhao, Y. Ma, et al. 2015. *Opt. Lett.*, 40(10):2337–2340.
- [29] X. Li, J. Smetana, A. S. Ubhi, et al. 2021. *Phys. Rev. D*, 103:122001.
- [30] M. Ying, X. Chen, Y. Hsu, et al. 2021. *J. Phys.*, 54(3).
- [31] M. Page, J. Qin, J. La Fontaine, et al. 2018. *Phys. Rev. D*, 97(12):124060.
- [32] M.-J. Hu, S. Zha, and Y.-S. Zhang. 2021. *arXiv:2007.03978 [astro-ph.IM]*.
- [33] D. Ganapathy, L. McCuller, J. G. Rollins, et al. 2021. *Phys. Rev. D*, 103(2).
- [34] U. L. Andersen, T. Gehring, C. Marquardt, et al. 2016. *Phys. Scr.*, 91(5):053001.
- [35] M. J. Yap, D. W. Gould, T. G. McRae, et al. 2019. *Opt. Lett.*, 44(21):5386–5389.
- [36] C. M. Caves. 1981. *Phys. Rev. D*, 23:1693–1708.
- [37] T. Corbitt and N. Mavalvala. 2003. *SPIE Proceedings*, 5111.
- [38] S. L. Danilishin and F. Y. Khalili. 2012. *Living Rev. Relativ.*, 15(1):5.
- [39] D. F. Walls and G. Milburn. *Quantum Optics*. Springer-Verlag, 1995.
- [40] B. L. Schumaker. 1986. *Phys. Rep.*, 135(6):317–408.
- [41] D. Klyshko. 1967. *JETP Lett.*, 6:23–25.
- [42] J. Aasi, J. Abadie, B. P. Abbott, et al. 2013. *Nat. Photonics*, 7(8):613–619.
- [43] M. J. Collett and C. W. Gardiner. 1984. *Phys. Rev. A*, 30:1386–1391.
- [44] L. Landau, E. Lifshitz, and L. Pitaevskii. *Statistical Physics, Part 1*. Pergamon Press, Oxford, 1980.
- [45] C. W. Gardiner and M. J. Collett. 1985. *Phys. Rev. A*, 31:3761–3774.
- [46] M. D. Reid. 1989. *Phys. Rev. A*, 40(2):913–923.
- [47] Wolfram Research, Inc. 2010.
- [48] M. Martinelli, C. Garrido Alzar, P. Souto Ribeiro, et al. 2001. *Braz. J. Phys.*, 31:597–615.

- [49] C. Schori, J. L. Sørensen, and E. S. Polzik. 2002. *Phys. Rev. A*, 66(3):033802.
- [50] A. Einstein, B. Podolsky, and N. Rosen. 1935. *Phys. Rev.*, 47:777–780.
- [51] Y. Ma, H. Miao, B. Pang, et al. 2017. *Nat. Phys.*, 13(8):776–780.
- [52] B. P. Abbott, R. Abbott, T. D. Abbott, et al. 2016. *Phys. Rev. Lett.*, 116:131103.
- [53] M. Tse, H. Yu, N. Kijbunchoo, et al. 2019. *Phys. Rev. Lett.*, 123(23):231107.
- [54] R. X. Adhikari, K. Arai, A. F. Brooks, et al. 2020. *Class. Quantum Grav.*, 37(16):165003.
- [55] T. Zhang, J. Bentley, and H. Miao. 2021. *Galaxies*, 9(1):3.
- [56] S. L. Danilishin, F. Y. Khalili, and H. Miao. 2019. *Living Rev. Relativ.*, 22(1).
- [57] S. Wills. 2018. *Opt. Photonics News*, 29(5):44–51.
- [58] M. Korobko. PhD thesis, Universität Hamburg, 2020.
- [59] R. Flaminio, J. Franc, C. Michel, et al. 2010. *Class. Quantum Grav.*, 27(8):084030.
- [60] R. El-Ganainy, K. G. Makris, M. Khajavikhan, et al. 2018. *Nat. Phys.*, 14(1):11–19.
- [61] D. Mason, J. Chen, M. Rossi, et al. 2019. *Nat. Phys.*, 15(8):745–749.
- [62] W. P. Bowen and G. J. Milburn. *Quantum Optomechanics*. CRC Press, 2015.
- [63] X. Li, 2021. Personal communication.
- [64] D. D. Brown and A. Freise. 2014. <http://www.gwoptics.org/finesse>.
- [65] N. S. Nise. *Control Systems Engineering*. Wiley, 8th edition, 2019.
- [66] L. Barsotti. 2016. *LIGO Doc. G1601199-v2*.
- [67] D. V. Martynov, E. D. Hall, B. P. Abbott, et al. 2016. *Phys. Rev. D*, 93:112004.
- [68] H. J. Kimble, Y. Levin, A. B. Matsko, et al. 2001. *Phys. Rev. D*, 65(2).
- [69] S. Singh. 2019. *LIGO Doc. T1900380-v1*.
- [70] D. D. Brown, P. Jones, S. Rowlinson, et al. 2020. *SoftwareX*, 12:100613.
- [71] C. Bender, 2021. Personal communication.
- [72] Z.-P. Liu, J. Zhang, Ş. K. Özdemir, et al. 2016. *Phys. Rev. Lett.*, 117(11):110802.
- [73] H. Hodaie, A. U. Hassan, S. Wittek, et al. 2017. *Nature*, 548(7666):187–191.
- [74] J. Südbeck, S. Steinlechner, M. Korobko, et al. 2020. *Nat. Photonics*, 14(4):240–244.
- [75] D. J. Marsh. 2016. *Phys. Rep.*, 643:1–79.
- [76] M. Malnou, D. A. Palken, B. M. Brubaker, et al. 2019. *Phys. Rev. X*, 9:021023.